The Pennsylvania State University

The Graduate School

Department of Electrical Engineering

THE OPTICAL AND DIELECTRIC APPLICATIONS OF POLY(VINYLIDENE FLUORIDE) BASED ELECTRO-ACTIVE POLYMERS

A Dissertation in

Electrical Engineering

by

Qin Chen

Submitted in Partial Fulfillment

of the Requirements

for the Degree of

Doctor of Philosophy

May 2008

The dissertation of Qin Chen was reviewed and approved* by the following:

Qiming Zhang
Distinguished Professor of Electrical Engineering
Dissertation Co-Adviser, Co-Chair of Committee

Shizhuo Yin
Professor of Electrical Engineering
Dissertation Co-Adviser, Co-Chair of Committee

Zhiwen Liu
Assistant Professor of Electrical Engineering

Christopher D. Rahn
Professor of Mechanical Engineering

W. Kenneth Jenkins
Professor of Electrical Engineering
Head of Department of Electrical Engineering

*Signatures are on file in the Graduate School.

Abstract

A family of polymers modified from poly(vinylidene fluoride) exhibit very large electro-optic and dielectric responses. For instance, dielectric constant of higher than 50 and electro-optic (E-O) effect with more than 2% of refractive index change are exhibited by poly(vinylidene fluoride-trifluoroethylene-chlorofluoroethylene) terpolymer, P(VDF-TrFE-CFE). Another example is poly(vinylidene fluoride-chlorotrifluoroethylene) copolymer, P(VDF-CTFE), which can store and release electrical energy density of higher than 25J/cm^2. This thesis presents a study on the application of these polymers in tunable optical devices and high energy density capacitors.

As an example of tunable optical devices, an electrically tunable long-period fiber grating (LPG) with P(VDF-TrFE-CFE) terpolymer as a second cladding has been demonstrated. A theoretical model has been developed to study the device performance. Computer simulation results indicated that the indium tin oxide (ITO) layer which acts the inner electrode for the terpolymer significantly increases the tuning range of the LPG. Furthermore, the tuning range of the LPG depends on the native refractive index of the terpolymer and maximum tuning

range can be achieved if the native index is increased by about 0.02.

A fabrication process for the tunable LPG has been developed which included dip coating of polymer on fiber. In order to increase the native refractive index of the terpolymer to achieve maximum tuning range, a nanocomposite approach has been employed where small amount of high refractive index zinc sulfide nanoparticles were added into terpolymer matrix. With a properly designed chemical synthesis route the nanocomposite exhibited increased refractive index while maintaining high transparency and relatively large E-O effect. Based on the nanocomposite a tunable LPG with tuning range of 50nm has been demonstrated, which is sufficient to cover an entire optical communication band.

In energy storage capacitors, not only high energy density but also high efficiency and reliability of the polymer films are required. For P(VDF-TrFE-CFE) terpolymers, electrical breakdown is an important concern that affects both the energy density and reliability of dielectric capacitors. It has been observed that both the breakdown electric field and conduction current of the terpolymer depends on the type of metal electrode, which indicates that both processes are controlled by metal-polymer interface. Aluminum and chromium showed considerably higher breakdown field and lower current density compared to gold and silver. In addition to the effect of metal work functions, another factor that contributes to the interface effect is the formation of interfacial layer. Such layer was observed for aluminum which is relatively reactive but not for gold which is inert.

In P(VDF-CTFE) copolymer, it has been found that electrical conduction contribute to a significant portion of the energy loss and hence lowers the efficiency. Detailed studies revealed that the conduction current is controlled by charge in-

jection from electrodes modified by bulk mobility. An effective method to reduce the conduction current is to block the charge injection from electrodes using more insulating materials. Poly(2,6-dimethyl-1,4-phenylene oxide) and silicon nitride have been selected as examples of polymeric and inorganic blocking layers and multilayered films containing both P(VDF-CTFE) and blocking layers have been fabricated. Significant reduction of conduction current has been observed while relatively high energy densities were maintained. It was also observed that the upper limit of energy density in such multilayered films is controlled by high field tunneling of charge carriers in the blocking layer.

Table of Contents

List of Figures

List of Tables

Acknowledgments

I wish to express my sincerest appreciation to the following persons who have contributed so generously to this undertaking:

My thesis advisor, Professor Qiming Zhang, for his continuous guidance, encouragement, and patience, without which the eventual completion of my PhD study would be impossible; my co-advisor, Professor Stuart Yin, for his professional assistance and support to my research; the other members of my thesis committee, Professors Zhiwen Liu and Chris Rahn, for their service on my committee and instructive suggestions to my research.

All my colleagues in the lab, especially Drs. Jon Lee and Minren Lin, Yong Wang, Xin Zhou, and Baojin Chu, for their advice, assistance, and friendship over the past several years.

I also wish to express my appreciation to the National Science Foundation (the MRSEC program) and the Office of Naval Research (the MURI program) for the support of my graduate study.

I wish to dedicate this thesis to my parents, Zhixin Chen (dad) and Jing Lin (mom), for their encouragement and patient support to me over many years.

Chapter 1

INRODUCTION: ELECTROACTIVE POLYMERS AND DEVICES

Polymers are found in innumerable applications in people's life, ranging from trivial everyday products such as plastic bags to the most critical components such as o-rings in space shuttles. However, over many years polymers were only used as "passive" materials. It is not until the past several decades that people started to be interested in the "electroactive" properties of polymers, such as piezoelectric effect, electro-optic effect, high electric conductivity, and light-emitting properties. The electroactive properties are critical in many applications in modern technologies. Comparing to their inorganic counterparts, electroactive polymers have their unique advantages in terms of flexibility, toughness, easy processing, low cost, etc. Therefore, the research in electroactive polymers is growing rapidly in recent years.

According to their electrical conductivity, electroactive polymers can be roughly divided into two categories. Among the first are those with relatively high conductivities such as conducting and semiconducting polymers, while for the second are dielectric (insulating) polymers. The work presented in this thesis only involves

dielectric polymers. More specifically, all the polymers discussed in this thesis are based on modified poly(vinylidene fluoride) (PVDF). The uniqueness of PVDF is that it is a ferroelectric polymer, which means there exists a ferroelectric phase which possesses spontaneous electrical polarization that is switchable by applied electric field. Comparing to normal polymers, PVDF exhibits much higher dielectric constant and piezoelectric and electro-optic effects. Some copolymers of PVDF such as P(VDF-TrFE) (TrFE: trifluoroethylene) also have similar properties as PVDF and these polymers found wide range of applications [1].

In many applications, much larger electroactive responses than those shown by PVDF are needed. For instance, electric field induced dimensional and refractive index change in PVDF is about 0.1%, while in polymer actuators and tunable photonic device changes of several percent are often required. The responses of PVDF can be significantly improved through proper material modifications. For instance, Zhang et al have developed a series of so-called relaxor ferroelectric polymers by properly introducing molecular defects into P(VDF-TrFE) copolymers [2]. In relaxor ferroelectric polymers, reversible molecular conformational change with very small hysteresis can be induced by electric field at room temperature. This generates very large strain, refractive index change, and electrical polarization. An example of relaxor ferroelectric polymer is the poly(vinylidene fluoride-trifluoroethylene-chlorofluoroethylene) terpolymer, P(VDF-TrFE-CFE), in which the electric field induced strain of 7% and refractive index change of >2.6% and room temperature dielectric constant of >50 have been achieved [3, 4, 5]. The copolymer P(VDF-CTFE) (CTFE: chlorotrifluoroethylene) is another example of polymers modified from PVDF. The copolymer exhibits similar dielectric constant to PVDF but shows much smaller hysteresis. This allows it to store and release much high energy density (>25J/cm^3) comparing to PVDF (<3J/cm^3). Such high

energy density is very attractive for energy storage capacitors [5, 6].

The purpose of the work presented in this thesis is to utilize the promising material properties of the P(VDF-TrFE-CFE) terpolymer and P(VDF-CTFE) copolymer in real device applications to achieve performances that are impossible for conventional materials. Two areas of applications will be covered, namely, tunable optical devices and high energy density capacitors. As an example of tunable optical devices, an electrically tunable long-period fiber grating (LPG) will be demonstrated. An LPG induces coupling between core and cladding modes in the fiber and produces a deep notch in the transmission spectrum of core mode at the so-called resonance wavelength. LPGs are promising candidates as wavelength filters and sensors in optical communication and sensing systems. In many applications it is often desired that the resonance wavelength of an LPG can be tuned over a wide range (preferably an entire communication band of about 40nm). Tuning of the resonance wavelength can be realized by various mechanisms such as thermo-optic effect, acousto-optic effect, and electro-optic(E-O) effect. E-O effect is perhaps the most ideal mechanism because of its fast speed and nearly zero power consumption. However, the realization of E-O tuning is hindered by the limited refractive index change provided by common E-O materials. For instance, lithium niobate, which is one of the most widely used E-O material, exhibit refractive index change of less than 0.1% which is too small to achieve any significant tuning [7]. The P(VDF-TrFE-CFE) terpolymer has very large E-O effect and its refractive index (n=1.4) is lower than that of fiber cladding (typically 1.44 to 1.45), which allows it to be used as the second cladding layer of the fiber in typical design of E-O tunable LPGs [8]. Therefore, the terpolymer can be potentially an ideal E-O material for tunable LPGs.

A challenging issue in the device design of tunable LPG is how to realize the

40nm tuning using given refractive index change in the terpolymer. In general, in order to achieve larger tuning range with given refractive index change in the terpolymer, it is desired that more light energy is contained in the terpolymer. Both numerical simulation and experiment results showed that the thin indium tin oxide (ITO) layer which acts as the inner electrode of the terpolymer plays an important role in the distribution of light energy. With suitable thickness and refractive index of ITO, when the refractive index of the terpolymer is in certain "sensitive range", large portions of energy are contained in both the second cladding and the core. Such distribution of light energy results in large tuning range as well as sufficient depth of the notch in transmission spectrum. However, the native refractive index of the terpolymer is n=1.4 while in order to reach the sensitive range at least n=1.42 is required. Therefore, the refractive index of the terpolymer needs to be increased by about 0.02 while retaining large E-O effect and high transparency. This has been achieved through a nanocomposite approach where small amount of high refractive index zinc sulfide (ZnS) nanopartiles has been introduced into terpolymer matrix. When the refractive index of the nanocomposite wass adjusted to around 1.42, large tuning range of 50nm has been achieved in the tunable LPG.

The second area of application discussed in this thesis is energy storage dielectric capacitors. Dielectric capacitors are widely used as energy storage components in many power electronic circuits. The energy density U_e of a dielectric material can be related to its dielectric constant K by (assume that K is independent of electric field):

$$U_e = \frac{1}{2} K \epsilon_0 E^2 \tag{1.1}$$

where ϵ_0 is the vacuum permittivity and E is the electric field. A more general

formula that is valid for nonlinear dielectric materials is given by

$$U_e = \int EdD \tag{1.2}$$

All the polymers used in current thin film polymer capacitors show low dielectric constant (e.g. K=2.2 for polypropylene and K=2.8 for polycarbonate). However, polymers are still the preferred choice as capacitor materials due to their extremely high breakdown field (>500 MV/m) and the self-healing after breakdown, which renders the capacitors with high reliability and leads to high energy density (typically 1-3J/cm^3). It is highly desirable to further increase the energy density of polymers in order to reduce the volume of the capacitors. The P(VDF-TrFE-CFE) terpolymer has much higher dielectric constant than conventional polymers and it can achieve a high energy density of about 9J/cm^3. A drawback of the terpolymer is that its dielectric constant decreases at higher fields due to the early saturation of electrical polarization. According to equation (1.2), this means at high fields the polarization as well as the energy density only increases slowly with electric field. On the other hand, the P(VDF-CTFE) copolymer has a dielectric constant of about 13 which is much lower comparing to the low field dielectric constant of 50 in the terpolymer. However, the copolymer does not exhibit polarization saturation and has very high breakdown electric field (>600MV/m), which result in higher energy density of >25J/cm^3.

Real applications not only demands high energy density in capacitors but also high breakdown electric field and efficiency. Breakdown electric field is an especially important concern for the P(VDF-TrFE-CFE) terpolymer. One of the methods to control the breakdown field of the terpolymer is to modify the interface between metal electrode and polymer. Experimental results revealed that in

terms of both mean value and the width of distribution of the breakdown fields, reactive metals such as aluminum and chromium exhibit better performances than more inert metals such as gold and silver. Furthermore, the metal electrodes showing better breakdown characteristics also have lower leakage current, which suggests that the breakdown process is strongly affected charge injection from the electrode. The dependence of the breakdown fields and injection currents of dielectric materials on metal electrodes is often due to work function difference between metals [9]. For the terpolymer, it has been found that another reason for electrode dependence is the formation of interfacial layer between metal electrode and the polymer. Such layer has been detected for reactive metals such as aluminum by dielectric and photoemission measurements, but not for inert metals such as gold.

For the P(VDF-CTFE) copolymer the most important concern is the conduction loss which significantly reduces the energy efficiency. P(VDF-CTFE) is a dielectric polymer that contain very small amount of charge carriers and the conduction currents are dominated by external carriers that are injected from the electrodes. Therefore, in order to reduce the conduction loss an efficient method is to block the charge injection using highly insulating layers. A blocking material must not only have low leakage current but also have a fabrication process that is compatible with the copolymer. Poly(2,6-dimethyl-1,4-phenylene oxide) (PPO) has excellent insulating properties and cannot be dissolved by the solvent used for P(VDF-CTFE). On the other hand, the solvent for PPO also does not dissolve P(VDF-CTFE). Therefore, multilayered PPO/P(VDF-CTFE) films can be readily fabricated through layer by layer spin coating. The efficiency in PPO/P(VDF-CTFE) multilayers can reach >90% while typical value for pure P(VDF-CTFE) is lower than 70% at similar energy density level. A drawback of all-polymer multilayers is that the polymers with low conduction losses also have low dielectric

constant (e.g. PPO K=2.8) which significantly reduces the overall dielectric constant of the multilayered films (e.g. in the high efficiency PPO/P(VDF-CTFE) mentioned above, K=5.5) and limits the maximum operation electric field. In contrast, inorganic materials with both low leakage current and dielectric constant close to or even higher than P(VDF-CTFE) are widely available [10]. Therefore, we investigated the feasiblity of using inorganic material as blocking layers. The most critical concern for inorganic blocking layers is that the typical deposition process for these materials involves high temperature or plasma energy that often damages the polymer film. The melting point of P(VDF-CTFE) is 165° and hence the deposition temperature of inorganic layer should be at least lower than this value. Based on this consideration, silicon nitride (Si_3N_4) has been selected as a prototypical inorganic blocking layer since it has very good insulating properties and can be deposited at below 150° using plasma enhanced chemical vapor deposition (PECVD). The efficiency of Si_3N_4/P(VDF-CTFE) multilayer is higher than 80% and a relatively high dielectric constant of >10 can be achieved.

The topics covered in this thesis are arranged as follow. Chapter 2 provides a brief review of PVDF based relaxor ferroelectric polymers. Chapter 3 and Chapter 4 discuss the development of tunable LPG, where Chapter 3 presents a theoretical analysis of the LPG response using a simulation model and the details about the fabrication and characterization of the tunable LPG as well as the nanocomposite are provided in Chapter 4. The next two chapters cover the applications in high energy density capacitors, where Chapter 5 presents the study on the metal-polymer interface and breakdown of the P(VDF-TrFE-CFE) terpolymer, while Chapter 6 discusses the conduction in P(VDF-CTEF) copolymer and reduction of conduction using blocking layers. Finally, a conclusion and some suggested future work are presented in Chapter 7.

Chapter 2

POLY(VINYLIDENE FLUORIDE) BASED ELECTRO-ACTIVE POLYMERS

All the work presented in this thesis is based on electro-active polymers that are derived from poly(vinylidene fluoride) (PVDF). Before delving into detailed discussion on the device applications, a brief introduction to PVDF based electroactive polymers is presented in this chapter. Due to limited space we will only discuss PVDF homopolymer and P(VDF-TrFE-CFE) terpolymer in this chapter. More detailed information about PVDF based polymers can be found in several excellent reviews [1, 12, 13, 14].

2.1 Poly(vinylidene fluoride)

PVDF was first synthesized over sixty years ago and has long been used as long-life coatings and as an electrical insulator and chemical inert material in chemical

processing equipment [11]. Large piezoelectric effect has been discovered in PVDF in late 1960's and since then extensive study has been carried out to prove the ferroelectric nature of PVDF and to elucidate the relation between its properties and structures [1, 11, 15]. At the same time, many applications of PVDF has been demonstrated, such as in transducers, electromechanical actuators, pyroelectric devices, etc [16]. In the late 1990's, relaxor ferroelectric behavior has been realized in defect modified PVDF copolymers and terpolymers [2]. This resulted in significant increase of dielectric constant and electromechanical and electro-optic effects than in normal PVDF.

The chemical structure of PVDF is $[\text{-}CH_2\text{-}CF_2\text{-}]_n$. Vinylidene fluoride can be copolomerized with trifluoroethylene (TrFE, chemical structure $CHF{=}CF_2$) to form the copolymer P(VDF-TrFE). The copolymer shows similar and in some cases superior properties comparing to PVDF homopolymer [14].

Although PVDF and P(VDF-TrFE) have simple chemical formulas, their physical structures are much more complicated and it is these diverse structures that resulted in their unique properties. PVDF shows several levels of physical structures, namely, individual polymer chains, crystalline forms (packing of individual chains), and the morphology of polymer films. An individual PVDF chain can take several different conformations, such as the so-called all-*trans*, TG^+TG^-, and $TTTG^+TTTG^-$ conformations (Figure 2.1). A major difference between these conformations is that the C-F and C-H bonds take different directions. Since the net dipole moment of the chain is the vectorial sum of dipole moment carried by individual segments, the different conformations exhibit different net dipole moments. The all-*trans* conformation is the most polar one with dipole moment of 7.0×10^{-30}C-m per repeat unit in the direction perpendicular to chain axis. The TG^+TG^- conformation carries dipole moment of 4.0×10^{-30}C-m perpendicular

and 3.4×10^{-30}C-m parallel to the chain axis. Similar values are held by the $TTTG^{+}\,TTTG^{-}$ conformation. In addition net dipole moment, different conformations also have different length of repeating units of the polymer chain.

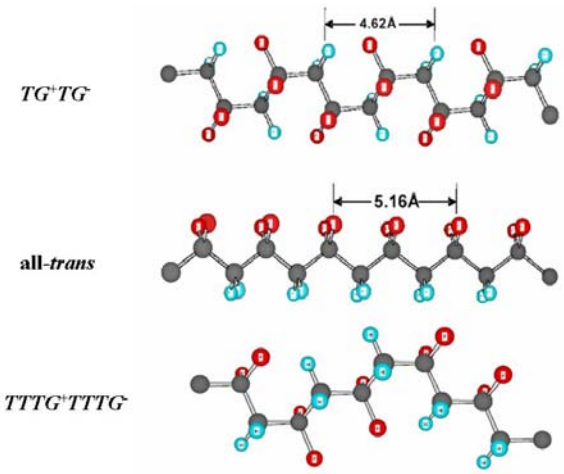

Figure 2.1. The different molecular conformations of PVDF

PVDF is a semi-crystalline polymer, which means there exists both crystalline and amorphous regions. In its crystalline region the polymer chains are packed into different crystalline forms, depending not only on the conformation of each individual chains but also the way of packing. The four most common crystalline forms of PVDF are the α, β, γ, and δ phases (Figure 2.2, 2.3). In α phase, the individual chains have $TG^{+}\,TG^{-}$ conformation and the chains are packed in a non-polar manner so that their dipole moments cancel each other, resulting in zero net polarization. In β phase, the chains have all-*trans* conformation and are packed in a polar manner that the dipole moments of all chains are in the same direction, and hence the β phase is a highly polar phase. The γ phase consists of chains with $TTTG^{+}\,TTTG^{-}$ conformation packed in a polar manner. Finally, the δ phase can be imagined as the polar counterpart of the α phase. The crystalline regions in PVDF consist of lamellae of typically 10 to 20nm thick, where the polymer

chains are perpendicular to the surface of the lamellae and are folded such that they penetrate the lamellae for many times. The lamellae further form spherulites (Figure 2.4). The crystalline regions are surrounded by an amourphous sea of scrambled, spaghettilike chains.

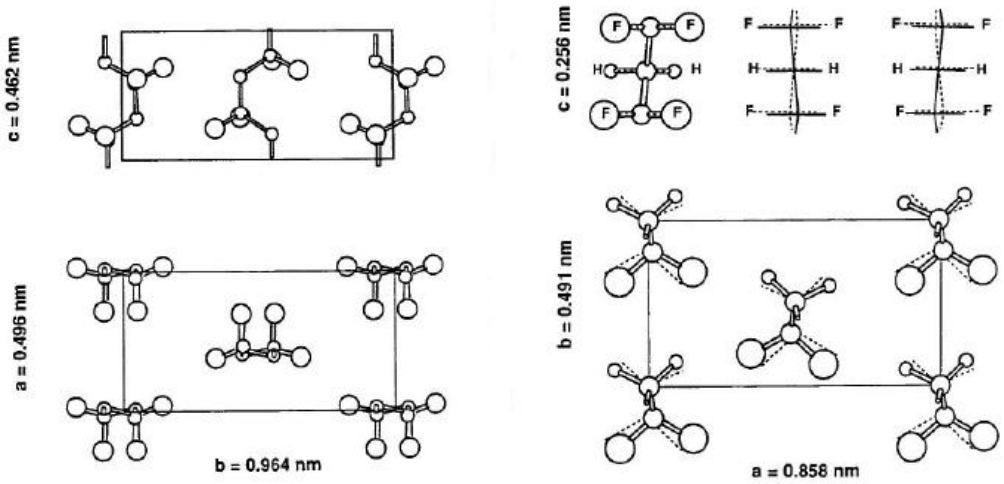

(a) α phase (b) β phase

Figure 2.2. The α and β phases of PVDF. (Adapted from [11])

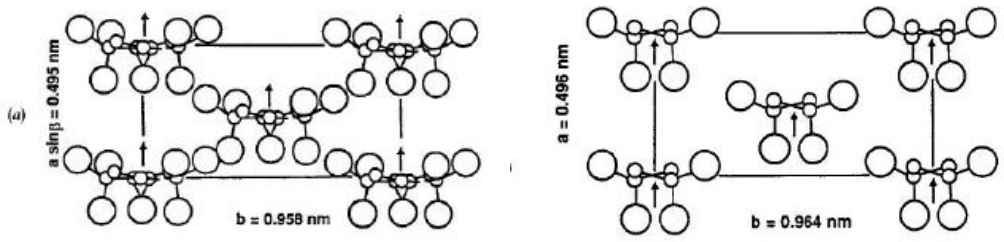

(a) γ phase (b) δ phase

Figure 2.3. The γ and δ phases of PVDF. (Adapted from [11])

The crystalline phase of PVDF depend on the preparation method and the different phases can be transformed into each other under certain conditions. For instance, PVDF films prepared from melt solidification are in α phase. When α phase PVDF is uniaxially stretched to several times it can be converted to β phase. On the other hand, when PVDF film in α phase is subjected to increasingly large

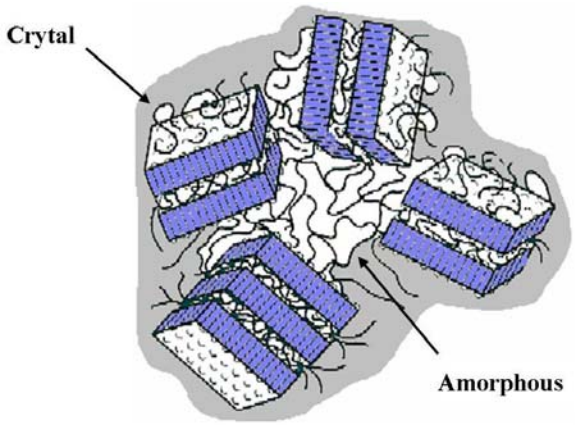

Figure 2.4. The morphology of PVDF, showing the crystalline lamellae and amorphous regions. (Adapted from [11])

electric fields, it will first be converted to δ phase and then to β phase at very high fields. The β phase of PVDF is a ferroelectric phase and exhibits the largest piezoelectric effect among all the phases. Therefore, it is the most attractive phase for early applications of PVDF that used its piezoelectric and pyroelectric effects.

2.2 Relaxor ferroelectric polymers

Although the ferroelectric β phase of PVDF exhibit relatively large piezoelectric, pyroelectric and electro-optic effects and have been used in various applications, the mechanical strain and refractive index change exhibited by PVDF is typically less than 0.1%, which cannot meet the requirement of many applications such as some electromechanical actuators and tunable photonic devices. An important property of PVDF based ferroelectric polymers is the transition from ferroelectric phase to paraelectric phase at increased temperature. Such phase transition generates much larger difference (as large as 10%) in dimension, refractive index and electrical polarization than those generated by the ferroelectric phase itself. In PVDF homopolymer the energy barrier for such transition is so large that no

phase transition could be observed up to the melting temperature. In P(VDF-TrFE) copolymer, on the other hand, the increased amount of TrFE units efficiently reduces the transition temperature to below the melting point[1]. It has been found that when the content of VDF is between 50-80 mol%, phase transition can be readily observed in P(VDF-TrFE) with transition temperatures in the range between 70° and 140° [14].

However, a drawback of the ferroelectric phase transitions in P(VDF-TrFE) copolymers is that they are associated with large hysteresis. Moreover, they occur at higher temperature than the room temperature (>70°C). It is well known in ferroelectric ceramics that the hysteresis associated with phase transition is due to the large energy barrier between the two phases. The energy barrier can be reduced by breaking the large ferroelectric domains into microdomains through introduction of defects. In this way, the normal ferroelectric P(VDF-TrFE) is converted into a relaxor ferroelectric material. The large hysteresis associated with phase transition is significantly reduced or even eliminated in relaxor ferroelectric polymers and a reversible phase transition can be induced by electric field at room temperature [2].

For P(VDF-TrFE) copolymer the molecular defects can be introduced by either high energy electron irradiation or chemical modification [2, 3]. From the standpoint of device applications, the latter approach is preferred because the chemically modified polymer are available as ready-to-use powders and hence can be easily processed. One of such modified copolymer is the poly(vinylidene fluoride-trifluoroethylene-chlorofluoroethylene) terpolymer, P(VDF-TrFE-CFE) (Figure 2.5). A typical composition of the terpolymer is VDF:TrFE:CFE=65:35:10 mol%. Since the dimension of chlorine atoms is much larger than all the other atoms in P(VDF-TrFE), the termonomer CFE effectively acts as structural defect in the

polymer.

Figure 2.5. The chemical structure of P(VDF-TrFE-CFE) terpolymer.

The polarization of the P(VDF-TrFE-CFE) terpolymer is characterized by the D-E loop curves, where D represents the electrical displacement and E represents the electric field. As shown in Figure 2.6, the hysteresis for the terpolymer is much smaller than that of the unmodified copolymer. Therefore, high polarization level can be induced by electric field reversibly and the room temperature dielectric constant is larger than 50. The electro-optic (E-O) response and the electromechanical strain of the terpolymer are shown in Figures 2.7 and 2.8. In order to measure the E-O effect, the transmission along the normal direction of the film is recorded using an FTIR spectrometer and from the electric field induced spectrum shift the overall optical path length change can be determined. Since the strain of the terpolymer can be measured independently using photonic sensors, pure refractive index change can be extracted from the path length change. Experimental result shows that pure refractive index change of -2.6% can be achieved under electric field of 80MV/m and the strain along film thickness direction is 3% under the same electric field.

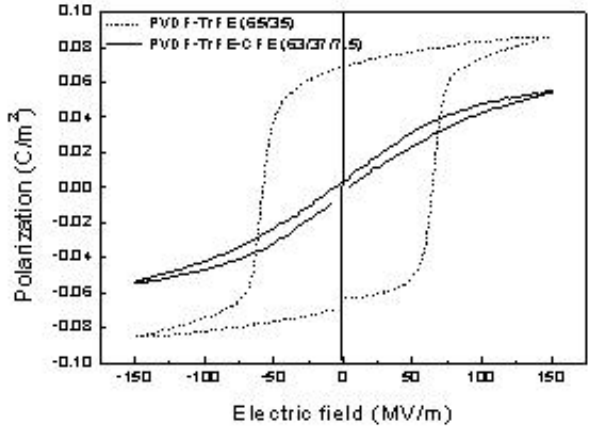

Figure 2.6. The D-E loops of a relaxor ferroelectric terpolymer and a normal ferroelectric copolymer. [18]

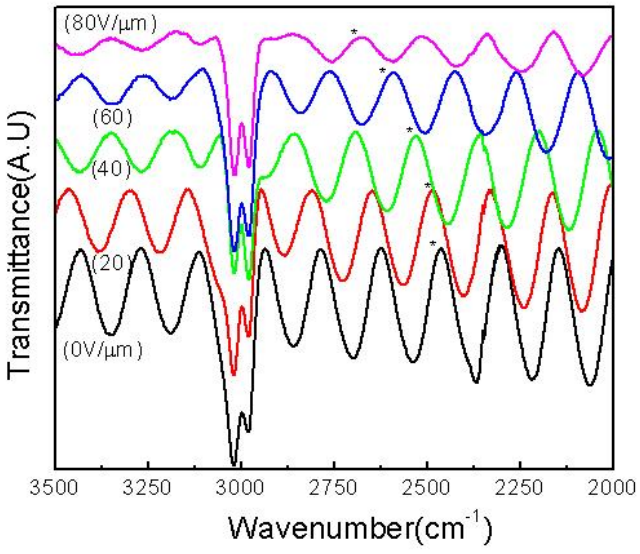

Figure 2.7. The electro-optic response of a relaxor ferroelectric terpolymer. [4]

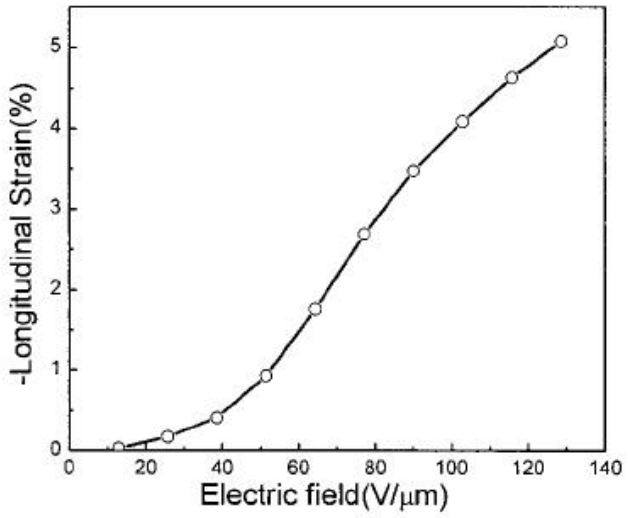

Figure 2.8. The D-E loops of a relaxor ferroelectric terpolymer and a normal ferroelectric copolymer. [4]

The strain and electro-optic effect exhibited by the terpolymer are more than an order of magnitude higher than those in most conventional electro-active materials. For instance, in common ferroelectric ceramics and single crystals the dimensional and refractive index changes are typically smaller than 0.1%. On the other hand, the dielectric constant and polarization level in the terpolymer are also significantly higher than common dielectric polymers such as polypropylene (2.2) and polycarbonate (2.8). Therefore, the terpolymer provides promising opportunities for device applications. In the following several chapters, applications of the terpolymer in tunable optical devices and energy storage capacitors are going to be demonstrated. For energy storage capacitors, another PVDF based polymer, the P(VDF-CTFE) copolymer, will also be discussed. More information regarding the detailed material properties are going to be presented in this thesis along with device applications.

Chapter 3

THEORETICAL ANALYSIS OF TUNABLE LONG-PERIOD FIBER GRATINGS

This chapter and Chapter 4 focus on the application of P(VDF-TrFE-CFE) terpolymer in tunable optical device. The design, fabrication and test results of a tunable long-period fiber grating (LPG) with the terpolymer as a second cladding layer will be presented. The tunable LPG developed here has a large tuning range that can cover an entire fiber optic communication band. This device not only demonstrated the advantage of the large E-O effect of the terpolymer in tunable optical devices, but also indicated how to properly design the device structure to maximize the tuning range with given magnitude of E-O effect, as well as a method to modify the native refractive index of the terpolymer which is required to further increase the tuning range. This chapter covers the working principle, design, and theoretical analysis of the tunable LPG which indicate the method to achieve the largest tuning range. The experimental methods and results will be presented in

Chapter 4.

3.1 Introduction to tunable long-period gratings

In fiber-optic communication networks, sensing systems, and scientific instrumentations, wavelength selectivity is often of the central importance. In optical fibers the wavelength selectivity is usually realized by fiber gratings. In order to understand the operation principle of fiber gratings, I will briefly review the basic structure and operation principle of optical fiber. The cross-sectional view of an optical fiber is presented in Figure 3.1, showing the core and cladding layers of the fiber and the surrounding medium which may be the plastic jacket in commercial fibers or any other material in specific fiber devices. Generally we have $n_{co} > n_{cl} > n_s$, where n_{co}, n_{cl}, and n_s are the refractive indexes of core, cladding, and surrounding medium, respectively. Therefore, total internal reflection can happen at both the core-cladding boundary and cladding-surrounding medium boundary, and hence light can be guided in the core only (core mode) or also in the cladding (cladding mode). Core mode has very small optical loss and carries signal in optical communication systems. Cladding mode, on the other hand, experiences much higher attenuation due to surface scattering, bending loss, etc [19].

The most important concepts of light in a fiber are the modes and the effective refractive index and field distribution of modes. An optical fiber is a cylindrical structure with a circular cross-section and infinitely extends along its axis. Light in fiber can be generally expressed as:

$$E_z(r, \theta, z) = E(r)e^{j\nu\theta}e^{jn_{eff}k_0 z} \tag{3.1}$$

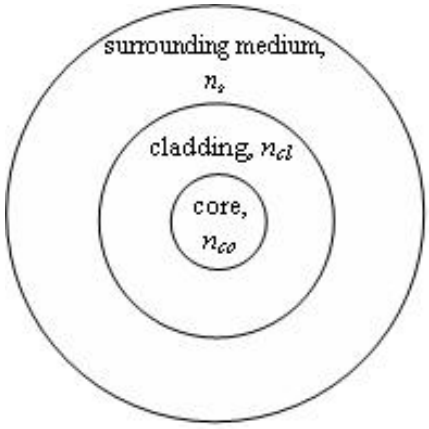

Figure 3.1. The cross-sectional view of an optical fiber.

where r, θ and z represents the radial, azimuthal and axial coordinates, and k_0 is the wave number in vacuum. The parameters ν and n_{eff} are called the azimuthal order and the effective refractive index. Due to cylindrical symmetry we have $\nu = 0, 1, 2, \cdots$. Here only the z-component of electric field is considered, but all the electric and magnetic field components can be treated similarly. For a step-index fiber, in each layer the radial field distribution $E(r)$ is governed by the equation [20]

$$\frac{d^2E(r)}{dr^2} + \frac{1}{r}\frac{dE(r)}{dr} + [k_0^2(n_m^2 - n_{eff}^2) - \frac{\nu^2}{r^2}]E(r) = 0 \tag{3.2}$$

where n_m denotes the refractive index of the mth layer of fiber. In most cases we are only interested in bounded modes in core or cladding. In this case, for each azimuthal order ν there exists a series of eigenmodes that satisfy (3.2) and each eigenmode has a specific n_{eff} and field distribution $E(r)$. The term "bounded" is most easily understood in a ray optics picture. For core modes, rays are bounded by the reflection at the core-cladding boundary and hence $n_{co} > n_{eff} > n_{cl}$. Outside the core, light is in the form of evanescent wave in the radial direction and the intensity decays to zero as the diameter increases towards infinity. Similarly,

for cladding modes $n_{cl} > n_{eff} > n_s$ and light is bounded in the cladding by is evanescent outside the cladding.

In a perfect fiber without structural perturbations, the eigenmodes propagate independently without interacting with each other. However, when a periodic perturbation (usually refractive index change) exist in the fiber, coupling between two modes will happen provided that the so-called phase-matching condition is satisfied:

$$\frac{2\pi}{\lambda}(n_{eff}^{(1)} - n_{eff}^{(2)}) = \frac{2\pi}{\Lambda} \tag{3.3}$$

where λ is the wavelength of light in vacuum, Λ is the period of the perturbation, and $n_{eff}^{(1)}$ and $n_{eff}^{(2)}$ are the effective refractive indexes of the two modes. The phase matching condition is satisfied at the resonance wavelength λ_0 which is given by

$$\lambda_0 = (n_{eff}^{(1)} - n_{eff}^{(2)})\Lambda \tag{3.4}$$

We call the periodically perturbed fiber structure a fiber grating. According to equation (3.4), a fiber grating induces mode coupling only at the resonance wavelength where light energy in one mode will be transfered to another. This results in change of transmittance of the mode at the resonance wavelength and hence realizes wavelength selectivity in fiber.

According to the grating period Λ and light wavelength λ, fiber gratings can be classified into fiber Bragg (short period) grating (FBG) in which $\Lambda \sim \lambda$ and long-period gratings (LPG) in which $\Lambda >> \lambda$ (Figure 3.2). In FBGs, the phase matching condition (equation (3.4)) implies that $n_{eff}^{(1)} - n_{eff}^{(2)} = \frac{\lambda_0}{\Lambda} \sim 1$. In a fiber the difference between the effective indexes of two modes propagating in the same direction is very small, and hence in FBG the phase matching condition can only

be satisfied by modes propagation in opposite directions. In practice, an FBG is usually used to couple a core mode to a counter-propagating core mode. In LPGs, on the other hand, $n_{eff}^{(1)} - n_{eff}^{(2)} = \frac{\lambda_0}{\Lambda} \approx 0$, and hence coupling occurs between two co-propagating modes, usually a core mode and a cladding mode. Cladding modes experience large attenuations and the energy will be lost quickly. In both FBG and LPG the coupling results in notch(es) in the transmission spectrum of the core mode. (Figure 3.2)

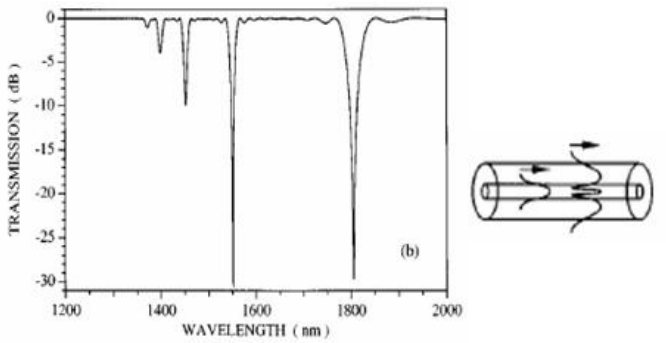

(a) LPG

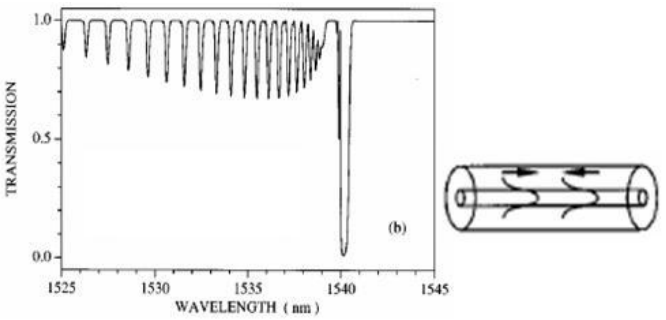

(b) FBG

Figure 3.2. Typical transmission spectrums of long-period gratings (LPG) and fiber Bragg (short period) gratings (FBG). The insets illustrate the core-cladding and core-core couplings. (Adapted from [26])

$$\lambda_0 = (n_{eff}^{(co)} - n_{eff}^{(cl)})\Lambda \tag{3.5}$$

It is often desirable that the resonance wavelength of a fiber grating is dynam-

ically reconfigurable in certain range. In particular a tuning range that can cover an entire communication band of about 40nm is highly demanded. According to equation (3.4), the resonance wavelength can be tuned by varying the grating period and/or the effective refractive indexes of the modes. Very limited dimensional change can be induced in silica fiber and hence it is more feasible to tune the effective refractive index of the modes rather than grating period. In this sense, LPGs are preferred over FBGs because of the large period multiplied to the effective indexes (equation (3.4)) which "amplifies" the effective index change to give a much larger shift of resonance wavelength. Tunable LPGs with tuning range of more than 40nm has been demonstrated only in polymer filled microstructured fibers where the effective refractive index change is generated by thermo-optic effect [21, 22]. However, the drawbacks of thermal tuning are the power consumption for heat generation and the slow speed. On the other hand, E-O effect has much faster speed and consumes essentially no electric power and is perhaps the most ideal tuning mechanism. However, within the author's knowledge, due to the lack of suitable E-O material very few E-O tunable LPGs have been reported and the tuning range is at most several nanometers [23]. The P(VDF-TrFE-CFE) terpolymer exhibit much larger E-O effect than conventional E-O materials and refractive index change of more than 0.01 can be generated by electric field. Therefore, the terpolymer can potentially significantly increase the tuning range of E-O tunable LPGs.

A device structure proposed by Yin et al has been chosen for the E-O tunable LPG (Figure 3.3), in which the terpolymer forms a second cladding in addition to the original cladding of the fiber. An indium-tin oxide (ITO) layer and a metal layer act as the inner and outer electrodes of the terpolymer. When electric field is applied, refractive index change is generated in the terpolymer through E-O effect

which in turn changes the effective refractive index of the cladding mode and hence tunes the resonance wavelength of the LPG. The advantage of this structure is that no additional loss is introduced to core mode at wavelengths away from the resonance wavelength. Furthermore, the fabrication of this device only involves deposition of organic and inorganic layers on the fiber, which is relatively easy to implement.

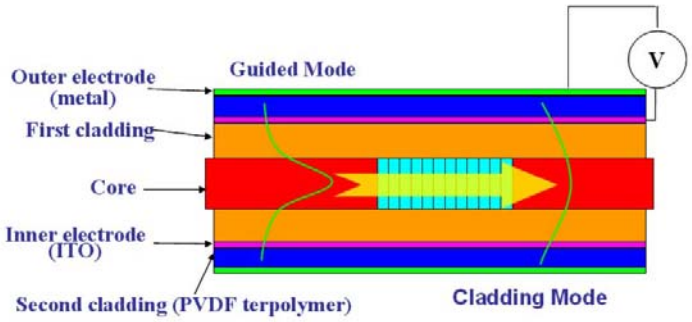

Figure 3.3. The structure of an electrically tunable LPG.

Even though the terpolymer exhibits a large E-O effect, the device structure of the LPG must be properly designed to realize the desired tuning range of 40nm with the refractive index change generated in the terpolymer. Furthermore, while the resonance wavelength is tuned the variation in the transmittance of grating must be minimized. In the following sections, a precise model will be developed to theoretically analyze the properties of the tunable LPG.

3.2 A precise model for computer simulation of LPG

The properties of a fiber grating can be analyzed using coupled-mode theory [24]. In this section, we will first present the coupled-mode formalism for LPGs and then provide the method to calculate the effective index and field distribution of modes that are the most important parameters in coupled-mode theory.

Coupled-Mode Formalism for Long-Period Gratings

We follow closely the treatment on coupled-mode theory as described in [25]. When certain perturbation exists in a waveguide, it can be treated as an additional polarization term:

$$\nabla \times \vec{E} = -j\omega\mu\vec{H} \tag{3.6}$$

$$\nabla \times \vec{H} = j\omega\epsilon\vec{E} + j\omega\vec{P} \tag{3.7}$$

If there are two waves propagating in the fiber (denoted by 1 and 2), from equations (3.6) and (3.7) we havex

$$\nabla \cdot (\vec{E}_1 \times \vec{H}_2^* + \vec{E}_2^* \times \vec{H}_1) = -j\omega\vec{P}_1 \cdot \vec{E}_2^* + j\omega\vec{P}_2^* \cdot \vec{E}_1 \tag{3.8}$$

Now we set wave 2 as a mode in the waveguide and hence $\vec{P}_2 = 0$, and integrate equation (3.8) over the entire cross section and use the divergence theorem, we

have

$$\iint_{-\infty}^{+\infty} dxdy\frac{\partial}{\partial z}(\vec{E}_1 \times \vec{H}_2^* + \vec{E}_2^* \times \vec{H}_1)_z = -j\omega \iint_{-\infty}^{+\infty} dxdy\vec{P}_1 \cdot \vec{E}_2^* \tag{3.9}$$

Decompose the first wave into summation of eigenmodes, then

$$\vec{E}_{1t} = \sum(a_\nu + b_\nu)\vec{E}_{t\nu} \tag{3.10}$$

$$\vec{H}_{1t} = \sum(a_\nu - b_\nu)\vec{H}_{t\nu} \tag{3.11}$$

where a_ν and b_ν are coefficients of forward and backward propagating modes, respectively. Let the second wave be a forward propagating mode, we have

$$\vec{E}_2 = \vec{E}_\mu exp(-j\beta_\mu z) \tag{3.12}$$

$$\vec{H}_2 = \vec{H}_\mu exp(-j\beta_\mu z) \tag{3.13}$$

The eigenmodes satisfy the orthonormality relation:

$$2\iint_{-\infty}^{+\infty} dxdy\vec{E}_{\nu\mu} \times \vec{H}_{\bar{\nu}\bar{\mu}}^* = \delta_{\nu\bar{\nu}}\delta_{\mu\bar{\mu}} \tag{3.14}$$

and hence

$$\frac{da_\mu}{dz} + j\beta_\mu a_\mu = -j\omega \iint_{-\infty}^{+\infty} dxdy\vec{P} \cdot \vec{E}_\mu^* \tag{3.15}$$

By changing wave 2 in equation (3.8) into a backward propagating wave, we will get

$$\frac{db_\mu}{dz} - j\beta_\mu b_\mu = j\omega \iint_{-\infty}^{+\infty} dxdy\vec{P} \cdot \vec{E}_{-\mu}^* \tag{3.16}$$

Define A_μ and B_μ as

$$a_\mu = A_\mu exp(-j\beta_\mu z) \tag{3.17}$$

$$b_\mu = B_\mu exp(j\beta_\mu z) \tag{3.18}$$

then

$$\frac{dA_\mu}{dz} = -j\omega \iint_{-\infty}^{+\infty} dxdy\vec{P} \cdot \vec{E}_\mu^* exp(j\beta_\mu z) \tag{3.19}$$

$$\frac{dB_\mu}{dz} = j\omega \iint_{-\infty}^{+\infty} dxdy\vec{P} \cdot \vec{E}_{-\mu}^* exp(-j\beta_\mu z) \tag{3.20}$$

For a waveguide with perturbation $\Delta\epsilon$, we have

$$\vec{P} = \Delta\epsilon\vec{E} \tag{3.21}$$

The longitudinal and transverse components are treated separately:

$$\vec{P}_t = \Delta\epsilon\vec{E}_t = \Delta\epsilon \sum (a_\nu + b_\nu)\vec{E}_{t\nu} \tag{3.22}$$

According to Maxwell's equation, after introduction of perturbation we have

$$j\omega(\epsilon + \Delta\epsilon)\vec{E}_z = \nabla_t \times \vec{H}_t \tag{3.23}$$

and hence

$$\begin{aligned} \vec{P}_z &= \Delta\epsilon\vec{E}_z \\ &= \frac{\Delta\epsilon}{j\omega(\epsilon + \Delta\epsilon)} \nabla_t \times \vec{H}_t \\ &= \frac{\Delta\epsilon \cdot \epsilon}{\epsilon + \Delta\epsilon} \sum (a_\nu - b_\nu)\vec{E}_{z\nu} \end{aligned} \tag{3.24}$$

Substitute the decomposed polarization into equations (3.19) and (3.20), we have

$$\begin{aligned}\frac{dA_\mu}{dz} =& -j\omega \iint_{-\infty}^{\infty} dxdy \sum [(a_\nu + b_\nu)\Delta\epsilon \vec{E}_{t\nu} \cdot \vec{E}^*_{t\mu} \\ &+ (a_\nu - b_\nu)\frac{\Delta\epsilon \cdot \epsilon}{\epsilon + \Delta\epsilon}\vec{E}_{z\nu} \cdot \vec{E}^*_{z\mu}] \exp(j\beta_\mu z)\end{aligned} \tag{3.25}$$

$$\begin{aligned}\frac{dB_\mu}{dz} =& j\omega \iint_{-\infty}^{\infty} dxdy \sum [(a_\nu + b_\nu)\Delta\epsilon \vec{E}_{t\nu} \cdot \vec{E}^*_{t\mu} \\ &- (a_\nu - b_\nu)\frac{\Delta\epsilon \cdot \epsilon}{\epsilon + \Delta\epsilon}\vec{E}_{z\nu} \cdot \vec{E}^*_{z\mu}] \exp(-j\beta_\mu z)\end{aligned} \tag{3.26}$$

Define the transverse and longitudinal coupling coefficients $K^t_{\nu\mu}$ and $K^z_{\nu\mu}$as

$$K^t_{\nu\mu} = \omega \iint_{-\infty}^{\infty} dxdy\Delta\epsilon \vec{E}_{t\nu} \cdot \vec{E}^*_{t\mu} \tag{3.27}$$

$$K^z_{\nu\mu} = \omega \iint_{-\infty}^{\infty} dxdy\frac{\Delta\epsilon \cdot \epsilon}{\epsilon + \Delta\epsilon} E_{z\nu} E^*_{z\mu} \tag{3.28}$$

And then the coupling equations become

$$\begin{aligned}\frac{dA_\mu}{dz} =& -j \sum \{A_\nu (K^t_{\nu\mu} + K^z_{\nu\mu}) exp[-j(\beta_\nu - \beta_\mu)z] \\ &+ B_\nu (K^t_{\nu\mu} - K^z_{\nu\mu}) exp[j(\beta_\nu + \beta_\mu)z]\}\end{aligned} \tag{3.29}$$

$$\begin{aligned}\frac{dB_\mu}{dz} =& j \sum \{A_\nu (K^t_{\nu\mu} - K^z_{\nu\mu}) exp[-j(\beta_\nu + \beta_\mu)z] \\ &+ B_\nu (K^t_{\nu\mu} + K^z_{\nu\mu}) exp[j(\beta_\nu - \beta_\mu)z]\}\end{aligned} \tag{3.30}$$

These are the general coupled-mode equations that find applications in various guided-wave optic problems. The application of coupled mode theory in fiber gratings has been treated thoroughly in [26] and [29].

A grating induced in fiber can be represented by a modulation of refractive index:

$$n(r, z) = n_0\{1 + \sigma(z)[1 + m\cos(\frac{2\pi}{\Lambda}z)]\} \tag{3.31}$$

The most important case for us is that $\sigma(z)$ is a constant:

$$n(r,z) = n_0 + n_0\sigma[1 + m\cos(\frac{2\pi}{\Lambda}z)] \tag{3.32}$$

In UV induced long-period gratings the modulation is limited in core region (In arc gratings the modulation exists in all layers). Comparing to [26], we use a slightly different form of mode normalization:

$$P = \frac{1}{2}Re\int_0^{2\pi} d\phi \int_0^{\infty} rdr(E_r^{cl}H_\phi^{cl*} - H_r^{cl*}E_\phi^{cl}) = 1W \tag{3.33}$$

In long-period gratings, core mode is always mode LP01. We consider core-core and core-cladding couplings and neglect cladding-cladding coupling since it is much weaker. In cylindrical coordinate equation (3.27) takes the form

$$K_{\nu\mu}^t(z) = \frac{\omega}{4}\int_0^{2\pi} d\phi \int_0^{\infty} rdr\Delta\epsilon(r,z)\vec{E}_\nu^t(r,\phi)\cdot\vec{E}_\mu^{t*}(r,\phi) \tag{3.34}$$

We only consider the transverse coupling coefficient because comparing to transverse components, the longitudinal components are much smaller. To be convenient for calculation, we write the coupling coefficient as

$$K_{\nu\mu}^t(z) = \tau + 2\kappa\cos\frac{2\pi}{\Lambda}z \tag{3.35}$$

$$\kappa = \frac{m}{2}\tau \tag{3.36}$$

where τ is the "dc" component of index change and m is the visibility of the grating. τ can be expressed as

$$\tau_{kj}(z) = \frac{\omega\epsilon_0 n_0^2\sigma}{2}\int_0^{2\pi} d\phi \int_0^{r_1} rdr\vec{E}_{kt}\cdot\vec{E}_{jt}^* \tag{3.37}$$

For guided-guided coupling ($LP_{01} - LP_{01}$):

$$\tau_{01-01}^{co-co} = \omega\epsilon_0 n_0^2 \sigma\pi \int_0^{r_1} rdr(|E_r^{co}|^2 + |E_\phi^{co}|^2) \tag{3.38}$$

where r_1 is the core radius. For guided-cladding coupling ($LP_{01} - M_{\nu\mu}$), the angular part of coupling coefficient is

$$\int_0^{2\pi} d\phi exp[i(\nu - 1)\phi] = 2\pi\delta_{\nu 1} \tag{3.39}$$

This means coupling take place only between core mode and cladding modes with angular order $\nu = 1$. Thus the core-cladding coupling coefficient can be expressed as

$$\tau_{01-1\nu}^{co-cl} = \omega\epsilon_0 n_0^2 \sigma\pi \int_0^{r_1} rdr(E_r^{cl} E_r^{co*} + E_\phi^{cl} E_\phi^{co*}) \tag{3.40}$$

For simplicity we only consider coupling between core mode and one cladding mode. The coupled mode equations for LP_{01} guided mode and $M_{1\mu}$ cladding mode can be expressed as

$$\frac{dA^{co}}{dz} = iK_{01-01}^{co-co} A^{co} + iK_{1\nu-01}^{cl-co} A_\nu^{cl} exp[i(\beta_\nu^{cl} - \beta^{co})z] \tag{3.41}$$

$$\frac{dA_\nu^{cl}}{dz} = iK_{01-1\nu}^{co-cl} A^{co} exp[i(\beta^{co} - \beta_\nu^{cl})z] \tag{3.42}$$

Let

$$\delta = \frac{1}{2}(\beta^{co} - \beta_\nu^{cl} - \frac{2\pi}{\Lambda}) \tag{3.43}$$

$$\hat{\sigma} = \frac{\tau^{co-co}}{2} + \delta \tag{3.44}$$

$$\kappa = \kappa_{1\nu-01}^{cl-co} = \kappa_{01-1\nu}^{co-cl*} \tag{3.45}$$

$$R = A^{co} exp[i(-\frac{\tau^{co-co}}{2} + \delta)z] \tag{3.46}$$

$$S = A^{cl}_{\nu} exp[i(-\frac{\tau^{co-co}}{2} - \delta)z] \tag{3.47}$$

Then

$$\frac{dR}{dz} = i\hat{\sigma}R + i\kappa S \tag{3.48}$$

$$\frac{dS}{dz} = -i\hat{\sigma}S + i\kappa^* R \tag{3.49}$$

The boundary condition for this problem is $|S(0)| = 0$, and the transmission of grating can be expressed as

$$\begin{aligned} T &= \frac{R(L)}{R(0)} \\ &= \cos^2(\sqrt{\hat{\sigma}^2 + \kappa^2}L) + \frac{\hat{\sigma}^2}{\hat{\sigma^2} + \kappa^2}\sin^2(\sqrt{\hat{\sigma}^2 + \kappa^2}L) \end{aligned} \tag{3.50}$$

Up to now we have presented a coupled-mode formalism for long-period gratings. The approximations we have made are:

1. Neglect all the off-resonant modes when computing certain mode

2. Neglect the longitudinal mode coupling

3. Neglect the cladding-cladding coupling

Effective refractive index and field distribution of modes

The method to solve effective index and field distribution of core and cladding modes are presented here. In this thesis we are only concerned with step index

fibers, where the refractive index is constant in each layer. In this case, analytical expression of general solution in each layer is available and the unknown constants in these general solutions are determined by boundary conditions. This is a straightforward process, but a potential problem is that when there are many layers in a fiber, the number of boundary conditions will be very large since at each boundary there are four independent boundary conditions. Solving for the unknown coefficients then involves manipulating matrices with very large dimensions which is time consuming. Here we follow the approach of Yeh where a transfer matrix type of formalism is adopted and the dimension of matrix involved in the calculation is always four, which significantly increases the computation speed [27, 28].

Light propagating in a fiber is governed by wave equation. Consider a fiber with $N+1$ layers and N boundaries, if the refractive index of the mth layer is n_m and define $k_m = 2\pi n_m/\lambda$ where λ is the wavelength of light in vacuum, then in cylindrical coordinate (r, θ, z) we have

$$\nabla^2 E_r - \frac{2}{r^2}\frac{\partial E_\theta}{\partial \theta} - \frac{E_r}{r^2} + k^2 E_r = 0 \tag{3.51}$$

$$\nabla^2 E_\theta + \frac{2}{r^2}\frac{\partial E_r}{\partial \theta} - \frac{E_\theta}{r^2} + k^2 E_\theta = 0 \tag{3.52}$$

$$\nabla^2 E_z + k^2 E_z = 0 \tag{3.53}$$

where the operator ∇^2 is defined by

$$\nabla^2 \psi = \frac{1}{r}\frac{\partial}{\partial r}(r\frac{\partial \psi}{\partial r}) + \frac{1}{r^2}\frac{\partial^2 \psi}{\partial \theta^2} + \frac{\partial^2 \psi}{\partial z^2}$$

Equations for magnetic fields are of the same form. The transverse (r- and

θ-) components couple with each other while the longitudinal (z-) component is decoupled from other components. Thus the longitudinal component can be solved first, and then the transverse components can be obtained through the transverse-longitude relations [20]

$$E_r = -\frac{1}{(k_m n_m)^2 - \beta^2}(\frac{\nu\omega\mu_0}{r}H_z - i\beta\frac{\partial E_z}{\partial r}) \tag{3.54}$$

$$E_\theta = -\frac{1}{(k_m n_m)^2 - \beta^2}(i\omega\mu_0\frac{\partial H_z}{\partial r} + \frac{\beta\nu}{r}E_z) \tag{3.55}$$

$$H_r = \frac{1}{(k_m n_m)^2 - \beta^2}(\frac{\nu {n_m}^2\epsilon_0\omega E_z}{r} + i\beta\frac{\partial H_z}{\partial r}) \tag{3.56}$$

$$H_\theta = \frac{1}{(k_m n_m)^2 - \beta^2}(i{n_m}^2\epsilon_0\omega\frac{\partial E_z}{\partial r} - \frac{\beta\nu}{r}H_z) \tag{3.57}$$

The z-component satisfies the equation

$$\frac{1}{r}\frac{\partial}{\partial r}(r\frac{\partial E_z}{\partial r}) + \frac{1}{r^2}\frac{\partial^2 E_z}{\partial\theta^2} + \frac{\partial^2 E_z}{\partial z^2} + k^2 E_z = 0 \tag{3.58}$$

This equation can be solved by separating variables and E_z can be written in the general form

$$E_z = E_z(r)e^{i\nu\theta}e^{i\beta z}$$

which yields

$$\frac{d^2 E_z(r)}{dr^2} + \frac{1}{r}\frac{dE_z(r)}{dr} + [({k_m}^2 - \beta^2) - \frac{\nu^2}{r^2}]E_z(r) = 0 \tag{3.59}$$

and for magnetic field there is a similar equation. Here β is related to the effective refractive index by

$$\beta = \frac{2\pi}{\lambda}n_{eff} \tag{3.60}$$

Define $p_m^2 = (k_m n_m)^2 - \beta^2$ and $q_m^2 = \beta^2 - (k_m n_m)^2$, the general solution in each layer can be expressed as:

Layer 1:

$$E_z^{(1)} = C_1 J_\nu(p_1 r) \tag{3.61}$$

$$H_z^{(1)} = iD_1 J_\nu(p_1 r) \tag{3.62}$$

Layer m(1<m<N+1):

For guided wave ($k_m > \beta$):

$$E_z^{(m)} = C_m J_\nu(p_m r) + C'_m Y_\nu(p_m r) \tag{3.63}$$

$$H_z^{(m)} = iD_m J_\nu(p_m r) + iD'_m Y_\nu(p_m r) \tag{3.64}$$

For evanescent wave ($k_m < \beta$):

$$E_z^{(m)} = C_m I_\nu(q_m r) + C'_m K_\nu(q_m r) \tag{3.65}$$

$$H_z^{(m)} = iD_m I_\nu(q_m r) + iD'_m K_\nu(q_m r) \tag{3.66}$$

Layer N+1:

$$E_z^{(N+1)} = EK_\nu(q_{N+1} r) \tag{3.67}$$

$$H_z^{(N+1)} = iFK_\nu(q_{N+1} r) \tag{3.68}$$

From z-components we can obtain r- and θ- components:

Layer 1:

$$E_r^{(m)} = i\frac{\beta}{p_m}J'_\nu(p_m r)C_m - i\frac{\nu\omega\mu_0}{p_m^2 r}J_\nu(p_m r)D_m \tag{3.69}$$

$$H_r^{(m)} = \frac{\nu n_m^2\epsilon_0\omega}{p_m^2 r}J_\nu(p_m r)C_m - \frac{\beta}{p_m}J'_\nu(p_m r)D_m \tag{3.70}$$

$$E_\theta^{(m)} = -\frac{\beta\nu}{p_m^2 r}J_\nu(p_m r)C_m + \frac{\omega\mu_0}{p_m}J'_\nu(p_m r)D_m \tag{3.71}$$

$$H_\theta^{(m)} = i\frac{n_m^2\epsilon_0\omega}{p_m}J'_\nu(p_m r)C_m - i\frac{\beta\nu}{p_m^2 r}J_\nu(p_m r)D_m \tag{3.72}$$

Layer m(1<m<N+1):

For guided wave ($k_m > \beta$),

$$\begin{aligned} E_r^{(m)} &= i\frac{\beta}{p_m}J'_\nu(p_m r)C_m - i\frac{\nu\omega\mu_0}{p_m^2 r}J_\nu(p_m r)D_m \\ &+ i\frac{\beta}{p_m}Y'_\nu(p_m r)C'_m - i\frac{\nu\omega\mu_0}{p_m^2 r}Y_\nu(p_m r)D'_m \end{aligned} \tag{3.73}$$

$$\begin{aligned} H_r^{(m)} &= \frac{\nu n_m^2\epsilon_0\omega}{p_m^2 r}J_\nu(p_m r)C_m - \frac{\beta}{p_m}J'_\nu(p_m r)D_m \\ &+ \frac{\nu n_m^2\epsilon_0\omega}{p_m^2 r}Y_\nu(p_m r)C'_m - \frac{\beta}{p_m}Y'_\nu(p_m r)D'_m \end{aligned} \tag{3.74}$$

$$\begin{aligned} E_\theta^{(m)} &= -\frac{\beta\nu}{p_m^2 r}J_\nu(p_m r)C_m + \frac{\omega\mu_0}{p_m}J'_\nu(p_m r)D_m \\ &- \frac{\beta\nu}{p_m^2 r}Y_\nu(p_m r)C'_m + \frac{\omega\mu_0}{p_m}Y'_\nu(p_m r)D'_m \end{aligned} \tag{3.75}$$

$$\begin{aligned} H_\theta^{(m)} &= i\frac{n_m^2\epsilon_0\omega}{p_m}J'_\nu(p_m r)C_m - i\frac{\beta\nu}{p_m^2 r}J_\nu(p_m r)D_m \\ &+ i\frac{n_m^2\epsilon_0\omega}{p_m}Y'_\nu(p_m r)C'_m - i\frac{\beta\nu}{p_m^2 r}Y_\nu(p_m r)D'_m \end{aligned} \tag{3.76}$$

For evanescent wave ($k_m < \beta$),

$$E_r^{(m)} = -i\frac{\beta}{q_m}I'_\nu(q_m r)C_m + i\frac{\nu\omega\mu_0}{q_m^2 r}I_\nu(q_m r)D_m - i\frac{\beta}{q_m}K'_\nu(q_m r)C'_m + i\frac{\nu\omega\mu_0}{q_m^2 r}K_\nu(q_m r)D'_m \tag{3.77}$$

$$H_r^{(m)} = -\frac{\nu n_m^2\epsilon_0\omega}{q_m^2 r}I_\nu(q_m r)C_m + \frac{\beta}{q_m}I'_\nu(q_m r)D_m - \frac{\nu n_m^2\epsilon_0\omega}{q_m^2 r}K_\nu(q_m r)C'_m + \frac{\beta}{q_m}K'_\nu(q_m r)D'_m \tag{3.78}$$

$$E_\theta^{(m)} = \frac{\beta\nu}{q_m^2 r}J_\nu(q_m r)C_m - \frac{\omega\mu_0}{q_m}J'_\nu(q_m r)D_m + \frac{\beta\nu}{q_m^2 r}Y_\nu(q_m r)C'_m - \frac{\omega\mu_0}{q_m}Y'_\nu(q_m r)D'_m \tag{3.79}$$

$$H_\theta^{(m)} = -i\frac{n_m^2\epsilon_0\omega}{q_m}I'_\nu(q_m r)C_m + i\frac{\beta\nu}{q_m^2 r}I_\nu(q_m r)D_m - i\frac{n_m^2\epsilon_0\omega}{q_m}K'_\nu(q_m r)C'_m + i\frac{\beta\nu}{q_m^2 r}K_\nu(q_m r)D'_m \tag{3.80}$$

Layer N+1:

$$E_r^{(N+1)} = -i\frac{\beta}{q_{N+1}}K'_\nu(q_{N+1} r)E + i\frac{\nu\omega\mu_0}{q_{N+1}^2 r}K_\nu(q_{N+1} r)F \tag{3.81}$$

$$H_r^{(N+1)} = -\frac{\nu n_{N+1}^2\epsilon_0\omega}{q_{N+1}^2 r}K_\nu(q_{N+1} r)E + \frac{\beta}{q_{N+1}}K'_\nu(q_{N+1} r)F \tag{3.82}$$

$$E_\theta^{(N+1)} = \frac{\beta\nu}{q_{N+1}^2 r}Y_\nu(q_{N+1} r)E - \frac{\omega\mu_0}{q_{N+1}}Y'_\nu(q_{N+1} r)F \tag{3.83}$$

$$H_\theta^{(N+1)} = -i\frac{n_{N+1}^2\epsilon_0\omega}{q_{N+1}}K'_\nu(q_{N+1} r)E + i\frac{\beta\nu}{q_{N+1}^2 r}K_\nu(q_{N+1} r)F \tag{3.84}$$

In these expressions $C_1, D_1, C_m, D_m, C'_m, D'_m, E, F$ are coefficients to be determined. Now that the general solution in each layer is obtained, the next step is to determine these coefficients through boundary conditions. For this purpose, we first express fields in different layers in matrix form:

Layer 1:

$$\begin{pmatrix} E_z^{(1)} \\ -iH_z^{(1)} \\ E_\theta^{(1)} \\ -iH_\theta^{(1)} \end{pmatrix} = M_1 \begin{pmatrix} C_1 \\ D_1 \\ 0 \\ 0 \end{pmatrix} \tag{3.85}$$

Layer m (1<m<N+1):

$$\begin{pmatrix} E_z^{(m)} \\ -iH_z^{(m)} \\ E_\theta^{(m)} \\ -iH_\theta^{(m)} \end{pmatrix} = M_m \begin{pmatrix} C_m \\ D_m \\ C'_m \\ D'_m \end{pmatrix} \tag{3.86}$$

Layer N+1:

$$\begin{pmatrix} E_z^{(N+1)} \\ -iH_z^{(N+1)} \\ E_\theta^{(N+1)} \\ -iH_\theta^{(N+1)} \end{pmatrix} = M_{N+1} \begin{pmatrix} 0 \\ 0 \\ E \\ F \end{pmatrix} \tag{3.87}$$

where

$$M_1(r) = \begin{pmatrix} J_\nu(p_1 r) & 0 & 0 & 0 \\ 0 & J_\nu(p_1 r) & 0 & 0 \\ -\frac{\beta\nu}{p_1^2 r} J_\nu(p_1 r) & \frac{\omega\mu_0}{p_1} J'_\nu(p_1 r) & 0 & 0 \\ \frac{n_1^2 \epsilon_0 \omega}{p_1} J'_\nu(p_1 r) & -\frac{\beta\nu}{p_1^2 r} J_\nu(p_1 r) & 0 & 0 \end{pmatrix} \tag{3.88}$$

$$M_m(r) = \begin{pmatrix} J_\nu(p_m r) & 0 & Y_\nu(p_m r) & 0 \\ 0 & J_\nu(p_m r) & 0 & Y_\nu(p_m r) \\ -\frac{\beta\nu}{p_m^2 r} J_\nu(p_m r) & \frac{\omega\mu_0}{p_m} J'_\nu(p_m r) & -\frac{\beta\nu}{p_m^2 r} Y_\nu(p_m r) & \frac{\omega\mu_0}{p_m} Y'_\nu(p_m r) \\ \frac{n_m^2\epsilon_0\omega}{p_m} J'_\nu(p_m r) & -\frac{\beta\nu}{p_m^2 r} J_\nu(p_m r) & \frac{n_m^2\epsilon_0\omega}{p_m} Y'_\nu(p_m r) & -\frac{\beta\nu}{p_m^2 r} Y_\nu(p_m r) \end{pmatrix} \tag{3.89}$$

for guided wave or

$$M_m(r) = \begin{pmatrix} I_\nu(q_m r) & 0 & K_\nu(q_m r) & 0 \\ 0 & I_\nu(q_m r) & 0 & K_\nu(q_m r) \\ \frac{\beta\nu}{q_m^2 r} I_\nu(q_m r) & -\frac{\omega\mu_0}{q_m} I'_\nu(q_m r) & \frac{\beta\nu}{q_m^2 r} K_\nu(q_m r) & -\frac{\omega\mu_0}{q_m} K'_\nu(q_m r) \\ -\frac{n_m^2\epsilon_0\omega}{q_m} I'_\nu(q_m r) & \frac{\beta\nu}{q_m^2 r} I_\nu(q_m r) & -\frac{n_m^2\epsilon_0\omega}{q_m} K'_\nu(q_m r) & \frac{\beta\nu}{q_m^2 r} K_\nu(q_m r) \end{pmatrix} \tag{3.90}$$

for evanescent wave;

$$M_{N+1}(r) = \begin{pmatrix} 0 & 0 & K_\nu(q_{N+1} r) & 0 \\ 0 & 0 & 0 & K_\nu(q_{N+1} r) \\ 0 & 0 & \frac{\beta\nu}{q_{N+1}^2 r} K_\nu(q_{N+1} r) & -\frac{\omega\mu_0}{q_{N+1}} K'_\nu(q_{N+1} r) \\ 0 & 0 & -\frac{n_1^2\epsilon_0\omega}{q_{N+1}} K'_\nu(q_{N+1} r) & \frac{\beta\nu}{q_{N+1}^2 r} K_\nu(q_{N+1} r) \end{pmatrix} \tag{3.91}$$

In order to satisfy the electromagnetic boundary conditions, all these four components must be continuous at the boundary between adjacent layers:

$$M_m(r_m) \begin{pmatrix} C_m \\ D_m \\ C'_m \\ D'_m \end{pmatrix} = M_{m+1}(r_m) \begin{pmatrix} C_{m+1} \\ D_{m+1} \\ C'_{m+1} \\ D'_{m+1} \end{pmatrix}, m = 1, 2, \cdots, N-1 \tag{3.92}$$

$$M_m(r_m)\begin{pmatrix} C_m \\ D_m \\ C'_m \\ D'_m \end{pmatrix} = M_{N+1}(r_m)\begin{pmatrix} 0 \\ 0 \\ E \\ F \end{pmatrix} \tag{3.93}$$

where r_m is the radius at the m'th boundary. Thus we can write

$$\begin{aligned} M_1(r_1)\begin{pmatrix} C_1 \\ D_1 \\ 0 \\ 0 \end{pmatrix} &= M_2(r_1)M_2^{-1}(r_2)\cdots M_m(r_{N-1})M_m^{-1}(r_m)M_{N+1}(r_m)\begin{pmatrix} 0 \\ 0 \\ E \\ F \end{pmatrix} \\ &= M\begin{pmatrix} 0 \\ 0 \\ E \\ F \end{pmatrix} \end{aligned} \tag{3.94}$$

where

$$M = M_2(r_1)M_2^{-1}(r_2)\cdots M_m(r_{N-1})M_m^{-1}(r_N)M_{N+1}(r_N) \tag{3.95}$$

This can be rewritten as

$$\begin{pmatrix} J_\nu(p_1r_1) & 0 & -M_{13} & -M_{14} \\ 0 & J_\nu(p_1r_1) & -M_{23} & -M_{24} \\ -\frac{\beta\nu}{p_1^2r_1}J_\nu(p_1r_1) & \frac{\omega\mu_0}{p_1}J'_\nu(p_1r_1) & -M_{33} & -M_{34} \\ \frac{n_1^2\epsilon_0\omega}{p_1}J'_\nu(p_1r_1) & -\frac{\beta\nu}{p_1^2r_1}J_\nu(p_1r_1) & -M_{43} & -M_{44} \end{pmatrix}\begin{pmatrix} C_1 \\ D_1 \\ E \\ F \end{pmatrix} = 0 \tag{3.96}$$

In order to have nontrivial solution the determinant of the matrix must be zero.

Therefore, β and hence n_{eff} can be solved from the equation:

$$\begin{vmatrix} J_\nu(p_1r_1) & 0 & -M_{13} & -M_{14} \\ 0 & J_\nu(p_1r_1) & -M_{23} & -M_{24} \\ -\frac{\beta\nu}{p_1^2r_1}J_\nu(p_1r_1) & \frac{\omega\mu_0}{p_1}J'_\nu(p_1r_1) & -M_{33} & -M_{34} \\ \frac{n_1^2\epsilon_0\omega}{p_1}J'_\nu(p_1r_1) & -\frac{\beta\nu}{p_1^2r_1}J_\nu(p_1r_1) & -M_{43} & -M_{44} \end{vmatrix} = 0 \tag{3.97}$$

Once β is known, it is straight forward to calculate the field coefficients. First, C_1, D_1, E and F are solved from equation (3.96). Then the coefficients for other layers can obtained by

$$\begin{pmatrix} C_i \\ D_i \\ C'_i \\ D'_i \end{pmatrix} = M_i^{-1}(r_{i-1})M_{i-1}(r_{i-1})\cdots M_2^{-1}(r_1)M_1(r_1)\begin{pmatrix} C_1 \\ D_1 \\ 0 \\ 0 \end{pmatrix} \quad (1 < i < N+1) \tag{3.98}$$

Thus the field distributions in different layers can be calculated using equations (3.85) to (3.87). The Poynting flux in the mth layer is given by

$$S_z(m) = \frac{1}{2}Re[E_r(m)H_\phi(m)^* - E_\phi(m)H_r(m)^*] \tag{3.99}$$

The radial components can be calculated using the transverse-longitude relationship (3.54) to (3.57). For the convenience of programming they are listed together with the azimuthal components:

$$\begin{pmatrix} E_r^{(1)} \\ E_\theta^{(1)} \\ H_r^{(1)} \\ H_\theta^{(1)} \end{pmatrix} = \begin{pmatrix} i\frac{\beta}{p_1}J'_\nu(p_1r) & -i\frac{\nu\omega\mu_0}{p_1^2 r}J_\nu(p_1r) & 0 & 0 \\ -\frac{\beta\nu}{p_1^2 r}J_\nu(p_1r) & \frac{\omega\mu_0}{p_1}J'_\nu(p_1r) & 0 & 0 \\ \frac{\nu n_1^2\epsilon_0\omega}{p_1^2 r}J_\nu(p_1r) & -\frac{\beta}{p_1}J'_\nu(p_1r) & 0 & 0 \\ \frac{in_1^2\epsilon_0\omega}{p_1}J'_\nu(p_1r) & -i\frac{\beta\nu}{p_1^2 r}J_\nu(p_1r) & 0 & 0 \end{pmatrix} \begin{pmatrix} C_1 \\ D_1 \\ 0 \\ 0 \end{pmatrix} \tag{3.100}$$

$$\begin{pmatrix} E_r^{(m)} \\ E_\theta^{(m)} \\ H_r^{(m)} \\ H_\theta^{(m)} \end{pmatrix} =$$

$$\begin{pmatrix} i\frac{\beta}{p_m}J'_\nu(p_mr) & -i\frac{\nu\omega\mu_0}{p_m^2 r}J_\nu(p_mr) & i\frac{\beta}{p_m}Y'_\nu(p_mr) & -i\frac{\nu\omega\mu_0}{p_m^2 r}Y_\nu(p_mr) \\ -\frac{\beta\nu}{p_m^2 r}J_\nu(p_mr) & \frac{\omega\mu_0}{p_m}J'_\nu(p_mr) & -\frac{\beta\nu}{p_m^2 r}Y_\nu(p_mr) & \frac{\omega\mu_0}{p_m}Y'_\nu(p_mr) \\ \frac{\nu n_m^2\epsilon_0\omega}{p_m^2 r}J_\nu(p_mr) & -\frac{\beta}{p_m}J'_\nu(p_mr) & \frac{\nu n_m^2\epsilon_0\omega}{p_m^2 r}Y_\nu(p_mr) & -\frac{\beta}{p_m}Y'_\nu(p_mr) \\ \frac{in_n^2\epsilon_0\omega}{p_n}J'_\nu(p_nr) & -i\frac{\beta\nu}{p_n^2 r}J_\nu(p_nr) & \frac{in_n^2\epsilon_0\omega}{p_n}Y'_\nu(p_nr) & -i\frac{\beta\nu}{p_n^2 r}Y_\nu(p_nr) \end{pmatrix} \tag{3.101}$$

$$\times \begin{pmatrix} C_m \\ D_m \\ C'_m \\ D'_m \end{pmatrix} \quad (1 < m < N+1)$$

$$\begin{pmatrix} E_r^{(N+1)} \\ E_\theta^{(N+1)} \\ H_r^{(N+1)} \\ H_\theta^{(N+1)} \end{pmatrix} = \begin{pmatrix} 0 & 0 & -i\frac{\beta}{q_{N+1}}K'_\nu(q_{N+1}r) & i\frac{\nu\omega\mu_0}{q_{N+1}^2 r}K_\nu(q_{N+1}r) \\ 0 & 0 & \frac{\beta\nu}{q_{N+1}^2 r}K_\nu(q_{N+1}r) & -\frac{\omega\mu_0}{q_{N+1}}K'_\nu(q_{N+1}r) \\ 0 & 0 & -\frac{\nu n_{N+1}^2\epsilon_0\omega}{q_{N+1}^2 r}K_\nu(q_{N+1}r) & \frac{\beta}{q_{N+1}}K'_\nu(q_{N+1}r) \\ 0 & 0 & -\frac{in_{N+1}^2\epsilon_0\omega}{q_{N+1}}K'_\nu(q_{N+1}r) & i\frac{\beta\nu}{q_{N+1}^2 r}K_\nu(q_{N+1}r) \end{pmatrix} \begin{pmatrix} 0 \\ 0 \\ E \\ F \end{pmatrix} \tag{3.102}$$

The total power carried by certain mode is

$$\begin{aligned} P = &\int_0^{r_1} \frac{1}{2} Re[E_r(1)H_\phi(1)^* - E_\phi(1)H_r(1)^*]2\pi r dr \\ &+ \sum_{k=2}^{m} \int_{r_{N-1}}^{r_m} \frac{1}{2} Re[E_r(m)H_\phi(m)^* - E_\phi(m)H_r(m)^*]2\pi r dr \\ &+ \int_{r_m}^{+\infty} \frac{1}{2} Re[E_r(N+1)H_\phi(N+1)^* - E_\phi(N+1)H_r(N+1)^*]2\pi r dr \end{aligned} \tag{3.103}$$

Including the optical loss

In the above formulation it is assumed that all the layers are made of perfectly transparent materials with no loss. In real devices there are many cases where the optical losses need to be considered, such as the finite absorption in ITO layers or metal layers and the scattering loss in polymers. These losses can be included into the model by including the imaginary part of refractive index:

$$n_m = n'_m + in''_m \tag{3.104}$$

where m denotes the layer number. Accordingly, the effective refractive index will be generally also a complex number:

$$n_{eff} = n'_{eff} + in''_{eff} \tag{3.105}$$

Therefore, the complex eigen equation can be separated into two real equations involving the real and imaginary parts:

$$E(n_{eff}) = R(n'_{eff}, n''_{eff}) + iI(n'_{eff}, n''_{eff}) = 0 \tag{3.106}$$

and hence

$$R(n'_{eff}, n''_{eff}) = 0 \tag{3.107}$$

$$I(n'_{eff}, n''_{eff}) = 0 \tag{3.108}$$

or equivalently

$$R^2(n'_{eff}, n''_{eff}) + I^2(n'_{eff}, n''_{eff}) = 0 \tag{3.109}$$

The numerical methods used for solving the eigen equation in the lossless case cannot be directly applied to solve this equation as two variables are involved. On the other hand, solving equation (3.109) is equivalent to solving the minimization problem

$$min(R^2 + I^2) \tag{3.110}$$

since $R^2 + I^2$ is non-negative. This minimization problem can be easily solved using the global optimization programs provided by many standard computational packages (e.g. in Matlab).

3.3 Results of computer simulation of LPG

The tunable LPG under consideration has six layers (Figure 3.3), namely, core, cladding, ITO inner electrode, polymer, metal outer electrode, and the external medium. However, since the polymer thickness is quite large so that the intensity

of light decreases to nearly zero at the outer diameter of the polymer, I omit the metal layer and the external medium and treat the polymer layer as infinitely thick, which significantly reduced complexity of simulatio while still maintain the key features of the model and the basic physics. Therefore, a four-layered structure is used in the computer simulation (Figure 3.4).

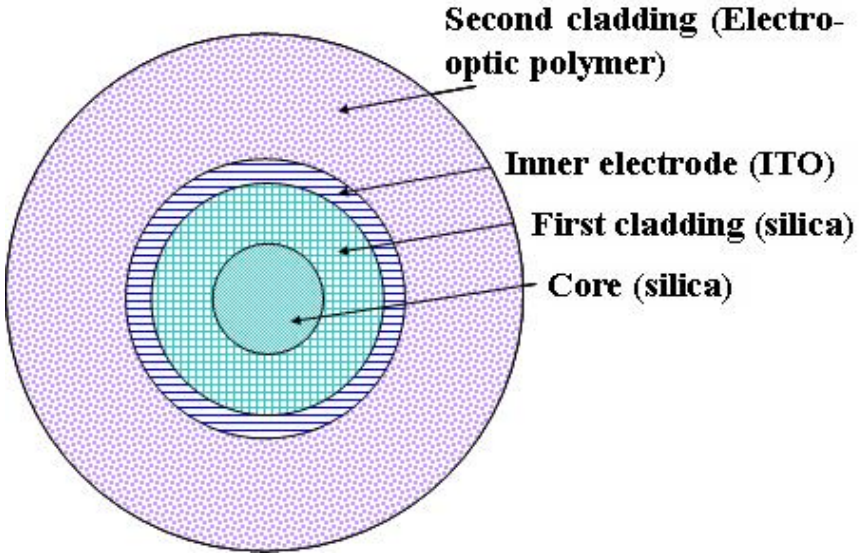

Figure 3.4. The cross-sectional view of the 4-layered fiber structure used in the computer simulation.

The model described in last section is capable of calculating the entire transmission spectrum of an LPG which shows the notch that is induced by coupling (Figure 3.5). In the design of tunable LPG we are interested in resonance wavelength shift $\Delta\lambda_0$ and transmittance T at resonance wavelength which is related to the depth of the notch. Therefore, we are interested in the effective index of cladding mode n_{eff}^{cl} and the coupling coefficient κ between core and cladding modes, because they are related to $\Delta\lambda_0$ and T by

$$\Delta\lambda_0 = -\Delta n_{eff}^{cl}\Lambda \tag{3.111}$$

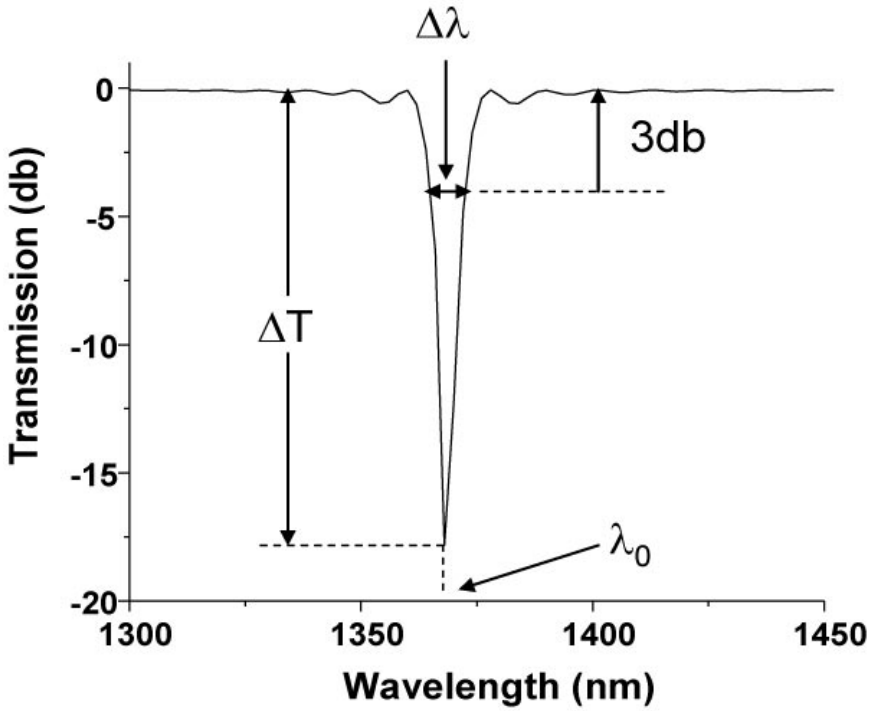

Figure 3.5. An example of the calculated transmission spectrum of an LPG, showing some critical parameters of the LPG: resonance wavelength (λ_0), notch depth (ΔT), and bandwidth ($\Delta\lambda$).

and

$$T = \cos^2(\kappa L) \tag{3.112}$$

which are derived from equations (3.4) and (3.50). Here L is the length of the grating. Effective index of core mode doesn't appear in these equations because the energy of core mode in polymer layer is essentially zero and we can assume that the core mode is completely not affected by the refractive index change. It should be noted that the above two equations are approximate. Precise value of the center wavelength and depth of the notch should be found by calculating the entire transmission spectrum, which is much more time consuming. However, as will be discussed later, even if the simulation itself is completely precise, the

uncertainties in material parameters will cause errors. Therefore, we focus on the effects of various device parameters on the tuning and mechanisms of such effects rather than exact values in the simulation. In this sense, the above two expressions provide enough information yet are relatively fast to calculate.

It should be also mentioned that the formulation developed here has assumed perfect periodicity of the grating. This is an ideal case since real gratings always have finite length. However, we expect that the error introduced by this issue will be small as long as the number of periods in the grating is not too small.

Since only cladding modes with $\nu = 1$ has non-zero coupling coefficients, we neglect ν in the designation of mode number and denote the modes with a single number.

A summary of simulation results

Table 3.1 lists the parameters used in the simulation as well as the core mode effective index and self-coupling coefficient which are constants in our discussion here. Here τ^{co-co} denotes the self-coupling coefficient of the core mode and the fringe modulation in the grating corresponds to the parameter m in equation (3.31) and is related to the maximum refractive index change Δn in the grating by $\Delta n = 2mn_{co}$.

Strictly speaking, ITO is not perfectly transparent and has certain optical loss. The exact value of imaginary part (n'') of refractive index of ITO depends on the deposition condition. Under the conditions used in our experiment, n'' is smaller than 0.01 [32]. We calculated the difference between the LPG parameters when $n'' = 0$ and $n'' = 0.01$ (Figure 3.6) [28]. The parameters used in simulation are: cladding diameter 35μm, ITO thickness 50nm, ITO refractive index 1.8. It

Parameter	Value
Wavelength	1550nm
Core diameter	8.3μm
Core index	1.4491
Cladding diameter	varies
Cladding index	1.4441
ITO thickness	varies
ITO index	varies
Fringe modulation	3.5×10^{-4}
n_{eff}^{co}	1.446107
τ^{co-co}	780.5 m^{-1}

Table 3.1. The parameters used in simulation and the calculated parameters of core mode.

is evident that optical loss in ITO with $n'' = 0.01$ has negligible effect on the effective refractive index of cladding modes. On the other hand, the attenuation of cladding mode induced by the loss in ITO is rather significant. For instance, taking the typical value for Im(n_{eff}) of 0.0001 the attenuation factor for an LPG (length L=8mm) at 1550nm wavelength is $\exp[\text{Im}(n_{eff})\frac{2\pi}{\lambda}L] \approx 25$. However, since the attenuation of cladding mode does not significantly affect the effective index, in the following discussion of tuning the effect of non-zero n'' can be neglected. Therefore, in the following simulations ITO is treated as a perfectly transparent layer.

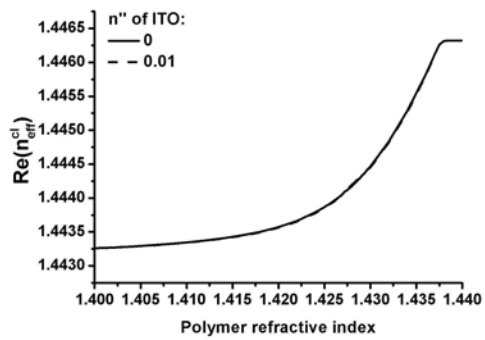

(a) Re(n_{eff}), 1st mode

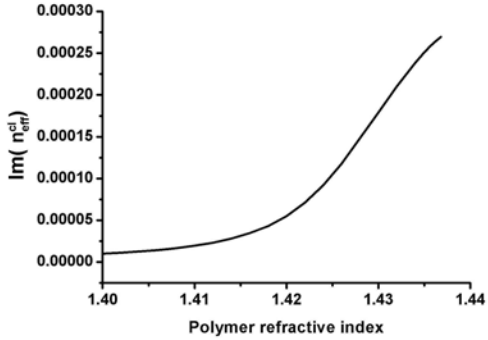

(b) Im(n_{eff}), 1st mode

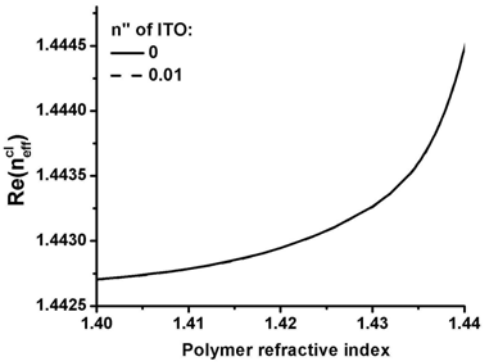

(c) Re(n_{eff}), 2nd mode

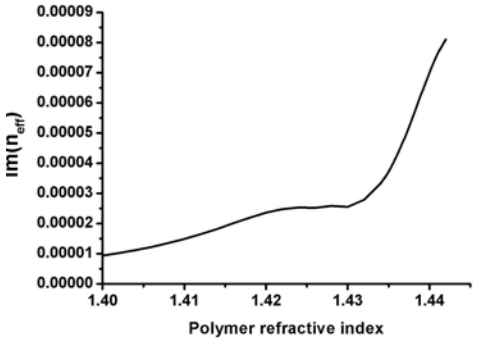

(d) Im(n_{eff}), 2nd mode

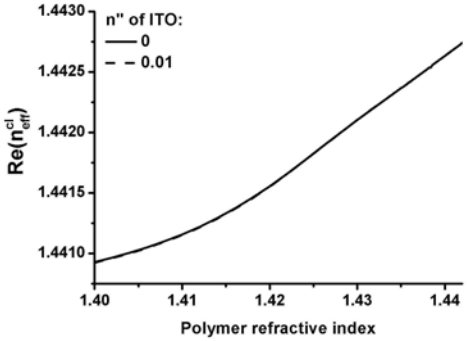

(e) Re(n_{eff}), 3rd mode

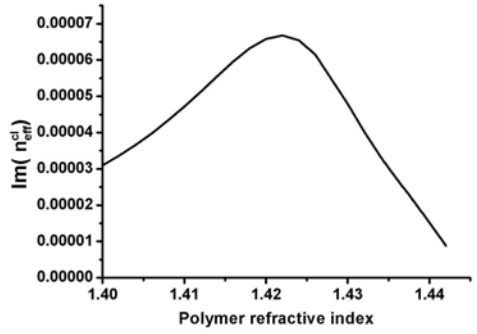

(f) Im(n_{eff}), 3rd mode

Figure 3.6. The effect of the imaginary part of ITO refractive index (n'') on the real and imaginary parts of the effective refractive index of the *1st* to *3rd* cladding modes.

The effect of ITO thickness on the effective refractive indexes and coupling coefficients of the first to third cladding modes are summarized in Figure 3.7. For a grating with period of 400μm, using equation (3.3) we can derive two rule-of-thumbs:

- $\Delta n_{eff}^{cl} = 0.0001$ corresponds to wavelength shift of 40nm
- Resonance wavelengths of 1550nm corresponds to $n_{eff}^{cl} = 1.442232$

The parameters used in simulation are: cladding diameter 40μm, ITO refractive index 1.8. For all the ITO thicknesses, n_{eff} show a common trend that it increases slowly with polymer refractive index n_{poly} when n_{poly} is low, but increases much faster when n_{poly} is large. Without ITO (0nm), the n_{eff} curve is almost flat up to $n_{poly} \sim 1.44$ but increases dramatically when n_{poly} is close to $n_{cl} = 1.444$. This means large tuning can be only achieved at very close to n_{cl}. However, as shown in Figures 3.7b,d,f, at close to n_{cl} the coupling coefficient κ also changes dramatically with n_{poly}, which means when the resonance wavelength is shifted the notch depth will change a lot, which is certainly undesirable. With increasing ITO thickness, n_{eff} increases more uniformly over the entire range of n_{poly} and much faster comparing to the flat curve portion in the non-ITO case. The increased thickness of ITO also effectively shifts the entire curve to lower polymer index. Furthermore, turn points can be observed in the κ-n_{poly} curves. For instance, in Figure 3.7f κ varies slowly with n_{poly} near point B. On the other hand, near point A in Figure 3.7e which corresponds to the same n_{poly} and ITO thickness as point B, n_{eff}^{cl} still changes fast with n_{poly}. This means that large tuning can be achieved while maintaining a small variation of notch depth. This is important for tunable LPGs and is a unique feature brought by the ITO layer. According to equation (3.4), at point A (ITO thickness 70nm, $n_{poly} = 1.42$) $\Delta n_{poly} = 0.004$ is required to

achieve tuning range of 40nm. This refractive index change is readily achievable by P(VDF-TrFE-CFE) terpolymer.

The effect of the refractive index of ITO on effective index and coupling coefficient is illustrated in Figure 3.8. The parameters used in simulation are: cladding diameter 40μm, ITO thickness 50nm. Generally speaking, the effects of ITO refractive index and ITO thickness are very similar. This can be understood by the fact that qualitatively speaking, it is the optical thickness (product of thickness and refractive index) rather than thickness or refractive index itself that determines the effect of ITO on fiber modes.

The effect of the diameter of fiber on effective index and coupling coefficient is illustrated in Figure 3.9. The parameters used in simulation are: core diameter 8.3μm, ITO thickness 50nm, ITO refractive index 1.8. The range of diameter under investigation is much smaller than the original diameter of fiber (125μm). This is because the tuning range of LPGs with reduced diameters is much larger than those with large diameters [7]. Simulation results show that the major effect of increasing diameter is to increase the effective index and decrease the coupling coefficient. The curves almost do not shift in the horizontal direction (along the n_{poly} axis) and the shape of curves is essentially unaffected. Therefore, the effect of cladding diameter on tuning characteristics of LPG is much smaller comparing to ITO thickness and refractive index.

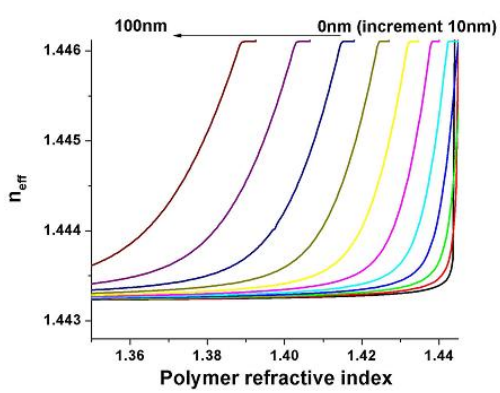

(a) n_{eff}, 1st mode

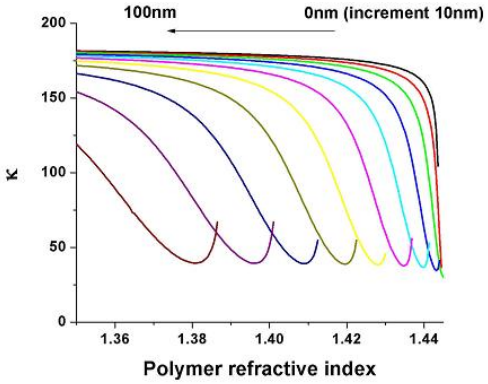

(b) κ, 1st mode

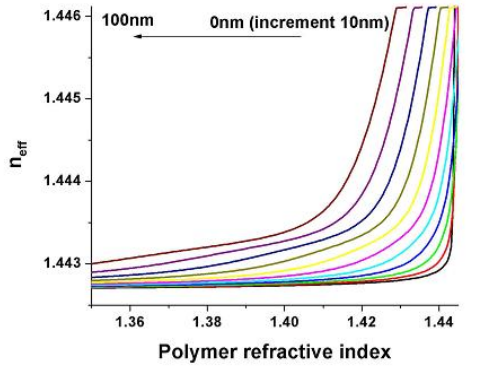

(c) n_{eff}, 2nd mode

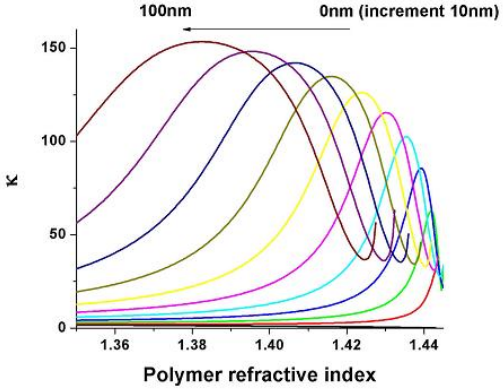

(d) κ, 2nd mode

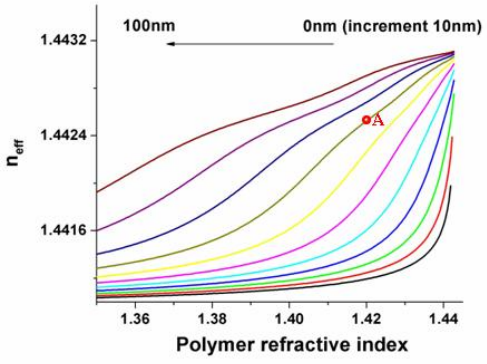

(e) n_{eff}, 3rd mode

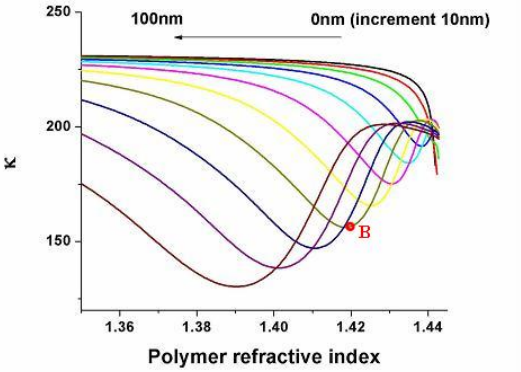

(f) κ, 3rd mode

Figure 3.7. The effect of ITO thickness on the effective refractive index and coupling coefficient for the *1st* to *3rd* cladding modes.

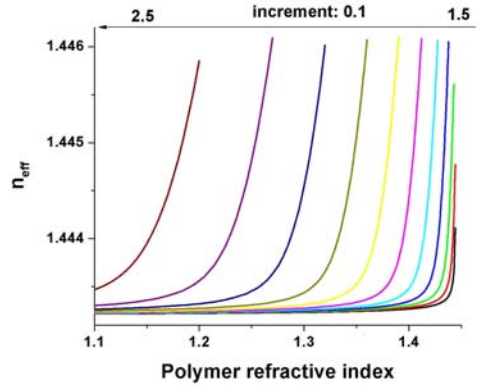

(a) n_{eff}, 1st mode

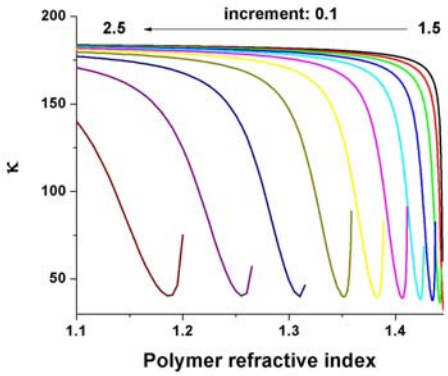

(b) κ, 1st mode

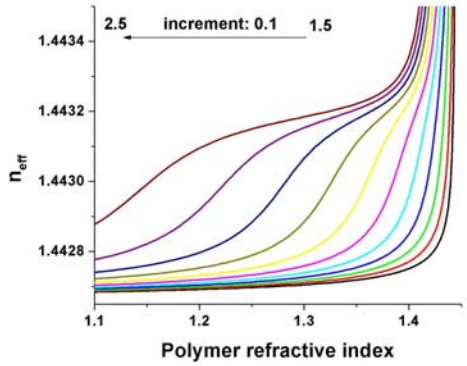

(c) n_{eff}, 2nd mode

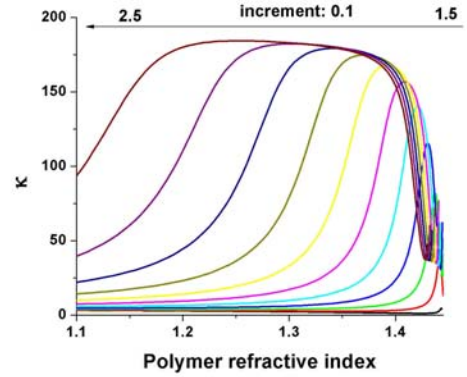

(d) κ, 2nd mode

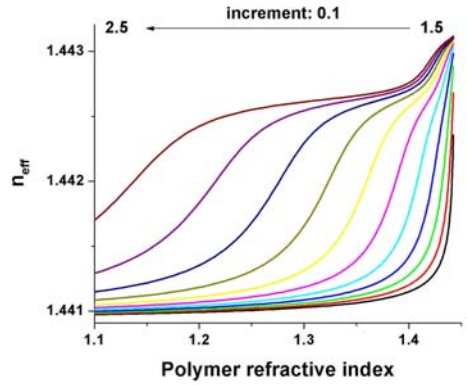

(e) n_{eff}, 3rd mode

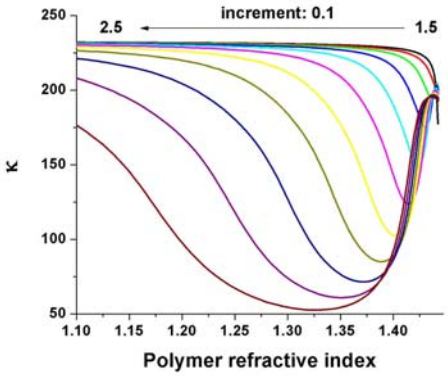

(f) κ, 3rd mode

Figure 3.8. The effect of ITO refractive index on the effective refractive index and coupling coefficient for the *1st* to *3rd* cladding modes.

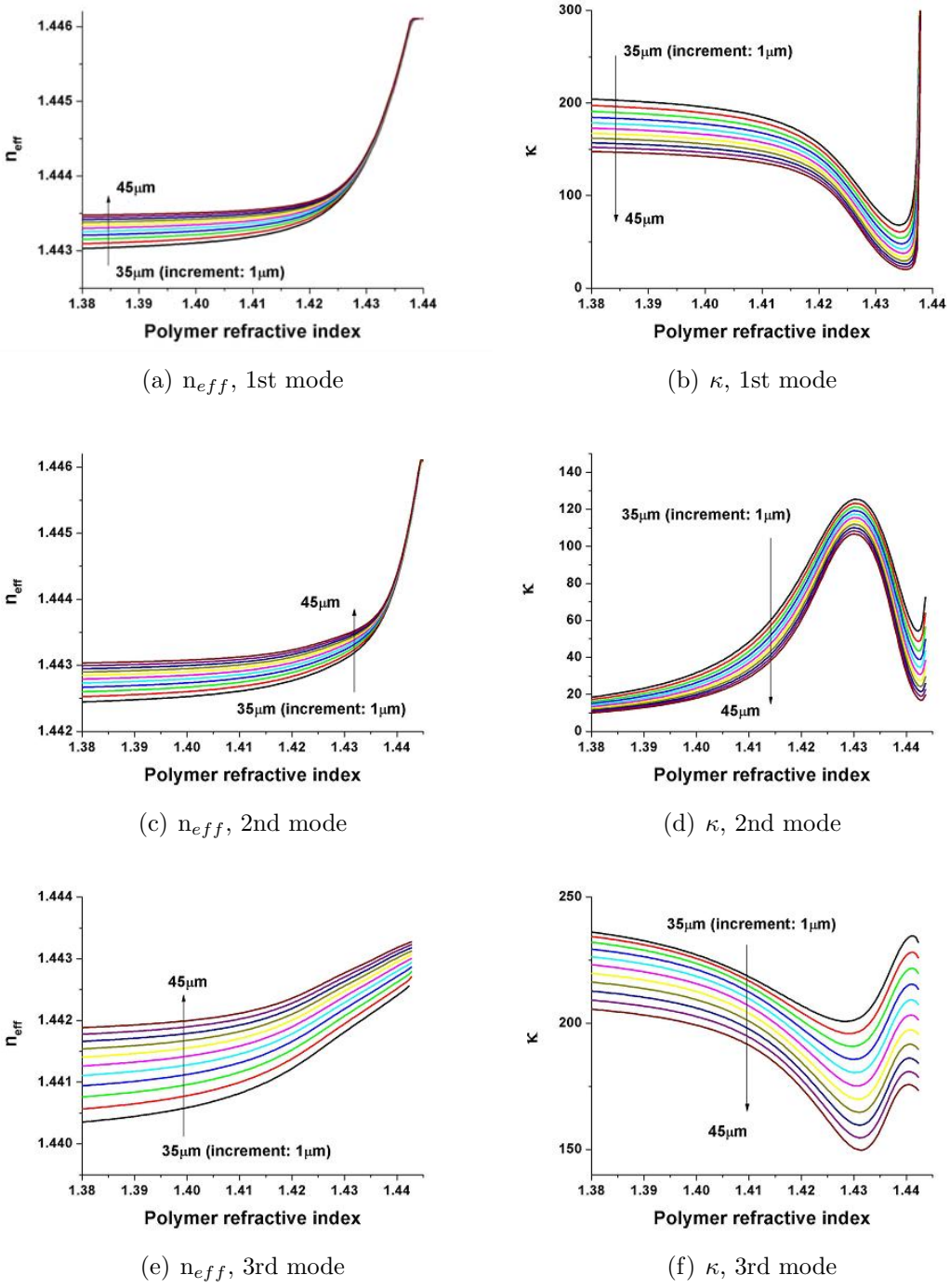

(a) n_{eff}, 1st mode

(b) κ, 1st mode

(c) n_{eff}, 2nd mode

(d) κ, 2nd mode

(e) n_{eff}, 3rd mode

(f) κ, 3rd mode

Figure 3.9. The effect of the diameter of the cladding layer on the effective refractive index and coupling coefficient for the *1st* to *3rd* cladding modes.

3.4 Discussion of simulation result and Conclusions

Discussions of the effect of ITO layer on the enhancement of tuning

In order to understand the origin of ITO effect, it is necessary to take a closer look at the orders of cladding modes in the above simulations. The mode orders are designated according to the effective refractive index of the modes in a descending order (Figure 3.10). In the simulations the mode orders are designated for $n_{poly} = 1$. However, as n_{poly} increases n_{eff} may exceed n_{cl} which means light in the cladding layer is in the form of evanescent wave. These modes are called *ITO modes* hereafter as in this case n_{eff} is smaller than ITO index and is larger than the refractive indexes of cladding and polymer. The orders of ITO modes are counted upwards from n_{cl} and take negative values. Therefore, the original 1st order mode for $n_{poly} = 1$ becomes order -1 when its n_{eff} exceeds n_{cl}, and order 2 becomes order 1, and so on. When n_{poly} further increases so that the originally 2nd mode for $n_{poly} = 1$ becomes ITO mode, the corresponding mode orders of the modes will be -2, -1, 1, $\cdots$. It has been pointed out by several authors that this mode transition behavior is the origin of ITO effect in tunable LPGs [33].

The field intensity distributions of various cladding modes in an LPG are shown in Figure 3.11. The parameters used in the simulation are: ITO thickness 50nm, ITO refractive index 1.8, cladding diameter 40μm. A distinct effect of the ITO is that it attracts light and increases the intensity at the cladding-polymer boundary and in polymer. Using perturbation theory, the variation of the propagation constant of mode due to the change of material refractive index can be expressed

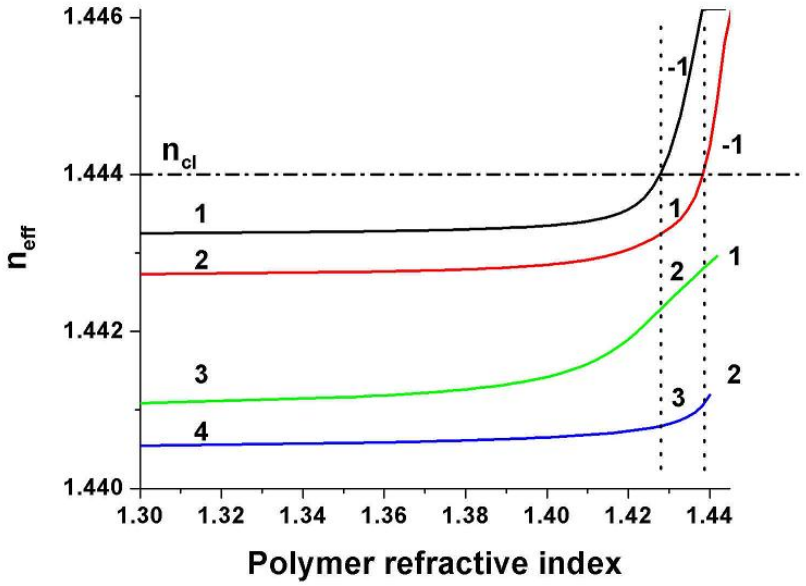

Figure 3.10. The designation of mode orders. The "guided" cladding modes ($n_{eff} < n_{cl}$) have positive orders and the "evanescent" cladding modes ($n_{eff} > n_{cl}$) have negative orders.

as [34]

$$\delta n_{eff}^2 = \frac{\int \delta n^2 |E|^2 dA}{\int |E|^2 dA} \tag{3.113}$$

In the tunable LPG under consideration, $\delta \neq 0$ only in polymer. Therefore, in order to achieve more efficient tuning it is desired that more light energy is contained in the polymer.

The reason why ITO increase light intensity in polymer is that ITO has a refractive index which is higher than both of its adjacent layers (namely, cladding and polymer). Therefore, the cladding-ITO-polymer structure is itself another asymmetric waveguide. Comparing to fibers without ITO layer where there is only one waveguide structure (the core-cladding structure), in this double waveguide structure certain amount of light is attracted by the second waveguide formed

by ITO. When the refractive index of polymer is high enough, light begins to be guided in the second waveguide and becomes the ITO mode. This is evident in Figures 3.11, where for large polymer refractive indexes (e.g. $n_{poly} > 1.426$) there is a peak of intensity distribution at the ITO layer, which is a clear indication of guiding.

It should be noted that although ITO layers forms part of another waveguide structure and the so-called ITO mode is considered here, light energy contained in ITO layer is very small comparing to cladding and polymer layers due to the extremely small thickness of ITO. Furthermore, the ITO mode never contribute to the notch in the transmission spectrum. This is because for ITO modes we always have $n_{eff} > n_{cl} = 1.4441$, which corresponds to resonance wavelength of shorter than 800nm which is far from the wavelength range that we are interested in (roughly 1300nm to 1700nm).

The double waveguide structure that induces redistribution of light energy in the fiber also affects the coupling coefficient. The coupling coefficient is given by equation (3.40):

$$\tau_{01-1\nu}^{co-cl} = \omega\epsilon_0 n_0^2 \sigma\pi \int_0^{r_1} r dr (E_r^{cl} E_r^{co*} + E_\phi^{cl} E_\phi^{co*}) \tag{3.114}$$

Since core mode is independent of polymer refractive index, the variation of coupling coefficient is due to the change of the portion of energy of cladding mode contained in the core. As shown in Figure 3.11c, as the polymer refractive indexes increases the intensity of cladding mode in core first increased and then decreased. Therefore, it reaches an extreme point which corresponds to the turn-point in Figure 3.7. Around the extreme point the variation of coupling coefficient is relatively small since the curve is flat. The existence of both increasing and decreasing por-

tions in the $\kappa - n_{poly}$ curves can be qualitatively understood in the viewpoint of optical resonators. In the cross-section of the fiber, the two waveguide structures mentioned above (the core-cladding and cladding-ITO-polymer structures) can be viewed as two resonators. As the polymer refractive index increases, the phase retardation of light associated with the latter resonator also gradually changes until the resonance condition will be achieved. At this point the Q value of this resonator is maximum and it attracts most energy from the core. This corresponds to the case where κ decreases with increased n_{poly}. When n_{poly} further increases, the resonator leaves its resonance condition and the Q value decreases, and hence it will store less energy and more energy will be "returned" to the core. Therefore, κ increases with n_{poly}. This kind of behavior is not exhibited by LPGs without the high refractive index interlayer because in that case there will be only one resonator (core-cladding) and the competing between resonators cannot be observed.

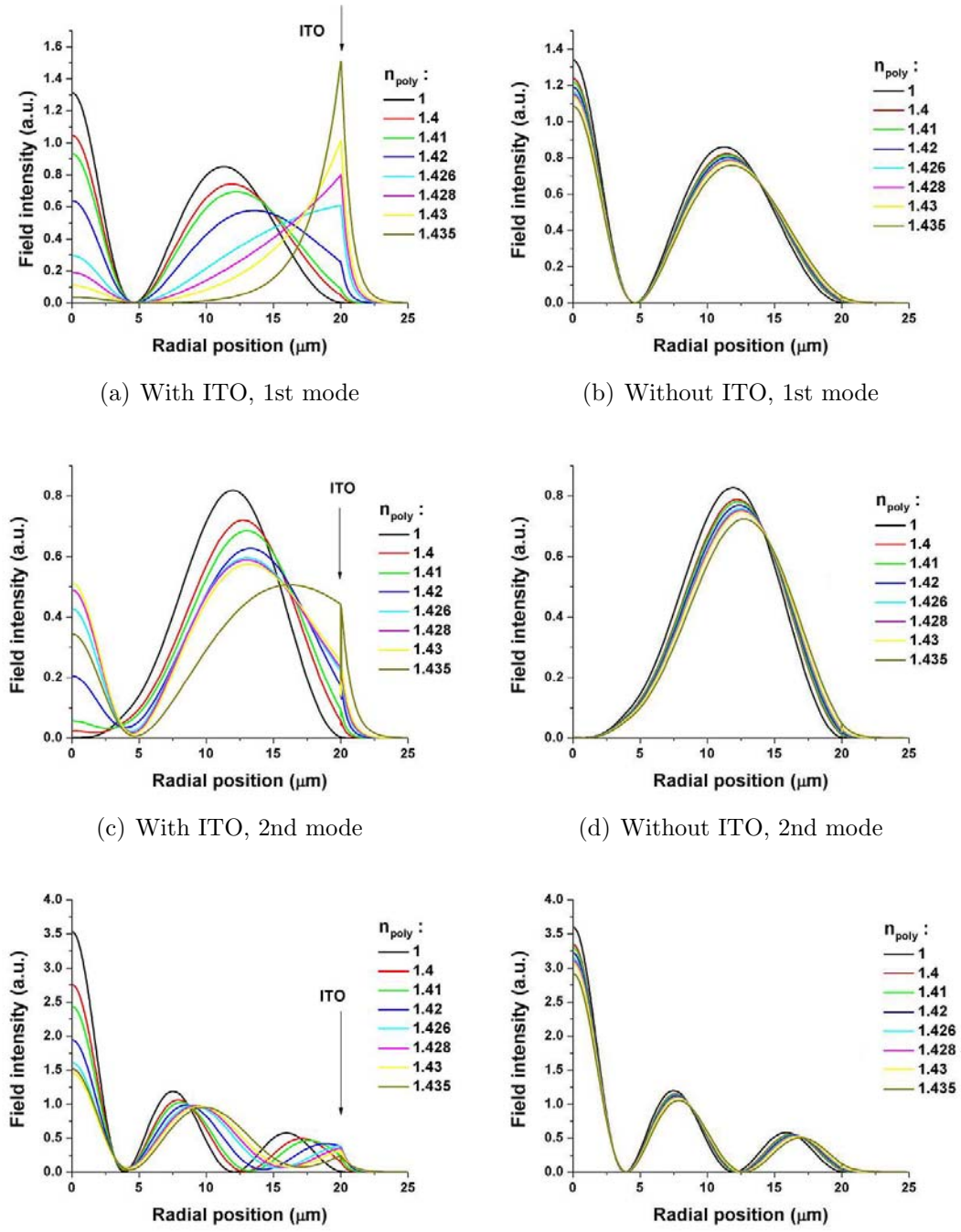

(a) With ITO, 1st mode

(b) Without ITO, 1st mode

(c) With ITO, 2nd mode

(d) Without ITO, 2nd mode

(e) With ITO, 3rd mode

(f) Without ITO, 3rd mode

Figure 3.11. Radial distribution of field intensity of the *1st* to *3rd* cladding modes in an LPG.

Conclusions on the simulation of tunable LPG

The simulation results show that ITO layer effectively enhances the tuning range of the tunable LPG while maintaining a small variation of notch depth. It is also demonstrated theoretically that with the achievable refractive index change in the terpolymer the desired tuning range of 40nm can be achieved. The simulation suggests that first of all, the combination of ITO refractive index and thickness and cladding diameter should be such that the native refractive index of the terpolymer corresponds to the n_{poly} that shows large tuning range and small variation of notch depth around the desired resonance wavelength (around 1550nm). Furthermore, the modulation depth of the grating should result in deep notch at the resonance wavelength. The best condition will be determined by trial-and-error in experiments with the simulated curves as a guide.

Chapter 4

EXPERIMENTAL REALIZATION OF THE TUNABLE LONG-PERIOD FIBER GRATING

4.1 Introduction

In order to experimentally realize the E-O tunable LPG with more than 40nm of tuning range which is predicted to be possible by simulation, a fabrication process must be developed. Furthermore, in the simulation we have seen that the n_{eff} vs. n_{poly} and κ vs. n_{poly} curves are very important for the design of tunable grating. Therefore, these relationships should be also measured experimentally to help determine the best parameters for the LPG. This chapter is organized as follow. The complete fabrication process of the tunable LPG will be first presented. After that, the transmission spectrum of bare LPGs (without polymer coating) immersed in different index matching fluids will be presented, which provide experimental data of the variation of resonance wavelength and notch depth with polymer refractive

index. In this experiment, it has been found that in order to achieve the desired tuning range the native refractive index of the terpolymer must be increased by at least 0.02. Therefore, the third section will be devoted to the development of a nanocomposite of the terpolymer which exhibit large E-O effect and adjustable native refractive index will be discussed. Finally, the experimental realization of E-O tunable LPG with about 50nm of tuning range will be demonstrated.

4.2 Fabrication process for the tunable long-period grating

The general fabrication process involves several steps:

1. Fiber etching
2. Writing gratings
3. ITO deposition
4. Polymer coating
5. Metal deposition
6. Wiring

The photosensitive fiber

In order to fabricate fiber gratings, it is necessary to induce periodic refractive index change in the fiber. There are several different methods to induce refractive index change in the fiber. One method is to use UV irradiation on photosensitive fibers which refractive index can be changed by exposure to UV irradiations. The photosensitivity can be induced by doping of impurities or hydrogen loading [35,

36]. Another method is to utilize thermal effects generated by CO_2 laser or electric arcs on fibers [37].

UV irradiation of doped photosensitive fiber has been used as the grating fabrication method in this study. The fiber is F-SBG-15 single mode photosensitive fiber (purchased from Newport). The core of this fiber is doped with Ge and B. Ge doping in silica fiber increases the refractive index of the fiber and also induces photosensitivity. The Ge defects in silica usually have a Ge atom coordinated with another Ge or Si atom. This bond is responsible for the absorption peak at around 240nm wavelength. Upon UV irradiation, this bond readily breaks and it is believed that this causes reconfiguration of the shape of the molecule, change in the density of material, and also the absorption. These effects causes the refractive index change [35]. On the other hand, boron doping reduces the refractive index of the fiber. Therefore, co-doping of germanium and boron allows for high germanium content with overall refractive index that is similar to normal single mode fibers. The maximum increase of refractive index in the B-Ge co-doped fiber can be close to 10^{-3}. Some characteristics of the F-SBG-15 fiber is summarized in Table 4.1. It is noteworthy that the refractive index profile in the B-Ge co-doped core isn't an ideal uniform distribution but is as shown in Figure 4.1

Operating wavelength (nm)	1550
Index profile	Step
Core index	1.4491 (@1550nm)
Cladding index	1.4441 (@1550nm)
NA	0.12-0.14
Core diameter (μm)	8.3
Cladding diameter (μm)	125$\pm$1
Background loss (dB/km)	$\leq$100
Cut-off wavelength (nm)	1100-1260

Table 4.1. The properties of the F-SBG-15 photosensitive fiber

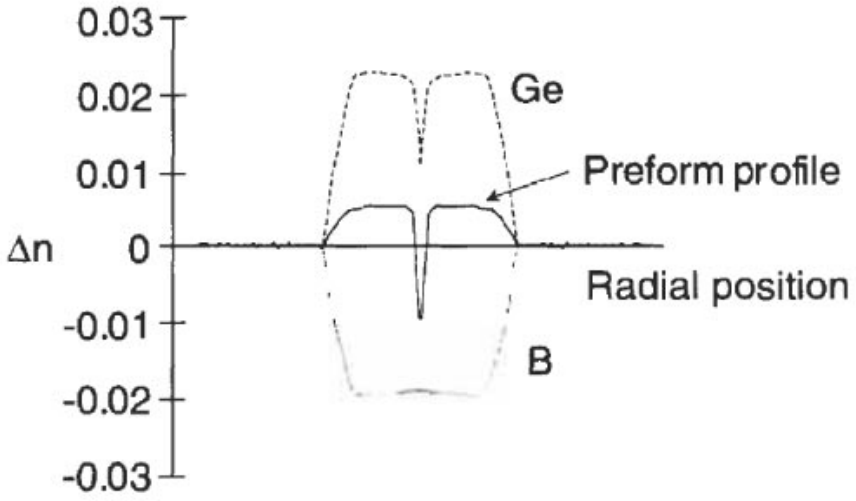

Figure 4.1. The typical refractive index profile in the core of B-Ge co-doped photosensitive fiber. Adapted from [35].

Fiber etching

The first step in the fabrication of the tunable LPG is to reduce the cladding diameter from its original value of 125μm down to about 40μm. The purpose of reducing the cladding diameter is to increase the sensitivity of the cladding mode parameters to the refractive index of the polymer second cladding [7]. The reduction of cladding diameter is realized by etching in hydrogen fluoric acid (HF). Before etching the plastic jacket (which is made of acrylic for the F-SBG-15 fiber) is first stripped using a fiber stripper. In case the jacket is difficult to strip, such as for short segment of fiber, the jacket can be first immersed in acetone or concentrated sulfuric acid for several minutes and then the stripping will be very straightforward. The etching solution is prepared by mixing hydrogen fluoric acid (assay 50%, from JTBaker) and D.I. water with mixing ratio of 1:1 or 1:2. It takes approximately 80min to 120min to etch the fiber down to 40μm, depending on the concentation of the HF solution. In order to precisely control the diameter, the fiber is taken out several times during the etching to perform diameter measurements. The diameter

is measured using an optical microscope.

Grating writing

After etching, long-period grating is written in the fiber using UV irradiation. The fiber is fixed on a stage and an amplitude mask is positioned in front of the fiber. The mask is made of chromium and the typical period is between 200μm and 500μm. The UV irradiation is produced by a frequency doubled argon laser at 244nm. A mirror attached to a computer controlled translation stage is used to scan the laser beam over the mask. During the writing process, the transmission of the fiber is real-time monitored using an optical spectrum analyzer (OSA).

ITO deposition

In order to apply electric field to the polymer second cladding, electrodes are required at the inner and outer sides of the polymer layer. The requirements on the inner electrode is especially strict because it affects the optical properties of the fiber. First of all, it should be at least partly transparent so that the polymer is not screened. Secondly, as indicated in the numerical simulation, a high refractive index dielectric layer is essential for the tuning of LPG. Indium-tin oxide (ITO) has been chosen as the inner electrode material for the tunable LPG.

A detailed review of ITO is provided in [38]. It has been pointed out that the simultaneous occurrence of high optical transparency (90%) and electronic conductivity require the creation of electron degeneracy in wide-gap oxides ($\geq$3eV) by suitably introducing nonstoichiometry and/or appropriate dopants. Perfect stoichiometric oxides are either insulators or ionic conductors which is not interesting for electronic applications due to the high activation energy required for ionic con-

duction. The intrinsic bandgap of indium oxide (In_2O_3) is about 3.5eV. In practice, the deposited films lack stoichiometry due to oxygen vacancies. At high vacancy concentrations, an impurity band is formd and is overlapped with the conduction band which produces a degenerate semiconductor. Tin has a valence number of 4 and hence when doped into indium oxide it act as an electron donor and increases the carrier concentration. The carrier concentration in ITO can reach $10^{21}cm^{-3}$, and at such concentration the carrier mobility is about $10cm^2/Vs$. The mobility is affected by the morphology of ITO films. For ITO films deposited on silica which is an amorphous material, it is expected that the conductivity is lower than that deposited on single crystal substrates.

ITO can be deposited using a wide range of techniques such as vacuum evaporation, dc and rf sputtering, spray pyrolysis, chemical vapor deposition, and sol-gel reactions [38]. In this study the ITO layer is deposited using rf magnetron sputtering of oxide targets (Anatech Hummer XII sputtering system) because of the easy control of deposition parameters and the moderate cost of deposition equipment. The properties of ITO films depend on the deposition method in a complicated manner. The effect of sputtering condition on ITO properties has been investigated thoroughly in [32]. In our experiments, the sputtering has been performed at room temperature using pure argon gas. The deposition pressure and power were 5mTorr and 10W. Fiber is typically taped to a frame, and after sputtering for one side the frame is flipped over and sputtering is performed for the other side using exactly the same conditions. This certainly does not produce a uniform cylindrical coating of ITO on the fiber. However, it is observed in experiments that this type of ITO coating is sufficient for the tunable LPG. During the deposition of ITO on fibers, a silicon wafer substrate was coated in the same chamber for refractive index and thickness measurements. The refractive index was measured

by an ellipsometer (Rudolph AutoEL II) equipped with a He-Ne laser (633nm), and the thickness was measured using both the ellipsometer and a profilometer (Tencor Alpha-step 500). Under such deposition conditions, the refractive index of ITO on Si substrate was 1.88 and the deposition rate was 1.1nm/min. The resistivity of ITO on fiber is about $10^{-2}\Omega$cm. Comparing to the common reported resistivity of $10^{-4}\Omega$cm this value is significantly higher. This is perhaps mainly due to the small thickness of ITO. It has been reported that when ITO thickness is smaller than 50nm, the resistivity increases significantly because of the formation of non-continuous films as in the case of metal films [38].

Polymer deposition

The polymer layer need to be thicker than the penetration depth of light. For instance, referring to Figure 3.11 it is seen that the field intensity decays to nearly zero at 5μm from the polymer-ITO boundary. Therefore, the polymer thickness in the tunable LPG under investigation is at least 10μ to prevent leakage of light. However, the polymer layer also cannot be too thick as otherwise the required voltage will be too high. Therefore, the polymer coating process should produce high quality polymer films with the thickness of around 10μm on fibers with typical diameter of 40μm.

Considering the cylindrical geometry of fiber and the requirement of conformal coatings, the most suitable coating method is dip-coating (Figure 4.2), in which the fiber is first immersed into a solution and then drawn out at a controlled speed. Due to capillary forces a thin layer of solution will remain on the surface of the fiber. After evaporation of solvent this layer will solidify and form a uniform polymer coating on the fiber. The thickness of the liquid film on a planar substrate

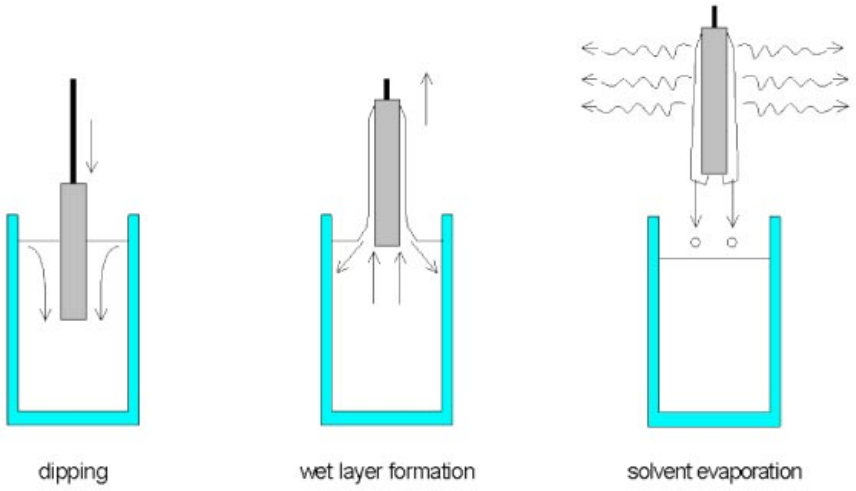

Figure 4.2. The process of dip-coating. Addapted from [40].

drawn from solution is predicted by the Landau-Levich formula,

$$\bar{h}_\infty = 0.945 l_c Ca^{2/3} \tag{4.1}$$

with

$$l_c = \sqrt{\frac{\sigma}{\rho g}}, \quad Ca = \frac{\mu U}{\sigma}$$

where ρ, μ, and σ are the density, viscosity, and surface tension of the fluid, U is the drawing speed, and g is the gravitation field. Therefore, theoretically the thickness of coating is controlled by the concentration of solution and drawing speed.

Although dip-coating can readily coat high quality thin film on flat substrates, there are some concerns with applying it on fibers. A fiber has a cylindrical surface and the radius of curvature is very small, which results in two problems. The first is that it is difficult to obtain a thick coating. For instance, using the same drawing speed, several microns thick films can be coated on planar substrates or glass sticks with large diameters (e.g. 5mm) while only nanometer sized film can be obtained

on a fiber with 40μm diameter. This is because it is difficult for the small capillary force provided by the fiber surface to balance the large gravity force acting on the solution. Another problem is the instability of solution flow. Consider a fiber with diameter of 40μm and a required coating thickness of 10μm, if 20% solution is used, it can be estimated that right after drawn out of the solution, the diameter of the fiber together with the solution on fiber surface will be 140μm. This means the solution drawn together with fiber is essentially a stream of liquid rather than a thin layer of liquid on substrate. It is well known that a long vertical column of liquid may break into beads due to the Rayleigh instability, which is a result of the surface tension of liquid. Indeed, the formation of beads has been observed in our experiment.

In order to overcome these problems, the conventional dip-coating process shown in Figure 4.2 has been modified as shown in Figure 4.3. In the modified setup, the solution is contained in a small die with a large opening on the top and a small opening at the bottom (Figure 4.3). The fiber is directed through the die and is drawn downwards. Therefore, gravity is now in the same direction of drawing and much thicker films can be readily obtained with low drawing speed. The low drawing speed allows for the solvent to evaporate sufficiently, and the evaporation speed can be increased by the heating elements. Therefore, the solution can solidify quickly enough to prevent the onset of Rayleigh instability. This also prevents the solution from flowing along the fiber which results in thickness gradient.

The selection of solvent is critical in dip coating. The boiling points of some common solvents for P(VDF-TrFE-CFE) terpolymer is shown in Table Ch3-table: solvents. Solvents with low boiling points and high vapor pressures have high evaporation rates. As discussed above, high evaporation rate is required to ensure

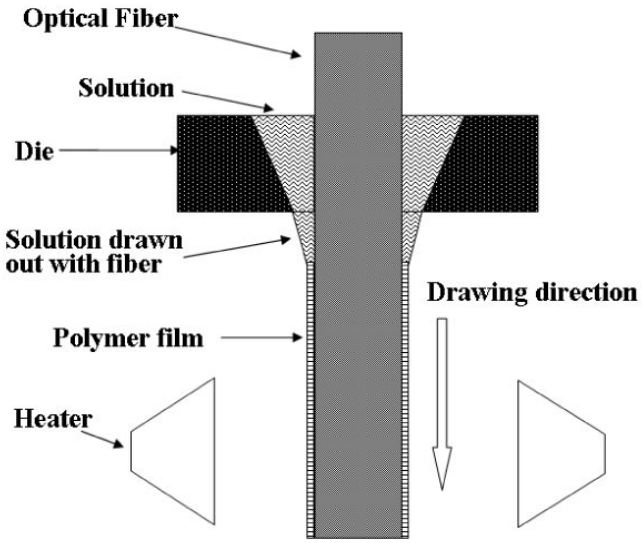

Figure 4.3. A modified process of dip-coating. [41]

Solvent	Boiling point (˚C)	Vapor pressure (mmHg)	Viscosity (mPa s)	Surface tension (mN/m)
DMF	153	2.7	0.802	36.4
DMSO	189	0.42	1.991	43.0
NMP	202	0.5	1.666	40.7
MEK	80	78	0.378	23.7
Acetone	56.5	400	0.303	22.7
1,4-dioxane	74	27	1.194	32.8
cyclohexanone	156	5	2	35.0

Table 4.2. Properties of some solvents for P(VDF-TrFE-CFE) terpolymer. DMF: N,N-dimethylformamide; MEK: methyl ethyl ketone. Values are for 1 atm pressure and 25˚C. [39]

quick solidification. However, a too high evaporation rate often results in the formation of a polymer layer on the surface of coating solution. Therefore, methyl ethyl ketone (MEK) has been selected as the solvent due to its moderately high evaporation rate.

The concentration of P(VDF-TrFE-CFE)/MEK solution used in dip-coating for the tunable LPG is 15% (polymer wt./solvent vol.). The resulting solution has a very high viscosity. The fiber is drawn with an Instron machine and the typical

drawing speed is 1mm/sec. This produces film thickness of around 10μm.

Metal deposition and wiring

The outer electrode merely provides electrical conductivity and its optical properties do not affect the performance of the tunable LPG. Sputtered gold or silver (using EMITech K550X Sputter Coater) are typically used as outer electrodes since they are among the easiest to be deposited and have very high conductivity. The metal should cover the segment of fiber with the grating written in. Small part of the polymer on fiber is then removed by acetone to expose the inner ITO electrode. Metal wires are then connected to the electrodes using silver epoxy (VonRoll Isola, E-Solder 3021A).

The microscopic images of etched fiber and polymer coated fiber and photographic picture of finally finished device are shown in Figure 4.4.

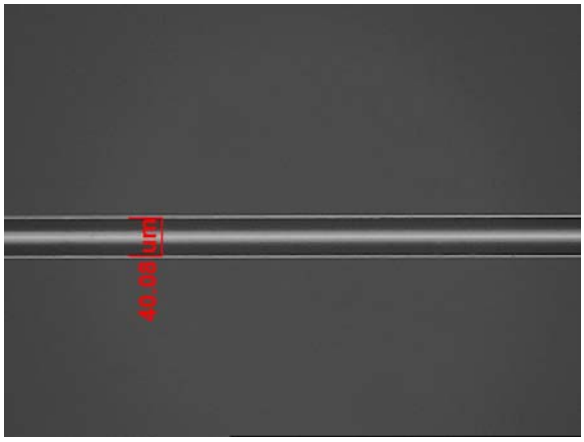

(a) Ethed fiber

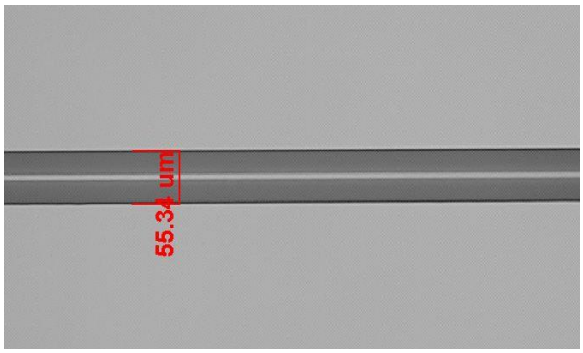

(b) Fiber coated with 10μm of polymer

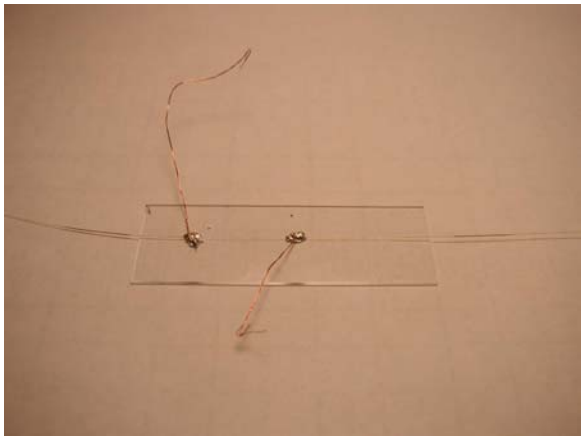

(c) Finished device

Figure 4.4. The microscopic images of etched fiber and polymer coated fiber and photographic picture of finally finished device

4.3 Experiments with index matching fluid

The numerical simulation of the LPG reveals that it is possible to achieve the desired 40nm tuning using E-O effect in P(VDF-TrFE-CFE) terpolymer if the terpolymer refractive index lies in certain range. However, it is expected that the numerical simulation cannot be directly used to predict the device parameters due to the uncertainties of material parameters used in the calculation, such as material dispersion, refractive index profile of the fiber, etc. Therefore, the optimum conditions for the tunable LPG that result in the widest tuning range need to be determined by experiments. For this purpose, we have performed the index matching fluid test.

In order to measure the transmission spectrum of the LPG for different values of the refractive index in second cladding, LPGs (with or without ITO coating) without polymer coatings were immersed into different liquids with precisely known refractive indexes. In this so-called index matching fluid test, the refractive index of the second cladding under which the LPG has the largest tunability can be determined.

The index matching fluids used in this experiment were purchased from commercial source(Cargille, Refractive Index Fluids). The LPG to be tested was laid on a microscope slide and was monitored by an optical spectrum analyzer. The transmission spectrum in air was first recorded, and then different index matching fluids were applied to cover the LPG and the spectrum was recorded. After testing with each refractive index the LPG was wiped and rinsed several times with alcohol and acetone to ensure the air spectrum is recovered before continuing to the next fluid.

The transmission spectrum of bare LPGs without ITO coatings is shown in

Figures 4.5a and 4.6a. As the refractive index of fluid increases, the resonance wavelength gradually shifts to shorter wavelengths. The wavelengths shifts faster when the refractive index approaches that of the fiber cladding (1.444 @1550nm) (Figure 4.8. Using Δn=0.01 as an estimation of the E-O effect in the terpolymer, it is evident from Figure 4.8 that the largest possible tuning range is 30nm. On the other hand, as the refractive index increases the rejection level (i.e. depth of the notch) decreases and finally approaches zero when the refractive index is close to cladding index. Comparing Figures 4.5a and 4.6a, it can be found that reducing the fiber diameter shifts the spectrum to longer wavelength and slightly increases the tunability. All the above observations for LPGs without ITO coating are consistent with the simulation result as well as other published results [7]. It is also noticed that at very high fluid refractive indexes such as 1.71 and 1.8 the notches can be observed again. These notches are due to the coupling between core mode and the leaky cladding modes [42]. When the refractive index of the fluid exceeds that of the cladding, total reflection can no longer at the cladding boundary. However, when the fluid index is high enough the reflection at the cladding-fluid boundary is high enough to support a leaky mode over certain distance. The resonance wavelength of leaky mode induced notches can merely be tuned since in this case changing the refractive index of the fluid can only change the amplitude of the reflected light and not the phase.

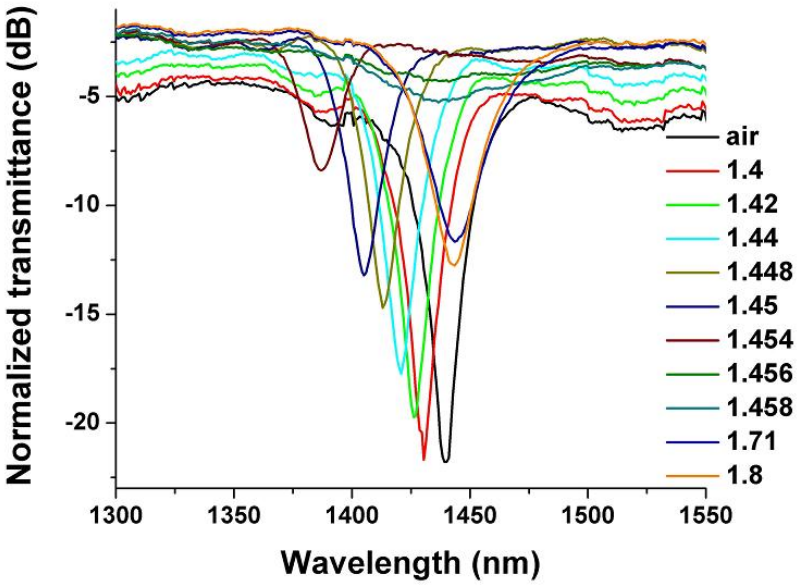

(a) Without ITO

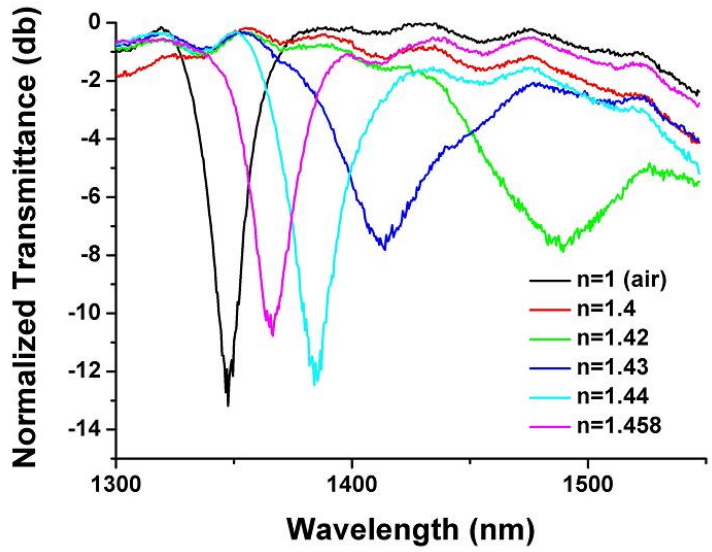

(b) With ITO

Figure 4.5. The transmission spectrum of LPGs with and without ITO coating immersed in different index matching fluids. Fiber diameter: 35μm; Grating period: 400μm; Grating length: 8mm. ITO thickness: 50nm; ITO refractive index (@1550nm): 1.8. The refractive indexes of the fluids are for 589nm wavelength.

The transmission spectrum of ITO coated LPG is shown in Figures 4.5b and 4.6b. It is obvious that ITO significantly changed the tuning characteristics of the LPGs. For low fluid refractive indexes, the response of ITO coated LPG is similar to that of the uncoated LPG and the resonance wavelength shifts to shorter wavelength. However, the notch depth decreases to zero much earlier at the fluid refractive indexes. The exact value of this "transition index" at which the notch disappears depends on the fiber and ITO parameters (e.g. 1.4 in Figure 4.5b and 1.43 in Figure 4.6b.) When the refractive index of the fluid further increases, another notch appears at the long wavelength side of the measurement wavelength window and shifts to shorter wavelength. This notch is shallow and shifts very fast when the fluid index is only slightly higher than the transition index. As the fluid index increases further, the notch becomes deeper and the resonance wavelength approaches that of the same LPG in air. The highest tunability can reach 76nm per 0.01 change in fluid index, which is sufficient to realize the desired 40nm tuning range with achievable E-O effect in the terpolymer.

For a notch induced by the coupling to a specific cladding mode, the resonance wavelength decreases with increasing fluid index because the effective index of the cladding mode will increase. By comparing to the simulation results it can be determined that the notch for ITO coated LPG in air is associated with the first cladding mode(Figures 3.7 and 3.8). At high fluid indexes this notch shifts to very short wavelength and its depth quickly decreases to nearly zero, and hence cannot be observed in the measured spectrum. On the other hand, considering the effective refractive index of the third cladding mode (Figures 3.7 and 3.8) it is believed that the new notch appearing at the long wavelength end of the measurement window is due to the third cladding mode. This means the tunability is highest when the mode transitioning happens, which is also consistent with the simulation result.

Comparing Figures 4.5b and 4.6b, it is evident that for different fibers the mode transitioning happens at different fluid indexes. However, it is not clear whether such difference really results from the diameter difference or is due to the variation of ITO parameters. As shown by simulation results, reducing the diameter of fiber decreases the effective index of the cladding mode. Therefore, the resonance wavelength should shift to longer wavelength and the mode transition should happen at higher fluid indexes (Figure 3.9). However, in the index matching fluid test it was observed that for smaller fiber diameters the mode transition happened at lower fluid indexes. On the other hand, as shown in Figures 3.7-3.8 a small change in ITO refractive index or thickness will result in a significant change of resonance wavelength. Therefore, the experimentally observed difference between different fibers may be due to the dependence of ITO coverage on fiber diameter or even the batch-to-batch variation of the parameters of sputtered ITO.

It was also found that it was difficult to reduce the mode transition index down to the terpolymer refractive index (n=1.4) while achieving both high tunability and acceptable notch depth. The lowest achieved index was approximately 1.42 (Figure 4.5). According to simulation, this refractive index can be lowered by increasing ITO thickness. However, in the experiment it was found that for thick ITO deep notch and wide tuning could not be achieved simultaneously. Perhaps this is due to the increased total optical loss in thicker ITO films which causes the notch to become shallower.

The feasibility of using metal instead of ITO as the inner electrode has also been studied (Figure 4.7). The refractive index of silver at 1550nm is $n = 0.469 + 9.32i$. It is evident in Figure 4.7 that the LPG coated with silver exhibited similar response to those coated with ITO. More specifically, the mode transitioning also happened and there is a range of fluid index where the tunability is relatively large.

For silver which is a metal, we expect that the transition of mode is also because that the metal layer can itself guide light. However, in this case the mode is surface plasmon like. In this study, metal coated LPGs were not extensively studied and more detail about this kind of fiber gratings can be found in [43]. However, the preliminary experiment result presented here indicates the potential of using metal as inner electrodes in E-O tunable LPGs.

The conclusions drawn from the index matching test can be summarized as follow.

1. Using the mode transition phenomenon in ITO coated LPG, it is possible to realize the desired tuning range (40nm) with the achievable E-O effect in the terpolymer (>0.01).

2. The desired tuning range can only be achieved when the refractive index of polymer is close to an "optimum index".

3. The lowest experimentally achieved "optimum index" is around 1.42.

4. Preliminary results indicate that it is feasible to use metal instead of ITO as inner electrode for tunable LPGs.

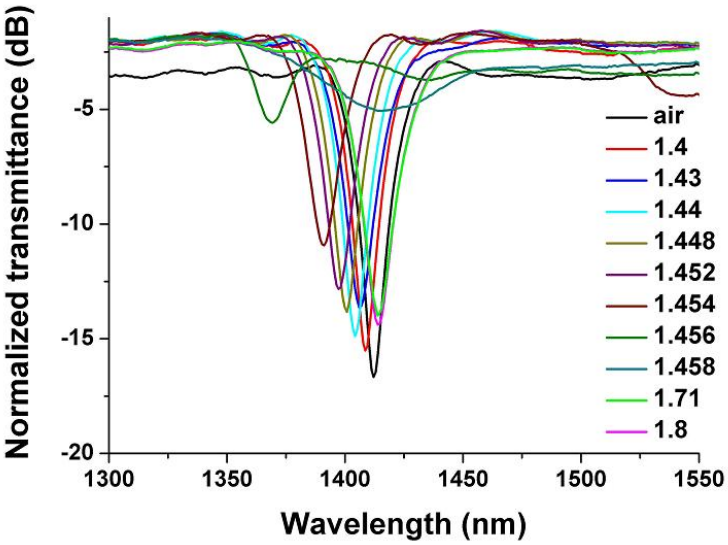

(a) Without ITO

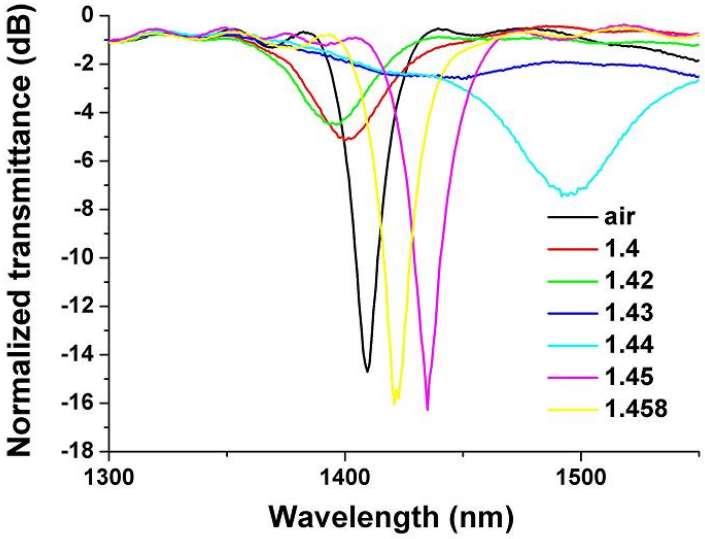

(b) With ITO

Figure 4.6. The transmission spectrum of LPG with and without ITO layer immersed in different index matching fluids. Fiber diameter: 40μm.

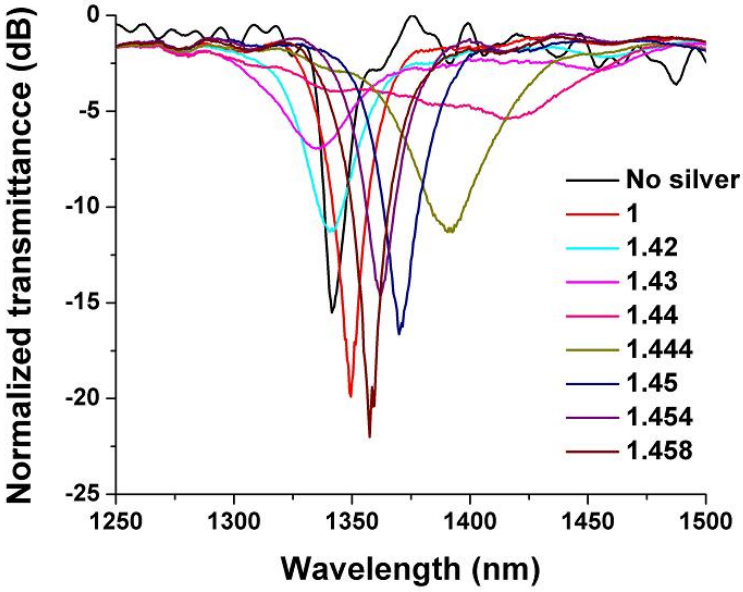

Figure 4.7. The transmission spectrum of LPG with silver coating immersed in different index matching fluids. Fiber diameter: 37μm.

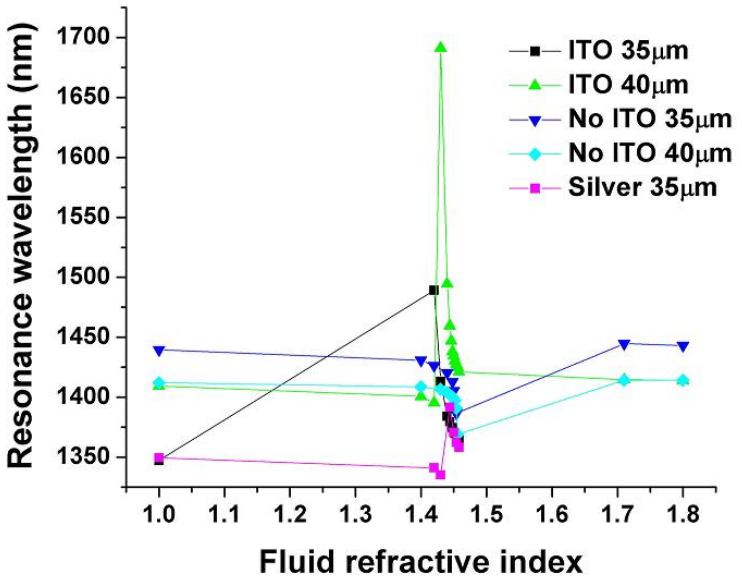

(a)

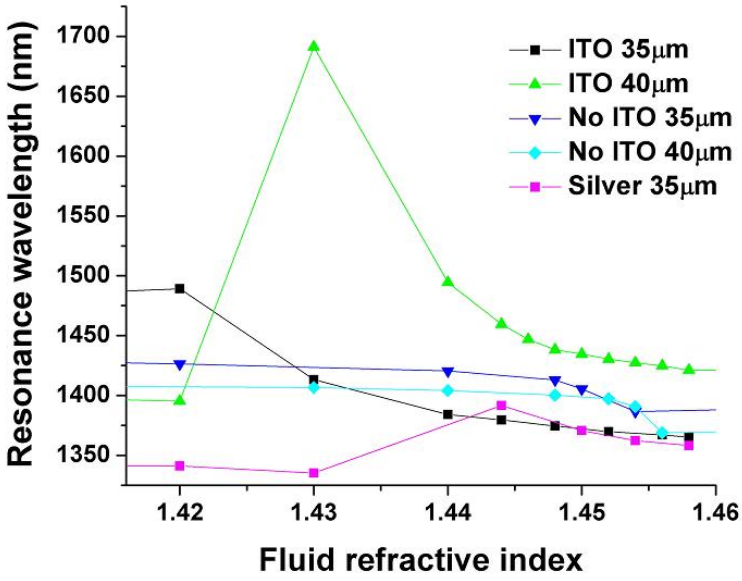

(b)

Figure 4.8. The tuning characteristic of LPGs obtained from Figures 4.5-4.7. (b) shows the detail of (a) in a narrower refractive index range.

4.4 Zinc sulfide - P(VDF-TrFE-CFE) nanocomposite with large E-O effect and adjustable native refractive index

Introduction

The P(VDF-TrFE-CFE) terpolymer exhibits a very large electro-optic (E-O) effect that is many times higher than most conventional E-O materials. However, in order to achieve wide tuning range in an LPG the native refractive index of the terpolymer must be close to an optimum index. For instance, index matching fluid test revealed that this optimum index is approximately 1.42, while the native refractive index of the P(VDF-TrFE-CFE) terpolymer is only 1.4. Therefore, the terpolymer needs to be modified and the modified material must satisfy the following requirements:

1. The refractive index must be increased by at least 0.02.

2. Large E-O effect must be maintained.

3. The optical loss must be almost the same as the terpolymer.

The basic idea to increase the refractive index of the terpolymer is to introduce another component with high refractive index. The refractive index of the resulting heterogeneous material is estimated by effective medium theory:

$$\frac{n^2-1}{n^2+2} = f_a \frac{n_a^2-1}{n_a^2+2} + f_b \frac{n_b^2-1}{n_b^2+2} \tag{4.2}$$

where f_a, f_b, n_a and n_b are the volume fractions and refractive indexes of the two components and n is the refractive index of composite. In order to maintain large

material	wavelength (nm)	n	wavelength	n
CdTe	625	2.873	1550	2.7384
GaAs	632.6	3.856	1550	3.3737
GaP	630	3.3132	1600	3.0509
Ge	635.8	5.5	1550	4.275
InAs	632.6	3.962		
InSb	632.6	4.249	1550	4.08
InP	639.1	3.530	1549	3.167
PbSe	619.9	3.65		
PbS	619.9	4.29	1500	4.25
PbTe	1240	4.55		
Si	632.6	3.882	1532	3.4784
SiC	619.9	2.634	1248	2.573
ZnS	635.8	2.352	1550	2.2706

Table 4.3. Refractive indices of semiconductors at near-IR wavelengths [31].

E-O effect, the volume percentage of the high refractive index component should be minimized. Blending with other polymers is not applicable here because polymers cannot achieve high refractive indexes (typically lower than 1.7) [45]. Similarly, chemical modifications such as copolymerization and grafting are also not preferred due to the low molar refractions of organic groups [46]. Therefore, perhaps the most feasible approach is to develop nanocomposites with high refractive index inorganic nanoparticles embedded in terpolymer matrix. Refractive indexes of higher than 2 are readily available in many inorganic materials and with such refractive indexes only several volume percents of the high index material is required to achieve n=1.42. A list of common high refractive index materials is provided in Table 4.3.

While the first two requirements can be satisfied by proper material selection, the requirement for low scattering is the most challenging in the preparation of nanocomposites. The scattering loss of light is small only if the particle size is much smaller than light wavelength, and in this case the scattering cross-section σ_s of a single particle is proportional to a^6/λ^4 where a is the diameter of particle

and λ is the wavelength. Therefore, a small increase in particle size will induce a large increase of scattering loss. Therefore, it is important to keep the particle size much smaller than light wavelength.

Nanoparticles with sizes of several nanometers to tens of nanometers can be easily synthesized. However, the nanoparticles have extremely large surface areas and hence large agglomerations are often formed to minimize the total surface energy. This could result in particle size on the order of microns and induces very large scattering loss. Two categories of methods can be used to avoid agglomeration. The first are physical methods such as ultrasound treatment and ball milling that mechanically break the agglomerations into small particles. The second are chemical methods which mainly involves modification of the surface of particles. Both of these methods have been investigated in this study.

Synthesize of nanocomposite

The easiest method to disperse nanoparticles is to use ultrasound treatment. Here titanium oxide (TiO_2) have been chosen as the inorganic filler due to its high refractive index (n=2.2) and the wide availability of TiO_2 nanoparticles. The nanoparticles were in the form of dry powders and the powders were added into terpolymer solution in MEK or DMF and the mixture was treated using a ultrasound probe. The power provided by the ultrasound probe was 15W. It was found that ultrasound treatment could not produce good dispersion and precipitation were observed soon after the ultrasound was turned off.

From a fundamental point of view, it is the surface and interfacial energies of the two phases that determine whether a good dispersion of nanoparticles in polymer matrix can be achieved. If the interaction between the two phases is weak

it is expected that large agglomeration will form to minimize the surface area of the nanoparticles. On the other hand, if there is strong interaction between the two phases, the interface area between the two material will be maximized and hence good dispersion can be achieved. It is well known that fluoropolymers show poor adhesion to most substances and hence it is expected that the problem of agglomeration will be serious. This is perhaps the reason for the poor result of ultrasound assisted dispersion. Therefore, chemical method is preferred to prepare the nanocomposite and indeed, most of the previously reported nanocomposites of the terpolymer involve modification of the surface of the particles that promotes the interaction between the polymer matrix and the nanoparticles [47, 48].

There are two requirements for the chemical synthesis route of the nanocomposite. First of all, the solvent used in the synthesis must be able to dissolve the terpolymer. Secondly, proper coupling agents must be found to modify the surface of the nanoparticles and enhance the particle-polymer interaction. Recently, the development of a high refractive index nanocomposite based on zinc sulfide (ZnS) and polythiourethane (PTU) has been reported [49, 50]. Zinc sulfide has a high refractive index (n=2.27 @ 1550nm) and is transparent from 400nm to 20μm [31]. Furthermore, the solvent used in the synthesis (DMF) is a good solvent for the terpolymer. However, the particle-polymer interaction in the ZnS-PTU nanocomposite is provided by the copolymerization of the coupling agent and the polymer matrix, which is not available in the terpolymer. In this study, we have investigated the preparation of ZnS-terpolymer nanocomposite with thiophenol (PhSH) and methyl 3-mercaptopropionate (MMP) as the coupling agents (Figure 4.9. The thiol groups in these molecules bond to zinc sulfide particles. It is expected that the aromatic ring in PhSH will minimize the surface energy of the particles and the carbonyl group in MMP will form hydrogen bonds with the terpolymer as in

the case of PVDF-PMMA blends [51].

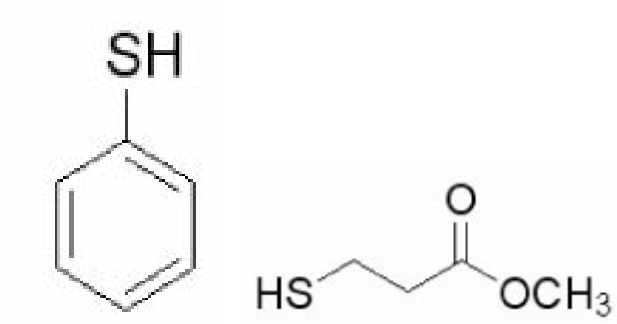

(a) PhSH (b) MMP

Figure 4.9. Chemical formulas of the coupling agents used in the synthesis of ZnS-terpolymer nanocomposite. (a) thiophenol (PhSH), (b)methyl 3-mercaptopropionate (MMP).

In the experiment, 3.72g zinc acetate, 0.98g thiophenol, 0.6g MMP and 0.155g triethylamine were dissolved in a flask containing 40ml of DMF. The flask was then immersed in an ice bath and excess dry H_2S gas was introduced slowly into the flask. The resulting colorless transparent thiol capped ZnS colloid dispersion was sealed in the flask for future experiments. To fabricate nanocomposite film, desired amount of ZnS dispersion and terpolymer were added together into DMF; Then the solvent was evaporated in vacuum to achieve a suitable viscosity; Finally the solution was spin coated, dip coated or directly cast onto glass slide or silicon wafer, followed by overnight curing in vacuum at room temperature. It is important to keep the entire process in dry environment because the nanocomposite is highly moisture sensitive.

Results

The refractive index of the ZnS-terpolymer nanocomposite has been measured by an ellipsometer (Rudolph AutoEL II) equipped with a He-Ne laser working at

633nm (Figure 4.10). The result shows that large change in the index can be readily realized by adding a relatively small amount of ZnS. The refractive index of the nanocomposite can be controlled by the fraction of nanoparticles, and refractive index of 1.5 can be reached with about 10 vol% of ZnS. The nanocomposite shows a transmittance similar to the neat terpolymer in the visible and near-IR ranges (Figure 4.11). The increased UV absorption is mainly due to the intrinsic absorption of ZnS. In addition, no particles were visible in the nanocomposites when viewed with a high resolution scanning electron microscope, which again confirms a very low level of agglomeration. It should be noted that low moisture is critical in the preparation of the nanocomposite. As shown in Figure 4.12, films prepared in dry condition is transparent while those prepared in relatively wet environment are cloudy, which indicates a high level of scattering loss and the existence of large agglomerates. The EO effect of the nanocomposite was measured using a Fabry-Perot interferometry method (Figure 4.13) [4]. An optical path length change of -1.7% at 4μm was achieved under electric field of 45 V/μm in nanocomposite with 10.6 vol % of ZnS, which shows a 37% decrease compared to neat terpolymer [4]. Assuming that the ratios between the contributions of pure refractive index change and dimension change are the same for neat terpolymer and nanocomposite, pure index change is estimated to be Δn/n=-1.3%. We expect that the reduction in E-O effect is partly due to the pure volume effects and partly due to the change in the morphology of the terpolymer induced by the nanoparticles (e.g. crystallinity). On the other hand, by comparing with index matching fluid test, the E-O effects of the nanocomposite coated on fiber in the tunable LPGs are estimated to be Δn/n=0.85% for 3 vol% ZnS under 50MV/m electric field. Again the signs of the refractive index changes are opposite, which is due to the mechanical boundary conditions of the nanocomposite.

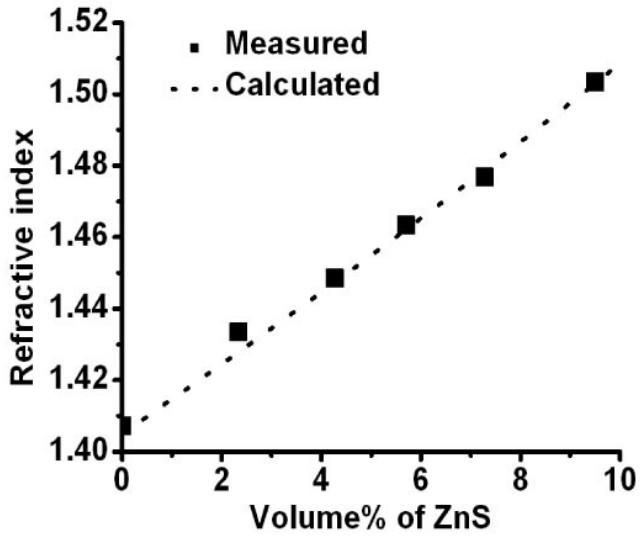

Figure 4.10. The refractive index of the ZnS-terpolymer nanocomposite with different ZnS concentrations.

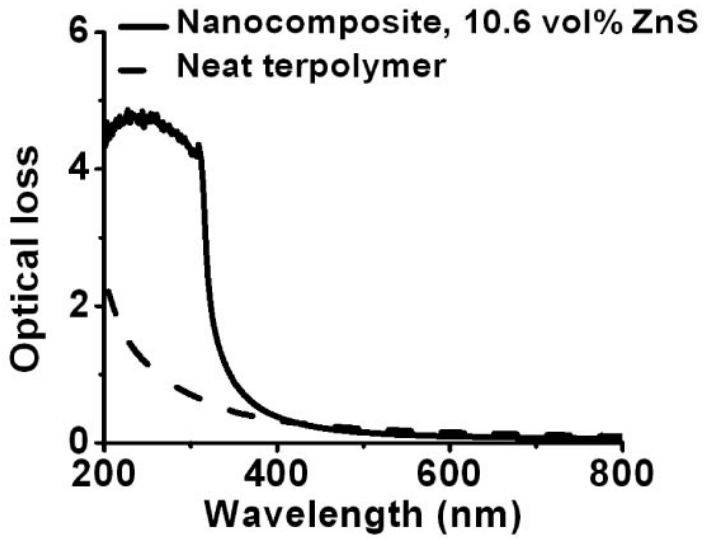

Figure 4.11. The optical loss of neat terpolymer and nanocomposite containing 10.6 vol% of ZnS. The thicknesses of both films are 40μm.

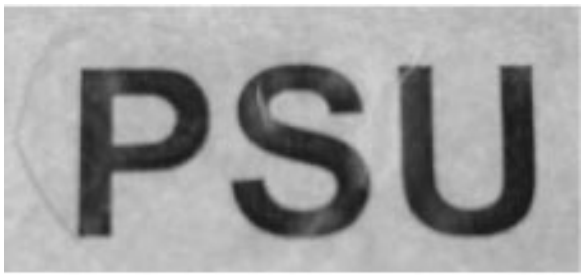

(a) 10vol% ZnS, 30μm, dry condition

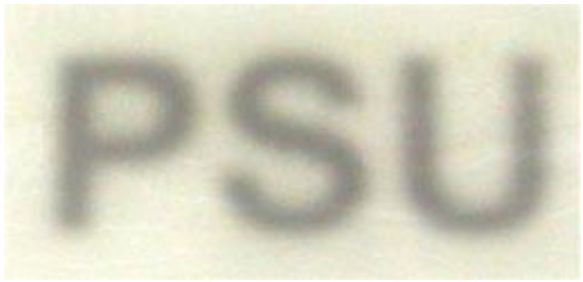

(b) 5vol% ZnS, 30μm, wet condition

Figure 4.12. A comparison of nanocomposite films prepared in (a) dry and (b) wet environments.

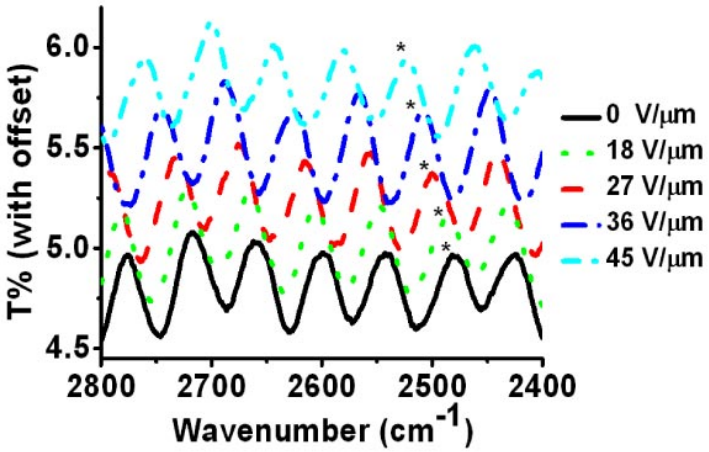

Figure 4.13. Electric field induced shift of Fabry-Perot interference pattern of the nanocomposite film containing 10.6vol% of ZnS. Film thickness: 40 μm. Curves have been offset for easier comparison. "$*$" is marked to guide the fringe shift.

4.5 Results of electrical tuning

The electrical tuning result of an LPG with neat P(VDF-TrFE-CFE) terpolymer as the second cladding is shown in Figure 4.14. It can be seen that under electric field of 100MV/m the tuning range is only about 5nm. However, comparing to index matching fluid test results this already corresponds to a large refractive index change of about 0.02 in the terpolymer. Comparing the transmission spectrum of the tunable LPG with that of the same LPG before without polymer coating (in air), it can be seen that the notch with terpolymer is to the left of that without polymer, which means the notch is due to the first cladding mode. As discussed earlier, it is difficult to induce large tuning using this mode.

Since the resonance wavelength shifts to shorter wavelengths as the electric field increases, the E-O effect induces a positive change in the refractive index of the terpolymer. In some early studies it has been discovered that the E-O effect in the terpolymer depends strongly on the mechanical boundary conditions [4, 44]. Polymer films without any mechanical constraint (free-standing films) show large negative refractive index changes, while films on stiff planar substrates show smaller but positive index change. The films on substrate experience partial constraint that is in the horizontal directions. Therefore, it is expected that there are possibly two different mechanisms contributing to the E-O effect that partly cancel each other. One is related to dimensional change, and the other exists even without dimensional change. Since the free-standing films exhibit large negative index change, we expect that the second mechanism is responsible for the positive index change. Therefore, it is possible that completely clamping the terpolymer can eliminate the canceling effect due to dimensional change.

In order to completely clamp the terpolymer, a tunable LPG coated with neat

terpolymer is further completely covered with epoxy. The epoxy is much thicker and stiffer comparing to the terpolymer, and hence it is expected that the allowed dimensional change of the terpolymer is nearly zero. The electrical tuning of the epoxy covered LPG is shown in Figure 4.15. The achieved tuning range is 15nm, which is two times larger than the tunable LPG without epoxy. Comparing the spectrum in air and with terpolymer, the notch is also due to the first cladding mode. The large tuning range is partially due to the smaller diameter of the fiber. However, it is not expected that the diameter change can result in a three fold change of the tuning range referring to the index matching fluid test and simulation results. Therefore, it is believed that the E-O effect is enhanced by clamping the terpolymer. However, a reliable comparison between the electrical tuning experiment and index matching fluid test cannot be obtained. For instance, in index matching fluid test when the refractive index of fluid increases the notch due to the first cladding mode always shifts to shorter wavelength and becomes shallower. On the other hand, as shown in Figure 4.15, when electric field increases the notch also shifts to shorter wavelength but becomes slightly deeper. This is perhaps due to some non-ideal factors associated with the polymer, such as anisotropy. As a result, the precise refractive index change in the terpolymer has not been determined.

Even the largest tuning range (15nm) achieved in tunable LPGs with neat terpolymer is much smaller than the desired value of 40nm. This is because the refractive index of the terpolymer ($n \approx 1.4$ @ 1550nm) is too low and hence the LPG can only operate with the first cladding mode. As pointed out by the index matching fluid test, in order to achieve the maximun tunability the native refractive index of the terpolymer must be close to an optimum index which is slightly higher than the mode transition index. More specifically, the refractive index of the

terpolymer must be increased by at least 0.02 to reach such value. A nanocomposite approach has been employed to increase the refractive index of the terpolymer while maintaining high transparency and large E-O effect. The nanocomposite consists of terpolymer matrix and zinc sulfide (ZnS) nanoparticles with high refractive indexes (n=2.27 @1550nm). The refractive index of the nanocomposite is determined by the ratio between the terpolymer and ZnS. More details on the nanocomposite is provided in the next chapter and here only the electrical tuning of LPGs based on the nanocomposite will be discussed.

The electrical tuning results of LPGs based on nanocomposites are shown in Figure 4.16. The refractiv e index of nanocomposites containing 3 v% ZnS is 1.42, which is close the optimum index of the LPG shown in 4.5. Indeed, under electric field of 50MV/m a large tuning range of 50nm has been achieved (Figure 4.16a), which is larger than the desired tuning range. If the refractive index of the nanocomposite is further increased to 1.44 (Figure 4.16a), the tuning range decreases again which corresponds to the high index region in Figure 4.5.

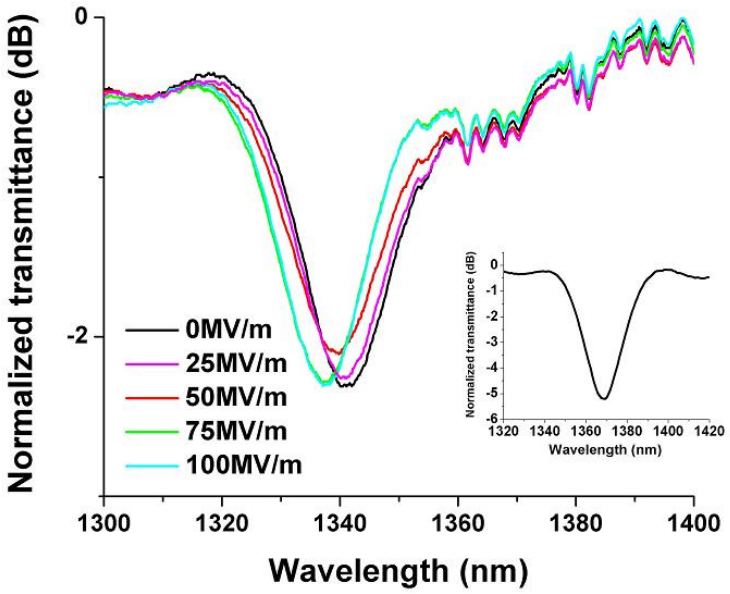

Figure 4.14. The transmission spectrum of an E-O tunable LPG under different applied electric fields. The E-O second cladding is P(VDF-TrFE-CFE) terpolymer. The parameters of the LPG are: fiber diameter: 42μm; Grating period: 400μm; Grating length: 8mm; ITO thickness: 50nm; ITO index: 1.8.

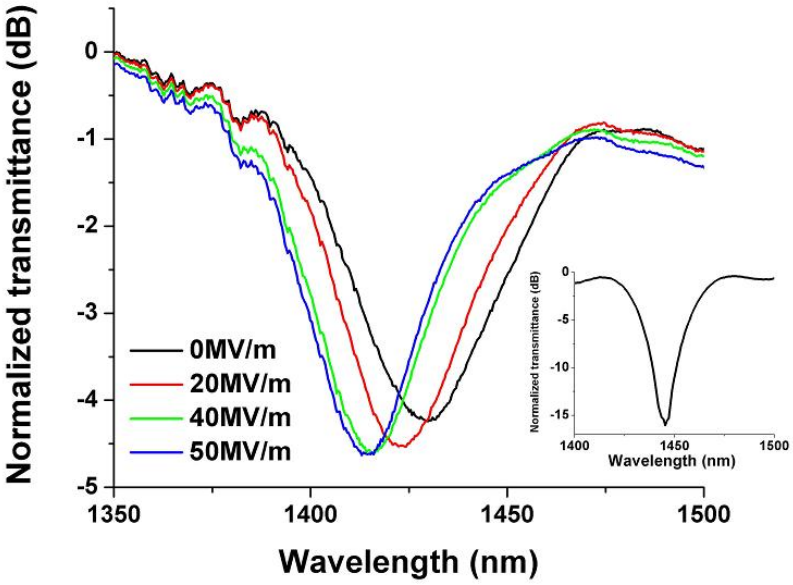

Figure 4.15. The transmission spectrum of an E-O tunable LPG under different applied electric fields. The E-O second cladding is P(VDF-TrFE-CFE) terpolymer. The entire device was embedded into epoxy. The parameters of the LPG are: fiber diameter: 35μm; Grating period: 400μm; Grating length: 8mm; ITO thickness: 50nm; ITO index: 1.8.

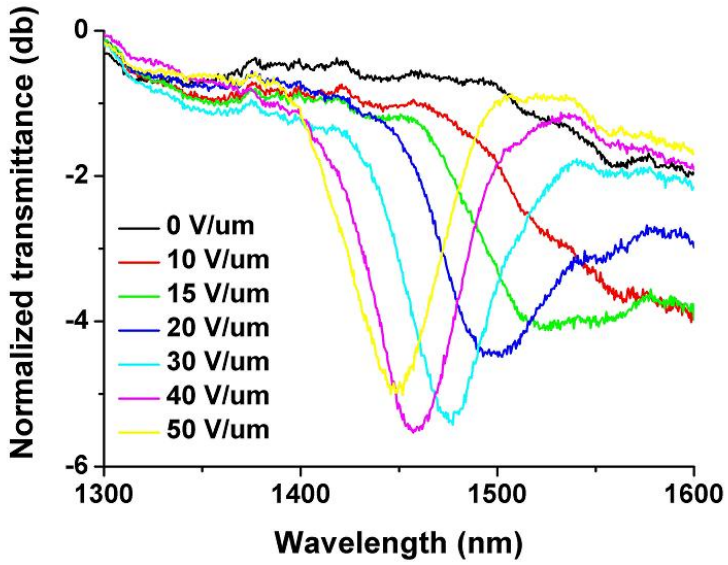

(a) 3vol% ZnS, n=1.42

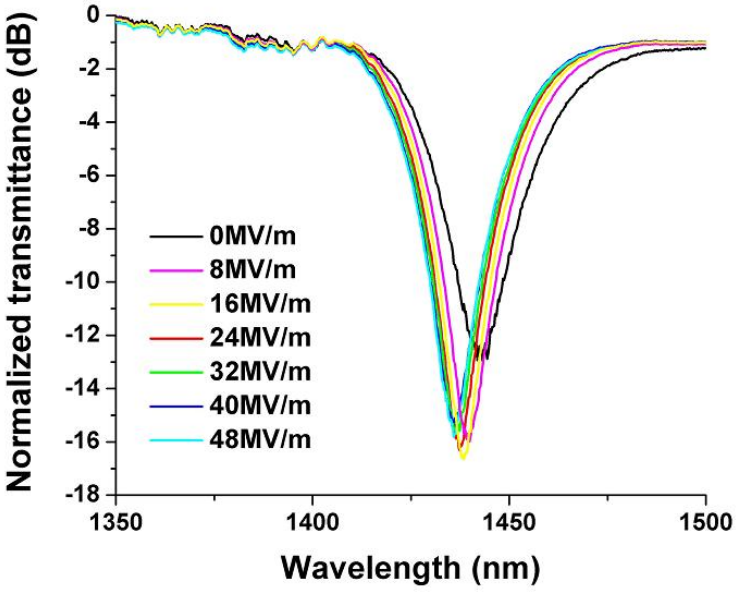

(b) 10vol% ZnS, n=1.44

Figure 4.16. The transmission spectrum of an E-O tunable LPG under different applied electric fields. The E-O second cladding is nanocomposite of P(VDF-TrFE-CFE) terpolymer and zinc sulfide (ZnS). The parameters of the LPG are: fiber diameter: 35μm; Grating period: 400μm; Grating length: 8mm; ITO thickness: 50nm; ITO index: 1.8.

4.6 Discussions and Conclusions

The problem of notch depth

The realization of more than 40nm of tuning in E-O tunable LPGs relies on the mode transitioning in ITO coated fibers. As observed in both index matching fluid test and electrical tuning experiments, when close to transition the notches shift fast but are generally shallow. The transmittance of LPG at the resonance wavelength is given by

$$T = \cos^2(\kappa L)$$

where L is the length of the grating and κ is the coupling coefficient between the core and cladding modes. The coupling strength is in turn proportional to the refractive index change in the grating. When fabricating the tunable LPG, the grating is usually written in air and UV irradiation is stopped when a maximum notch depth is achieved, which means $\kappa_{air} L = \pi/2$. However, when polymer or nanocomposite is coated on the fiber the coupling coefficient decreases and hence the transmittance is no longer zero, resulting in a shallow notch. Therefore, one strategy to increase the notch depth in the high tunability range is to vary the refractive index change in the grating so that $\kappa L = \pi/2$ in this range. An example is shown in Figure 4.17. The mode transition happens at about n=1.43 and the tuning is most sensitive between about n=1.44 and n=1.45. These values are larger than those for the LPGs shown in 4.6. Within the high tunability range (i.e. around 1.44 to 1.45) the notch is deepest at n=1.448 (>20dB) and is shallower for both n=1.452 and n=1.444 (both >10dB). This clearly indicates that it is possible to achieve wide tuning of deep notches. However, it has been difficult to realize such tuning electrically. The major reason is that it requires a terpolymer

refractive index of around 1.44 (@1550nm) which corresponds to relatively high concentration of ZnS in the nanocomposite. It is difficult to incorporate nanocomposite with high ZnS content into tunable LPG while maintaining low scattering loss in the nanocomposite using the current experiment equipment. Although electrical tuning using such high concentration has been demonstrated (Figure 4.16), in that case the LPG is not operating near the mode transition point, and hence the fraction of light energy contained in the nanocomposite is relatively small. When operating close to the transition index much more light energy is contained in the nanocomposite and hence the requirement for scattering loss is more strict. Therefore, when the LPG as shown in 4.17 was coated with nanocomposite the notch depth significantly reduced. This is expected to be improved with better control in the nanocomposite preparation procedures.

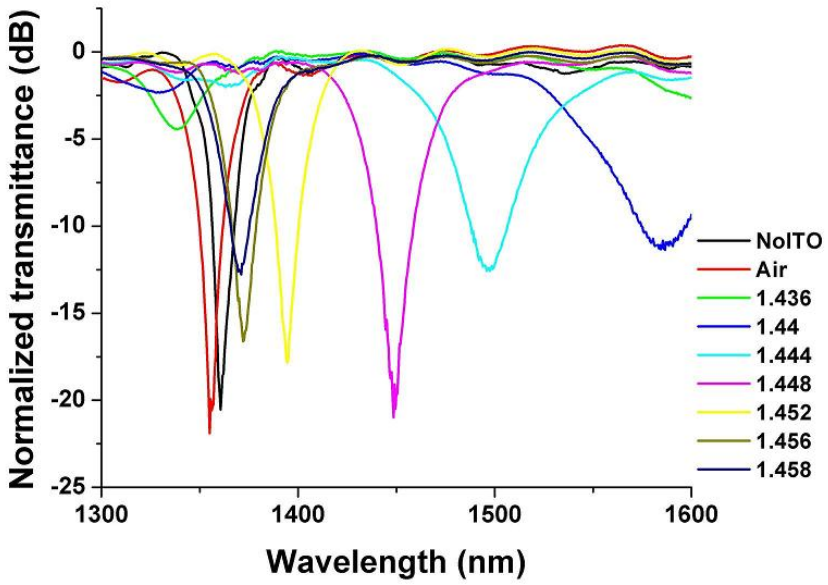

Figure 4.17. Index matching fluid test result for an LPG showing high tunability and deep notch depth. Parameters: Fiber diameter: 41μm; Grating period: 400μm; Grating length: 8mm; ITO thickness: 50nm; ITO index: 1.8.

Non-ideal factors in fabrication

In the fabrication process there are certain non-ideal factors that make the parameters of the fabricated device deviate from the designed values. Some of the major non-ideal factors are associated with the ITO properties. First of all, the deposition process for ITO is very complicated and the properties such as deposition rate, refractive index, and optical loss strongly depend on the deposition conditions. This could induce some batch-to-batch fluctuations of ITO properties. This kind of error can be minimized by precisely controlling all the deposition conditions. Secondly, during the ITO sputtering usually a batch of five or six fibers are processed simultaneously. Fibers placed at different locations will have ITO coatings with different thicknesses due to the target-substrate distance and angle differences. This problem is more serious if the target-substrate distance is small. It is expected that the in-batch variation of ITO thickness is more serious than the batch-to-batch variation in our experiment. This problem can be overcome by using larger target-substrate distances.

Another source of experimental error is the diameter of fiber. In our experiments the fiber thickness was measured using both micrometer and optical microscope. It is estimated that the error associated with the measurement is $\pm 1\mu$m. One of the methods to precisely measure the diameter of the fiber is using SEM to image the cross-sectional of the fiber.

Finally, as discussed earlier the scattering loss in nanocomposite degrade the notch bandwidth and depth of the LPG. The problem of nanocomposite preparation is to be discussed in the next chapter.

According to the simulation results, we expect that the difference of ITO thickness is the major cause of the fluctuation of device performances because it directly

affects the mode transition index. The diameter of fiber affects the resonance wavelength of the LPG and also slightly affects the tunability of the LPG. The quality of nanocomposite is the major concern for notch depth.

Conclusion and Future developments

The tunable LPG with more than 40nm of tuning range find applications in optical communication and sensing systems. However, the structures that enhanced the tuning range are not only limited to LPGs but can be also applied to a wider range of tunable optical devices that are based on waveguides. There are two concepts that have been successfully demonstrated by the tunable LPG. First of all, efficient tuning can be realized "externally", which means the guiding structure can still be made of passive material with very high optical quality (e.g. fused silica) and the active E-O materials serve as cladding layers that contain only evanescent waves. In this way the requirement for the optical quality of the E-O material is much looser and the deposition process of the E-O material can be much easier. Secondly, it was shown that ITO interlayer with proper parameters can significantly modify the mode profiles in waveguides. Near the mode transition point the effective refractive index of modes in the waveguide is very sensitive to the refractive index of the cladding E-O material and hence the tunability is significantly increased. More importantly, the major problem of the external tuning approach is that when the effective refractive index of the mode is tuned the field distribution also varies, but with the high index ITO interlayer it is possible to significantly reduce such variation. This will allow external tuning to be applied in practical tunable optical devices.

Chapter 5

EFFECT OF METAL-POLYMER INTERFACE ON THE BREAKDOWN ELECTRIC FIELD OF P(VDF-TRFE-CFE) TERPOLYMER

5.1 Application of PVDF based electroactive polymers in energy storage capacitors

Energy storage capacitors are important components in power electronic circuits. Currently, these capacitors often occupy large volume due to the low energy density of capacitor materials. Therefore, materials that can store and release high electrical energy density is highly desirable.

The energy storage capacitors in high voltage, high power applications are usually made of dielectric polymer films. Currently the most common polymer for this application is polypropylene. Generally speaking, the electric energy density stored in dielectric material can be expressed as

$$U_e = \int EdD \tag{5.1}$$

where E is the electric field and D is the dielectric displacement. For dielectric materials with linear response (dielectric constant is independent of electric field) we have

$$U_e = \frac{1}{2} K \epsilon_0 E^2 \tag{5.2}$$

where ϵ_0 is the permittivity of vacuum and K is the dielectric constant of material. Current dielectric polymers have very low dielectric constants. For instance, in polypropylene K=2.2 and hence even if the breakdown electric field is as high as 600MV/m, the maximum energy density is only about 3J/cm^3. On the other hand, P(VDF-TrFE-CFE) terpolymer and P(VDF-CTFE) copolymer have much higher dielectric constants of K=50 and K=13, respectively. Therefore, they are expected to achieve much higher energy densities.

In P(VDF-TrFE-CFE), indeed a very high energy densities of about 9J/cm^3 has been measured (Figure 5.1) [18]. However, the measured energy density of the terpolymer is much lower than predicted by equation (5.2) where 35J/cm^3 should be achieved under 400MV/m if K=50. This is because the effective dielectric constant defined by

$$K_{eff} = \frac{1}{\epsilon_0} \frac{dD}{dE} \tag{5.3}$$

decreases significantly at high electric fields (Figure 5.1c) and hence equation (5.2) is no longer valid in this case. The decrease of dielectric constant is due to saturation of polarization (Figure 5.1a). Intuitively, it can be imagined that there is only certain number of available polarization in the polymer which is mainly determined by the dipole moment carried by the chains; if the dielectric constant is too large the polarization will be "depleted" quickly and saturation will happen. Therefore, in order to achieve higher energy density it is desirable that the dielectric constant of the polymer is lowered so that the same polarization level can be achieved at much higher electric field.

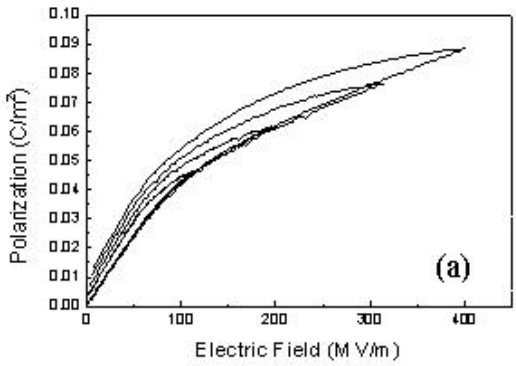

(a) D-E loop

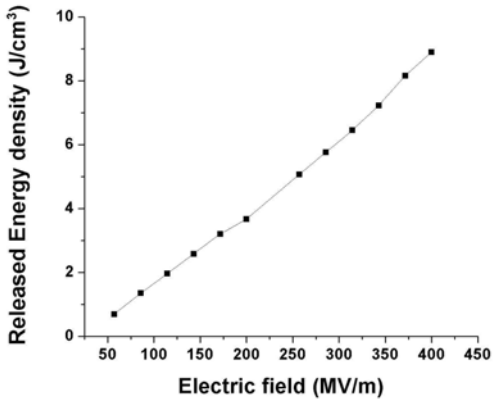

(b) Energy density

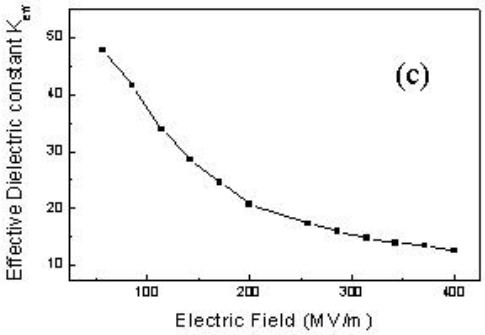

(c) Effective dielectric constant

Figure 5.1. D-E loop, energy density and effective dielectric constant of P(VDF-TrFE-CFE) terpolymer 63/37/7.5 mol%. Adapted from [18]

The D-E loop, released energy density and efficiency of P(VDF-CTFE) film are shown in Figure 5.2. Although low field dielectric constant (K=13) of the film is much lower than the terpolymer (K∼50), the effective dielectric constant does not decrease significantly at high fields and much higher energy density can be achieved. For instance, under 600MV/m the released energy density from stretched P(VDF-CTFE) film is as high as 25J/cm^3.

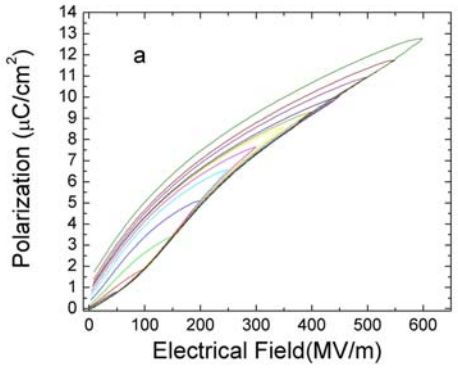

(a) D-E loop

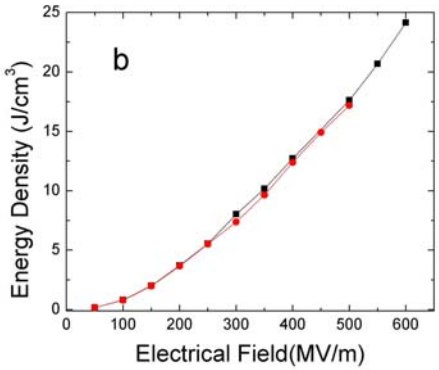

(b) Energy density

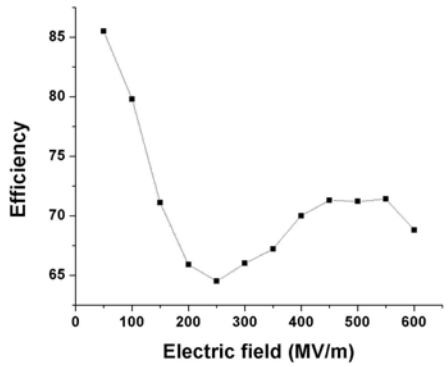

(c) Efficiency

Figure 5.2. D-E loop, energy density and energy efficiency of stretched (5 times) P(VDF-CTFE) copolymer film. Adapted from [52]

Both the terpolymer and the copolymer are promising candidates as dielectric material for energy storage capacitors. For instance, when relatively large energy density is required at moderate voltage the terpolymer can be used. On the other hand, the copolymer can be used to achieve ultrahigh energy densities. However, in order to be applied in capacitors there are some issues to be addressed in addition to the energy density, such as breakdown electric field and energy efficiency. The breakdown electric field of the terpolymer ($\sim$300MV/m) is relatively low comparing to polypropylene and the copolymer (>600MV/m). This affects not only the highest achievable energy density but also the reliability of the film. Therefore, it is imperative to understand what controls the breakdown in the terpolymer. On the other hand, the energy efficiency η is defined as the ratio between released and stored energy,

$$\eta = \frac{U_{release}}{U_{store}} \tag{5.4}$$

In the P(VDF-CTFE) copolymer the efficiency is relatively low (Figure 5.2c), and hence it is important to understand the mechanism of the energy loss and seek for methods to reduce the loss.

This chapter discusses the electric breakdown in the P(VDF-TrFE-CFE) terpolymer films. It is found that the breakdown field of the relaxor terpolymer depends critically on the electrode-polymer interface properties and the electrodes with less charge injection also resulted in higher breakdown fields. The difference in charge injection between different electrode materials is attributed to both the difference in Schottky barrier height and the composition and morphology of the interface.

The problem of energy loss and improvement of efficiency of P(VDF-CTFE)

copolymer will be discussed in Chapter 6.

5.2 Effect of metal-polymer interface on the breakdown electric field of P(VDF-TrFE-CFE) terpolymer

The relaxor ferroelectric terpolymer with a composition of P(VDF-TrFE-CFE) 63/37/7.5 mol% was used in this investigation. The terpolymer powder was synthesized via a suspension polymerization process at Piezotech of France [53]. Polymer films were fabricated using solution cast method with dimethylformamide as the solvent. After casting the films were annealed at 120°C for more than 2 hrs to remove residual solvent and to raise the crystallinity. The films were then uniaxially stretched to more than five times of the original length to induce high degree of polymer chain orientation, which improves the breakdown field of the films [5, 18]. The typical film thickness was about 15μm. Electrodes of 2.46 mm diameter were deposited on both sides of the films by sputtering or evaporation of different metals. For the Cr electrodes, an additional layer of Au was coated on the top to improve the conductivity. The breakdown field was measured according to ASTM standard with a voltage ramp rate of 500 V/sec. The leakage current (I-V curve) was measured by a Keithley 6517A electrometer. For each voltage value, the current was recorded after the voltage was applied for 5 seconds and then the sample was shorted for another 5 seconds. The dielectric measurements were performed using a HP 4284A LCR meter. The polarization characterization was carried out with a Sawyer-Tower circuit. All the experiments were carried out at room temperature (22°C). For the study of metal-polymers using FTIR, terpolymer film of less than 50nm was spin coated on silicon wafer and metal layers of about 5nm thick was coated on top of the polymer. Measurement was performed

using an FTIR in grazing angle macro ATR mode. For XPS (x-ray photoemission spectrum) measurements, terpolymer film of about 100nm thick was first coated on silicon wafer and then ultrathin aluminum films with various thicknesses were coated on the polymer films.

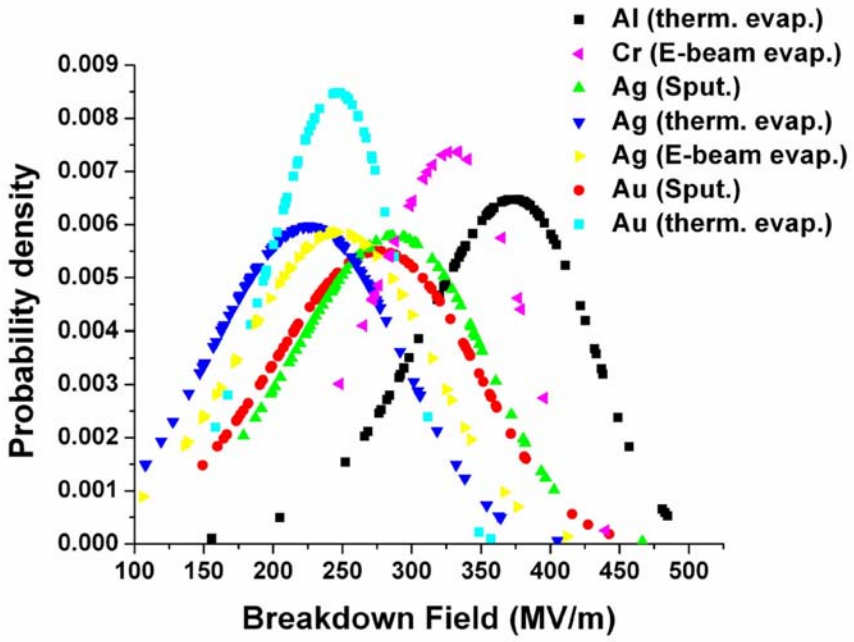

Figure 5.3. Electric breakdown field of terpolymer films coated with different metal electrodes and with different deposition methods. [69]

The distribution of breakdown fields for different electrode materials prepared under different deposition conditions are presented in Figure 5.3. The distribution of breakdown field of materials can be fitted by Weibull statistic model [54]:

$$P(F) = 1 - \exp[-(\frac{F}{\alpha})^{\beta}] \tag{5.5}$$

where F is the electric field and $P(F)$ is the probability of the sample to breakdown at electric field F. The fitting parameters α and β reflect the characteristic value (electric field under which 63.2% of samples breakdown) and spread of breakdown

Electrode	Work function (eV)	α	β
Al (thermal evaporation)	4.26	382.75	6.66
Cr (e-beam evaporation)	4.5	337.70	6.69
Ag (sputtering)	4.74	303.14	4.65
Ag (thermal evaporation)	4.74	244.58	3.82
Ag (e-beam evaporation)	4.74	265.18	4.08
Au (sputtering)	5.31	294.29	4.27
Au (thermal evaporation)	5.31	254.64	5.78

Table 5.1. The Weibull parameters for breakdown field distribution of the terpolymer films with different electrodes under different deposition conditions. The work functions are literature values for 111 plane (Al, Au, Ag) or for polycrystalline film (Cr).

field. Values of α and β for different electrode materials and deposition conditions are summarized in Table 5.1 and Figure 5.4. It can be readily seen that both the characteristic value and the width of distribution of breakdown field are dependent on the electrode material and deposition method. Therefore, it is expected that electric breakdown in the terpolymer films is governed by the metal-polymer interface rather than the bulk properties of the terpolymer.

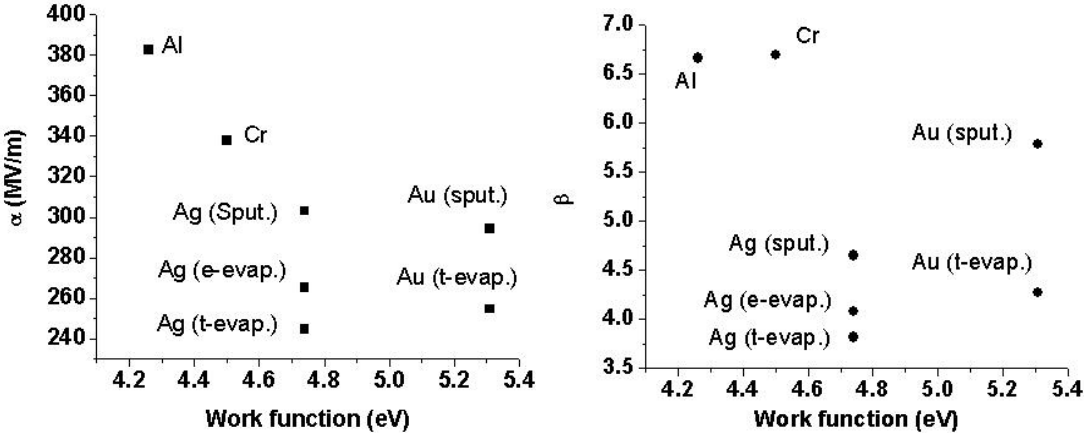

(a) α (b) β

Figure 5.4. The Weibull parameters for breakdown field distribution of the terpolymer films vs. work function for different electrodes and deposition conditions.

Figure 5.5 presents the J-V curves of the films which show that similar to the breakdown field, the leakage current depends on both the electrode material and

deposition condition. Such dependence suggests that the conduction is limited by charge injection from electrodes. For all the electrodes the currents exhibit saturating behavior for low to medium fields (<50MV/m) and increases rapidly under high fields (>80MV/m). The saturating behavior differs significantly among different electrodes as well as deposition conditions, and hence is believed to be due to the trap filling effect near the interface [55]. Comparing the high field J-V curve to the polarization measurement (D-E loops shown in Figure 5.5b) reveals that the onset of rapid increase of leakage current and deviation from low-field linear relationship in the D-E loop happen at similar electric fields (about 80MV/m). This suggests possible relationship between charge injection and the molecular conformational change associated with the dielectric response of the terpolymer [3, 56, 57].

Comparing the breakdown fields with leakage currents, it can be found that higher leakage current corresponded to lower and broader distributed breakdown field. This correspondence suggests that breakdown is possibly related to the charge injection process at the metal-polymer interfaces. Charge injection is one of the major cause of electric breakdown in inorganic and polymer films, and the underlying mechanisms includes impact ionization, bond cleavage, space-charge formation, Joule heating, etc. [54, 58, 59, 60].

The basic mechanism of charge injection includes Schottky emission and tunneling. In both processes the injection current J is dependent on the interfacial barrier height ϕ_B [75]:

$$J \propto \exp(-C\phi_B^{\alpha}) \tag{5.6}$$

where $\alpha = 1$ for Schottky emission and $\alpha = 1.5$ for tunneling, and C is a

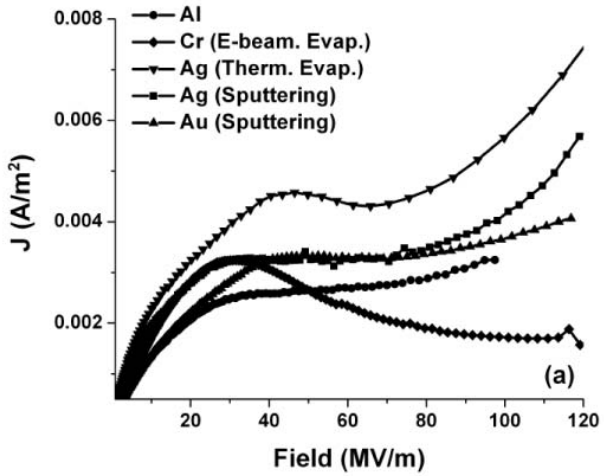

(a) J-V curves

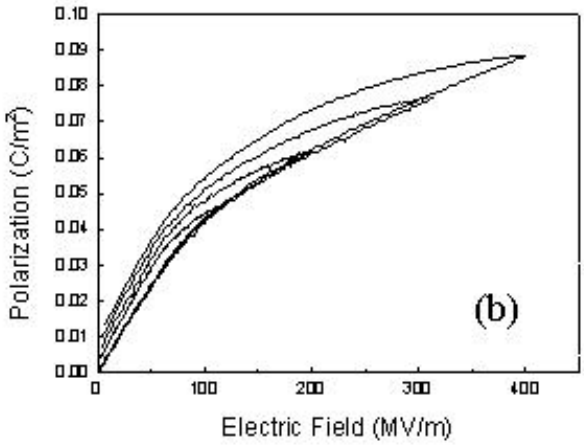

(b) D-E loops

Figure 5.5. (a) I-V curves of terpolymer films coated with different metal electrodes under different deposition conditions. (b) D-E curves of terpolymer films coated with sputtered gold electrodes.

coefficient independent of ϕ_B. In the terpolymer films, electrodes with higher work functions generally results in larger leakage currents and lower breakdown fields (Table 5.1). According to equations (5.6), this can be explained by the dominance of hole injection in the charge injection process. This is consistent with

the previous observation on charge injection into PVDF base polymers [61, 62].

Some of the detailed behaviors of the breakdown field and leakage current in the terpolymer films cannot be explained by barrier height difference alone. For instance, the work function of Ag is closer to Cr than Au, but its breakdown and conduction behaviors resemble Au rather than Cr. Furthermore, different preparation conditions of same metal resulted in different characteristics (Figure 5.3, 5.5a). Recently, it has been discovered that the composition and morphology of the metal-polymer interface play an important role on the charge injection process in many polymers [63]-[67]. For instance, noble metal such as Au and Ag exhibits high conductivity even for very thin films and tend to diffuse into polymers [63]-[65]. On the other hand, more reactive metal such as Al often reacts with polymers to forms insulating thin layer which is expected to reduce the charge injection and impedes the diffusion of metal into polymer [65]-[67]. It is also expected that interfaces with insulating layers are sharper than diffusion-type interfaces and hence should result in narrower distribution of breakdown field. These expectations are consistent with the experimental observations for the terpolymer (Table 5.1). In order to study the properties of the electrode-polymer interfaces of the terpolymer, ultrathin films ($<$ 100nm) have been fabricated by spin coating and Ag and Al electrodes were deposited by thermal evaporation. Assuming interfacial layers with thickness d_s and dielectric constant ϵ_s are present at both electrodes, the overall dielectric constant of the film, ϵ, can be expressed as [68]:

$$\frac{1}{\epsilon} = \frac{1}{\epsilon_f} + \frac{2d_s}{d}(\frac{1}{\epsilon_s} - \frac{1}{\epsilon_f}) \tag{5.7}$$

where ϵ_f is the dielectric constant of the terpolymer and d is the total thickness of the film. The effective dielectric constant of Al coated terpolymer films with

different thicknesses (Figure 5.6) fits fairly well to equation (5.7) and yields ϵ_f = 67.3 and d_s=4.4nm (assuming $\epsilon_s = 5$). These values are consistent with the native dielectric constant of terpolymer and the typical thicknesses of interfacial layers and indicates the existence of interfacial layer. For the films with Ag and Au electrodes, no such blocking layer was found and ultrathin films tend to form short circuit, indicating the diffusion of silver into polymer.

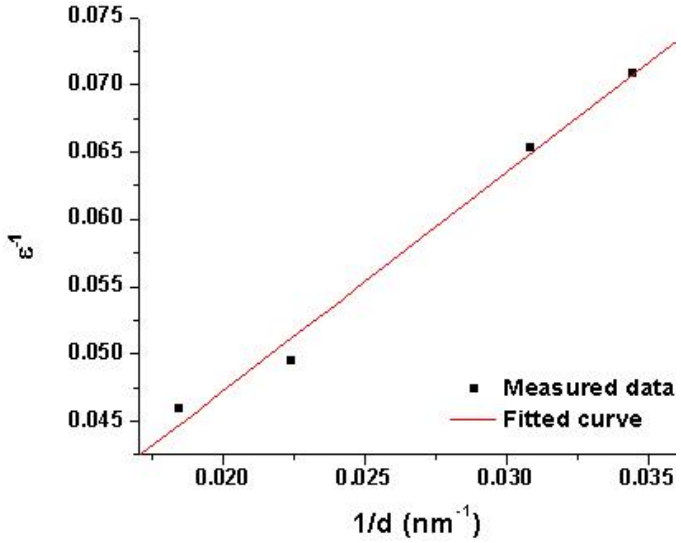

Figure 5.6. Dielectric constant of terpolymer films coated with Al electrodes (evaporated) as a function of the inverse of film thickness.

The existence of interfacial reactions is also confirmed by FTIR measurements (Figure 5.7). Comparing to pure terpolymer films, there is a clear additional peak at around 950cm−1 in aluminum coated films. This feature is absent in Au coated films. Therefore, this indicates reaction between terpolymer and deposited aluminum. The formation of interface between aluminum and the terpolymer was further studied using XPS. The XPS measurement probes the inner electrons in atoms and the resonance peaks not only depends on the type of atom but also depends on its chemical environments. Therefore, chemical reactions are indicated by the shift of peaks. The peaks of aluminum, fluorine, and oxygen clearly shifted

for aluminum thicknesses from 0nm to 4nm (Figure 5.8). On the other hand, the peak of chlorine didn't show clear shift. The terpolymer itself doesn't contain oxygen atoms and hence the oxygen is expected to come from the residual gases (oxygen or water vapor) in the deposition chamber or adsorbed on the surface of polymer.

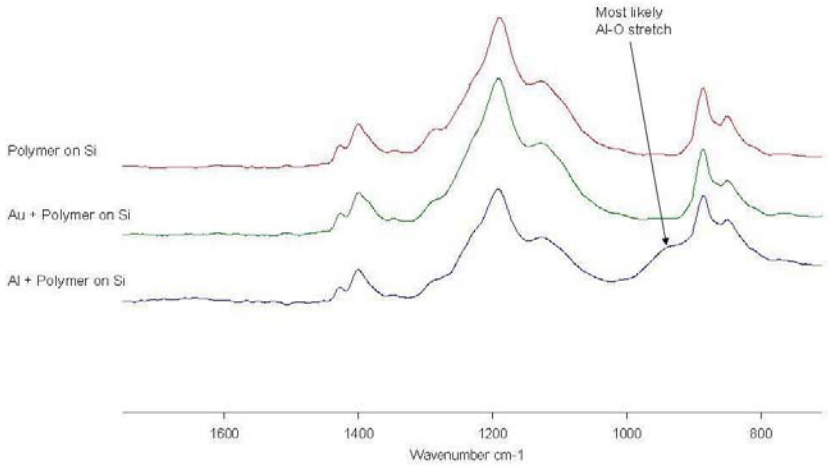

Figure 5.7. FTIR spectrums of neat terpolymer and terpolymer coated with very thin Au or Al layers.

5.3 Conclusions

In conclusion, the dependence of dielectric breakdown field of P(VDF-TrFE-CFE) on electrode material has been studied. It is observed that electric breakdown is mainly controlled by metal-polymer interface and the interfaces with smaller injection current possess higher breakdown field. The interface states can be influenced by both the electrode material and deposition condition. Reactive metals such as aluminum and chromium result in less charge injection, higher breakdown field and narrower distribution of breakdown field comparing to inert metals such as

gold and silver. The differences arise from both the different work functions of the metals and the formation of interfacial layers.

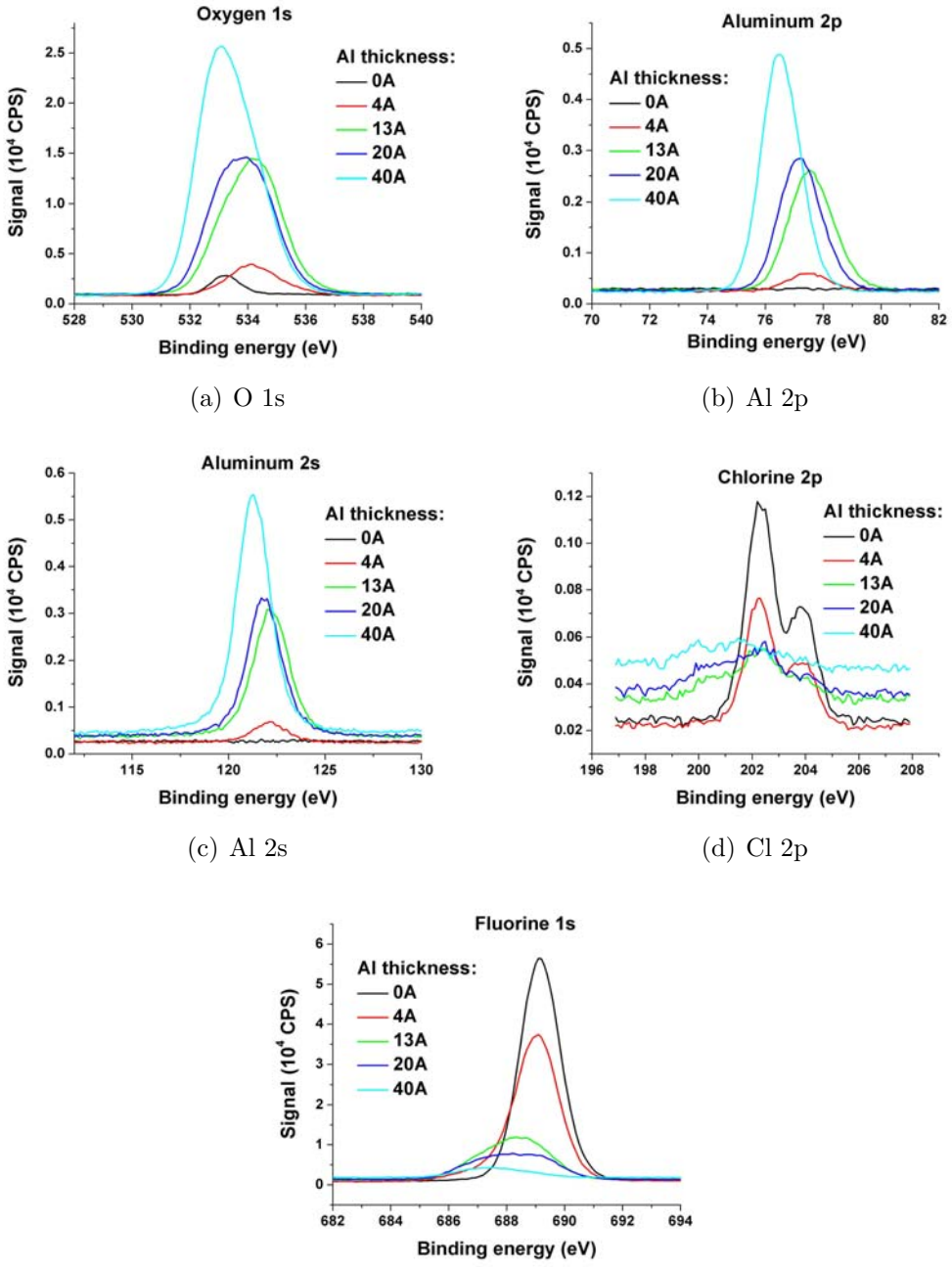

(a) O 1s

(b) Al 2p

(c) Al 2s

(d) Cl 2p

(e) F 1s

Figure 5.8. XPS spectrums of neat terpolymer and terpolymer coated with ultrathin Al layers with different thicknesses

Chapter 6

CONDUCTION LOSS IN P(VDF-CTFE) COPOLYMER

The poly(vinylidene fluoride - chlorofluoroethylene) copolymer, P(VDF-CTFE), is able to achieve energy density of as high as 25J/cm^3. However, its energy efficiency is relatively low, especially under certain range of electric field (Figure 5.2c). For instance, the efficiencies of stretched P(VDF-CTFE) film are 65% at 250MV/m and 71% at 500MV/m, while in polypropylene the efficiency is usually higher than 90%. In this chapter, I will first analyze the different types of energy loss. Then the mechanisms of conduction loss will be investigated. After that, experimental results of using blocking layers to reduce the conduction loss will be presented.

6.1 The energy loss in P(VDF-CTFE) copolymer

The D-E loops of stretched and un-stretched P(VDF-CTFE) films are shown in Figure 6.1a,b. Both films were fabricated by extrusion. In general, in a D-E

loop illustrated in Figure 6.2, the areas I+II, I and II represent the stored energy, released energy and energy loss. Approximately speaking, the loss (the area II) is proportional to the remnant electrical displacement D_r, which is defined as the electrical displacement when the electric field returns to zero in the loop test.

In general, under electric field there are two types of losses existing in dielectric polymers, namely, dielectric loss and conduction loss. Dielectric loss is due to dielectric relaxation of the polymer and conduction loss is due to transportation of charge carriers in the polymer. The two types of losses can be identified from the dependence of D_r on loop period. The conduction loss exhibits a nearly linear dependence, while the portion of loss that is independent of loop period is due to dielectric loss [1]. In stretched and un-stretched P(VDF-CTFE) films both types of losses can be observed (Figure 6.1c,d). A marked difference between stretched and un-stretched films is that in stretched film the dielectric loss ($\sim 0.01 C/m^2$ at 400MV/m) is considerably higher than in un-stretched film ($\sim 0.05 C/m^2$ at 400MV/m), while the conduction loss of un-stretched film is much higher than stretched film. The larger dielectric loss in stretched film is due to ferroelectric transition, which is evident from the increase of the slope of D-E loop at around 100MV/m (Figure 6.1a).

In order to improve the efficiency, both the conduction loss and the dielectric (ferroelectric) loss need to be reduced. The study in this thesis focuses on understanding and reducing the conduction loss.

[1] Dielectric loss can also be strongly time dependent if the frequency of loop is close the the frequency of a relaxation peak. However, no relaxation peak was observed in the frequency under consideration in P(VDF-CTFE). [52]

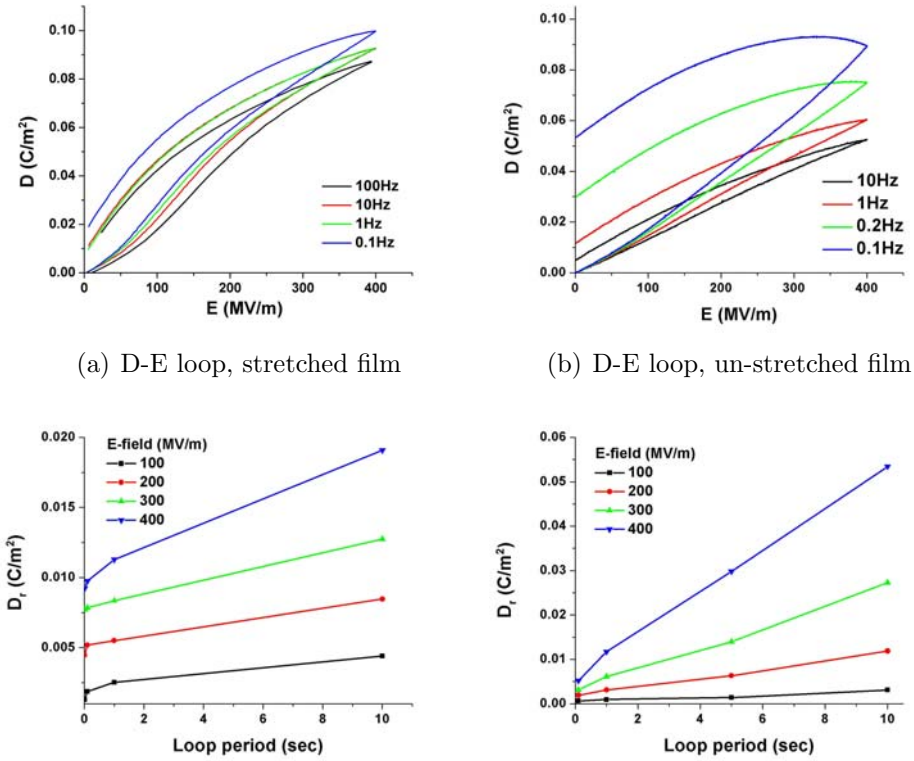

(a) D-E loop, stretched film

(b) D-E loop, un-stretched film

(c) D_0, stretched

(d) D_0, un-stretched

Figure 6.1. (a), (b): The D-E loops of stretched and unstretched P(VDF-CTFE) films. (c), (d): D_r, the remnant displacement, of stretched and unstretched films.

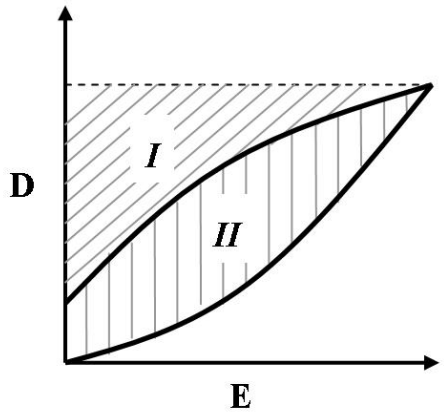

Figure 6.2. The electrical energies in a typical D-E loop.

6.2 Mechanisms of electrical conduction in polymers

The electrical conduction in dielectric polymers is very complicated. Before discussing the details of conduction phenomenon in P(VDF-CTFE) copolymer, I will very briefly review the theory of electrical conduction in solids. A detailed discussion on this topic can be found in [9].

In general, the measured leakage current of a polymer film consists of two parts:

$$J = J_c + J_d \tag{6.1}$$

where J_c is the conduction current and J_d is the displacement current. The displacement current is due to the change of electrical displacement with time,

$$J_d = \frac{\partial D}{\partial t} \tag{6.2}$$

On the other hand, the conduction current is produced by real motion of charge carriers. Displacement current is closely related to dielectric relaxation in the polymer and could be important for highly polar polymers such as P(VDF-CTFE). However, we will not consider it here since conduction loss is expected to dominate under high fields.

General process of electrical conduction

The source of charge carriers

The charge carriers that contribute to conduction current can be intrinsic carriers that are provided by the material itself or external carriers that are injected from

electrodes. Examples of intrinsic carriers are free electrons and holes in semiconductors and the mobile ions in ionic conductors. The P(VDF-CTFE) copolymer is a highly insulating material and it is not likely to contain large number of charge carriers by itself. Therefore, the electrical conduction in the copolymer is due to carriers injected from electrodes.

Conduction process

The energy band diagram of a metal-polymer-metal structure as well as common conduction processes in polymer are illustrated in Figure 6.3. The HOMO (Highest Occupied Molecular Orbital) and LUMO (Lowest Unoccupied Molecular Orbital) in a polymer take the place of valence band edge and conduction band edge in semiconductors. The electrical conduction due to injected carriers from electrodes consists of three steps:

1. Charge injection from electrode into polymer.
2. Charge transportation in the bulk of polymer.
3. Charge exits polymer and returns to electrode.

For each step there are often several different mechanisms. For instance, charge can be injected from electrode into polymer through Schottky emission, field emission, and injection into trap states. On the other hand, bulk transportation includes band conduction and hopping that are affected by the existence of traps.

The steps 1 to 3 are can be imagined as three resistors connected in series, and hence the step with lowest rate will limit the overall conduction current. In general, the exiting step is not the limiting step since for polymers there is usually

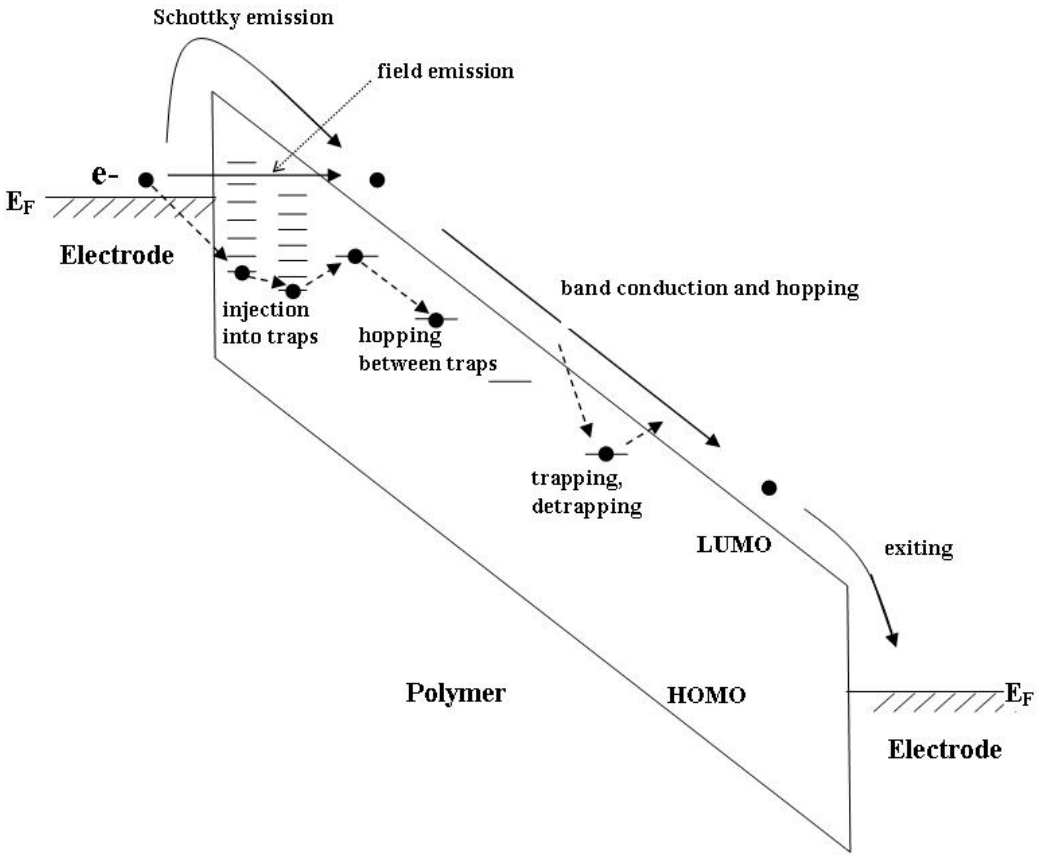

Figure 6.3. Energy band diagram and different conduction processes in polymer film.

no energy barrier at the exiting interface [2]. On the other hand, carriers injected from electrode to polymer experience an energy barrier at the electrode-polymer interface due to the difference between electrode Fermi level and HOMO (LUMO) of the polymer. Therefore, the conduction in polymers can be bulk limited or electrode (injection) limited, depending on which step limits the current.

Bulk limited conduction

Carriers are first injected from electrode into polymer and then transported in the bulk of polymer. If the mobility of polymer is low and the rate of bulk transporta-

[2]Even if there is an energy barrier, the exiting process can treated in similar way as for charge injection and hence will not be considered separately

tion is much slower comparing to the rate of supply of carrier by the electrode, the conduction is bulk limited.

The charge carried by intrinsic carriers in material is always compensated by opposite charges. For instance, in semiconductors the electrons are compensated by holes or ionized donors. Therefore, the net charge density in bulk material is zero. Unlike intrinsic carriers, carriers injected from contacts into polymer are not compensated and instead form space charges. The space charges alter the electric field distribution in the polymer. Consider the case where hole is the major carrier and using band conduction model, the space charge limited conduction is generally described by the following equations [9]:

$$\frac{dF(x)}{dx} = \frac{q[p(x) + p_t(x)]}{\epsilon} \tag{6.3}$$

$$J = q\mu_p p(x) F(x) \tag{6.4}$$

$$p_t(x) = \int_{E_l}^{E_u} h(E, x) f_p(E) dE \tag{6.5}$$

$$p(x) = N_v exp(-E_{Fp}/kT) \tag{6.6}$$

where $F(x)$ is the electric field, $p(x)$ and $p_t(x)$ are the concentration of free and trapped holes, ϵ is the permittivity, μ_p is the mobility of holes, E_l and E_u are the lower and upper energy of trap distribution, $h(E, x)$ is the concentration of traps, $f_p(E)$ is the probability of trapping, N_v is the valence band density of state, and E_{Fp} is the quasi Fermi energy for holes. Diffusion has been neglected since only high field conduction is of interest to us. Similar formula can be obtained for conduction involving electrons only or both types of carriers. Due to the existence of traps in polymer, part of the space charges may be trapped charges and cannot

Trap distribution	Current density
Trap-free	$J = \frac{9}{8}\epsilon\mu_p\frac{V^2}{d^3}$
Single discrete level	$J = \frac{9}{8}\epsilon\mu_p\theta\frac{V^2}{d_{eff}^3}$
Exponential	$J = q^{1-l}\mu_p N_v(\frac{2l+1}{l+1})^{l+1}(\frac{l}{l+1}\frac{\epsilon}{H_b'})^l\frac{V^{l+1}}{d_{eff}^{2l+1}}$
Gaussian (shallow)	$J = \frac{9}{8}\epsilon\mu_p\theta\frac{V^2}{d_{eff}^3}$
Gaussian, (deep)	$J = q^{1-m}\mu_p N_v(\frac{2m+1}{m+1})^{m+1}(\frac{m}{m+1}\frac{\epsilon}{H_b'})^m\frac{V^{m+1}}{d_{eff}^{2m+1}}$,
Uniform	$J = 2q\mu_p N_v g_p\frac{V}{d_{eff}}\exp[-\frac{E_u-E_l}{kT}]\exp[2\frac{\epsilon V}{qH_c kTd_{eff}^2}]$

Table 6.1. Current density for space charge limited conduction [9].

contribute to conduction. The current density depends on the energy distribution of traps. This topic is discussed in detail in [9]. A summary of the formulas for some common distributions are given in Table 6.1 as a reference. The trap distributions and some related parameters appeared in the table are:

- Exponential, $H(E) \approx \exp(-\frac{E}{kT_c})$, $l = T_c/T$
- Gaussian, $H(E) \approx \exp[-\frac{(E-E_{t0})^2}{2\sigma_t^2}]$, $m = [1 + 2\pi\sigma_t^2/16k^2T^2]^{1/2}$
- Uniform, $H(E) = H_c$, $E_l < E < E_h$

The parameter θ in the expression of current density represents the ratio between the numbers of free carrier and total space charge. The effective thickness d_{eff} account for the effect of spatial distribution of traps.

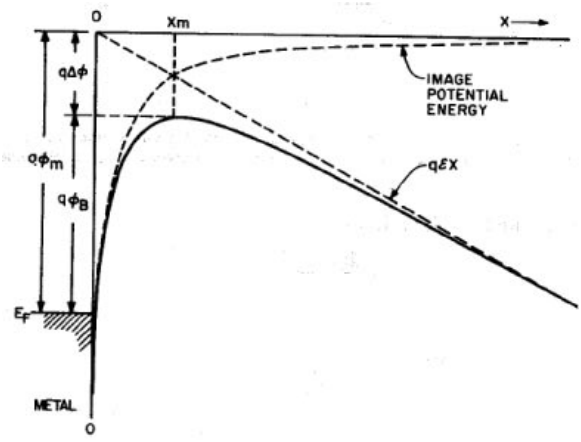

Figure 6.4. The band structure of metal-insulator contact showing the image force effect. Adapted from [75]

Electrode limited conduction

If the injection of carriers into polymer is so difficult that the electrode cannot supply enough carriers for bulk transportation, then the conduction is electrode limited (or injection limited). The energy band structure of a typical metal-insulator contact with applied electric field is shown in Figure 6.4. The carrier can overcome the barrier by acquiring sufficient thermal energy to surpass the barrier, or it may also directly penetrate through the barrier via quantum mechanical tunneling processes. These two mechanisms are called thermionic (Schottky) emission and field (Fowler-Nordheim) emission, respectively. Usually Schottky emission dominates at high temperatures while field emission dominates under high electric fields and moderate temperatures.

Barrier lowering due to image force

A charge carrier that is close to the electrode-polymer interface experiences electrical forces generated by both the applied electric field and image charge induced by the metal electrode. The energy of the carrier in the polymer with respect to

electrode Fermi energy is given by

$$E(x) = \phi_B - \frac{q^2}{16\pi\epsilon x} - qFx \tag{6.7}$$

where ϕ_B is the original energy barrier height, F is the applied electric field and ϵ is the permittivity of the polymer. Therefore, the maximum energy that correspond to the modified barrier height is given by:

$$\phi'_B = \phi_B - \Delta\phi = \phi_B - \sqrt{\frac{qF}{4\pi\epsilon}} \tag{6.8}$$

and the peak of barrier is no longer at the interface ($x = 0$) but moved to

$$x_m = \sqrt{\frac{q}{16\pi\epsilon_0 F}} \tag{6.9}$$

It has been suggested that since the transit time of carriers across the electrode-polymer interface is very short, the dielectric constant at optical frequency should be used when calculating the image force effect.

Schottky emission

The injection current is generally given as

$$J = q \int D v_x [n_1(E) - n_2(E)] dE \tag{6.10}$$

where D is the transition probability, v_x is the velocity of carrier in x direction, and $n(E)$ is the number of carriers with energy in the interval between E and $E + dE$. Both the transition probability and limit of integration depend on the mechanism of injection. For Schottky emission, all the carriers with energies higher than the

injection barrier can move into the insulator and the current density is given by [75]

$$J = A^* T^2 \exp(-\frac{q\phi_B}{kT}) \exp(\beta F^{1/2}) \tag{6.11}$$

where A^* is the Richardson constant:

$$A^* = \frac{4\pi q k^2 m^*}{h^3} \tag{6.12}$$

and

$$\beta = \sqrt{\frac{q}{4\pi\epsilon}} \tag{6.13}$$

Field emission

For field emission (Fowler-Nordheim emission, F-N emission), the transition probability D is the quantum tunneling probability D_T. The WKB approximation is usually utilized to calculate D_T:

$$\begin{aligned} D_T &= \exp[-\frac{4\pi}{h}(\int_{x_1}^{x_2} |p_x| dx)] \\ &= \exp\{-\frac{4\pi}{h}[\int_{x_1}^{x_2} \sqrt{2m^*[E_\perp - E + E_C(x)]} dx\} \end{aligned} \tag{6.14}$$

where E_C is the conduction band edge for the insulator film and p_x is the x-component of momentum. Since for tunneling the energy barrier height is larger than the kinetic energy of carrier and the y- and z- components of momentum should be constant, p_x is imaginary and $|p_x|$ represents the imaginary part of momentum. It should be noted that the physical meaning of WKB approximation

is to neglect the multiple reflections of the electronic wave. Therefore, it can be expected that while it is a good approximation for single layer films, there would be larger error for multilayered films.

The final form of D_T and hence the injection current density depends on not only the barrier height but also the shape of the barrier. Under very high electric fields as in our experiment, only triangular barrier is of interest:

$$\begin{aligned} x_1 &= 0 \\ x_2 &= \frac{\phi_B}{qF} \\ E_C(x) &= E_F + \phi_B - qFx \end{aligned} \tag{6.15}$$

and hence

$$J = \frac{A^* T^2 \pi \exp(-2\alpha\phi_B^{3/2}/3qF)}{(\alpha\phi_B^{1/2} kT/qF)\sin(\pi\alpha\phi_B^{1/2} kT/qF)} \tag{6.16}$$

where

$$\alpha = \frac{4\pi(2m^*)^{1/2}}{h} \tag{6.17}$$

and A^* is the Richardson constant.

Charge injection modified by bulk transportation

In the above discussion of charge injection, the formulas for injection currents due to Schottky emission and field emission were originally derived for semiconductors where the mean free path of carriers is large. It has been argued that for solids with small mean free paths such as dielectric polymers, these formulas are not

strictly correct. For instance, a modified formula for Schottky emission has been suggested by Simmons [72]:

$$J = 2q(\frac{2\pi mkT}{h^2})^{3/2}\mu F \exp(-\frac{\phi_B}{kT}) \exp(\beta F^{1/2}) \tag{6.18}$$

where μ is the carrier mobility in bulk polymer. This formula takes into account the finite bulk transportation rate in solids. The exponential terms represents the effect of interfacial energy barrier which determines the number of carriers that are available for transportation in the polymer, while the mobility determines the rate of transportation of these carriers in polymer. Similar argument also hold for field emission with the only difference that the carriers are injected through tunneling rather than thermionic emission.

Specific issues with conduction in polymers

Disorders, localized states and hopping

The PVDF-CTFE copolymer is a semi-crystalline polymer where crystalline regions are surrounded by amorphous regions. The repeating units in the backbone of the polymer are connected with σ bonds that show small overlapping between the electron wave functions of adjacent repeating units. Furthermore, between different polymer chains there is only molecular forces and the overlapping of electron wave functions is expected to be even smaller. In this case, the energy band of the crystal will be very narrow. Furthermore, the chemical structure of the copolymer contains a lot of randomness and typically there are relatively large amount of physical and chemical defects in polymers. This means even the crystalline region will be considerably disordered. For narrow energy band with high level of disorder it is expected that significant amount of carriers will occupy localized states rather

than shared by the entire lattice [73, 74]. In other words, this means the mean free path of carrier transportation is on the same order of the dimension of repeating units. Therefore, even though there are also electronic bands in the polymer, a carriers cannot travel freely in these bands as in crystalline semiconductors but is localized at one site. It moves to another site via thermally activated hopping [74]. Hopping mobility is much lower than band conduction mobility and can be expressed as

$$\begin{aligned} \mu_{hop} &= \mu_0 \exp[-W/kT] \\ \mu_0 &= (1/6)\nu_{ph} q R^2/kT \end{aligned} \tag{6.19}$$

where W is the activation energy, ν_{ph} is phonon frequency, R is the distance of hopping, and q, k, T have their normal meanings. Hopping not only happens in electronic band but can also take place between traps.

At high electric fields the hopping mobility often depends on the electric field. Poole-Frankel (P-F) type of dependence is often observed [80, 81]:

$$\ln J \propto \sqrt{F} \tag{6.20}$$

It should be noted that P-F emission was originally derived for charge emission from traps but has been found to be also applicable to hopping conduction in organic semiconductors.

The exponential dependence has also been proposed [82],

$$J \propto \exp(\frac{qFl}{2kT}) \tag{6.21}$$

Mechanism	Field dependence
Schottky emission	$\ln J \sim \sqrt{F}$
Bulk modified Schottky	$\ln(J/\mu) \sim \sqrt{F}$
Field emission	$\ln J \sim -1/F$
Space charge limited	$J \sim F^m$
Hopping	$\ln J \sim \sqrt{F}$ or $\ln J \sim F$

Table 6.2. Mechanisms of charge transportation and their dependence on electric field.

where l is the distance of hopping. This type of dependence is suggested to be due to hopping of small polarons [82].

Traps near the electrode-polymer interface

In polymers, trap states near the electrode-polymer interface often have higher concentration and wider distribution of energy level comparing to those in bulk polymer (Figure 6.3). This could be due to various reasons, such as surface roughness and the damage of film surface during metallization. The carriers can be injected from electrodes into trap states rather than entering the LUMO(HOMO) of polymer. After moving away from the electrode the carriers hop into bulk states, which could be traps or band states and typically have much narrower energy distribution. Due to the wide distribution of trap level near the interface, the first hop from metal into polymer may not be the rate limiting step, and the conduction may be limited by the energy difference between the traps near the interface and bulk states [79]. In this case, the conduction cannot be simply treated as bulk limited or injection limited. It depends on the energy distribution of trap and bulk states as welll as the mobility of hopping conduction.

The different mechanisms of charge transportation as well as their dependence on electric field are summarized in Table 6.2.

6.3 Electrical conduction in P(VDF-CTFE) copolymer

The experimental results of electrical conduction in P(VDF-CTFE) copolymer films will be presented in this section. From the measured dependence of conduction current on various factors we attempt to understand the mechanism of the conduction based on the above discussion of conduction processes.

Methods

The copolymer used in this study is purchased from Solvay and contains 9 mol% of CTFE. According to the manufacturer, it is highly heterogeneous (similar to elastomeric nodules) [71]. It has been observed that the copolymer can be only partly dissolved in MEK and there is gel like solid remaining in the solution. This is consistent with the experimental results in Solvay's patent on the synthesis of the copolymer, which describes the heterogeneous copolymer as having a composite type of structure where small particles of homogeneous P(VDF-CTFE) copolymer are embedded in matrix of PVDF homopolymer [70]. The insoluble solid is due to the fact that only the PVDF-CTFE homogeneous copolymer can be dissolved by MEK while the PVDF homopolymer matrix cannot. In the following discussion we use "PVDF-CTFE" to denote the heterogeneous copolymer rather than the homogenous component.

Some properties of the P(VDF-CTFE) copolymer are summarized in Table 6.3. The data are obtained from [52].

There are generally three methods of film processing for the P(VDF-CTFE) copolymer, namely, solution cast (including spin coating), melt press, and extru-

Property	Value
Dielectric constant (1kHz)	13.5
Dielectric loss (1kHz)	0.02
Breakdown field	$\approx$ 600MV
Melting point	165°C
Young's modulus	450MPa

Table 6.3. Some properties of the P(VDF-CTFE) copolymer. The electrical and mechanical properties were measured at 23°C. [52].

sion. In the first method, polymer powders are dissolved in dimethylformamide (DMF) and the solution is directly cast on glass substrates and dried under 70°C in an oven. After completely cured the film can be peeled off from substrate. Spin coating was also used to fabricate ultrathin films and the details about these films will be presented in a separate section. In the second method, films were formed by melt-pressing the powder at 230°C followed by immediate quenching in ice water. In the last method, films were extruded. Solution cast and melt-press methods are suitable for fabricating films with small quantity of polymer powders while the extrusion method requires in general large quantity of polymer resins (a few kgs). Among the three methods, experimental results show that the extruded films exhibited the best quality in terms of the breakdown field and conduction loss, and are also easier for the subsequent uniaxial stretching, which further improves the film breakdown strength. A zone drawing machine was used to uniaxially stretch the P(VDF-CTFE) films to five times of their original length with the temperature of the narrow heating zone at 100°C. The zone drawing machine provides a very narrow heating zone with the drawing ratio to be controlled precisely by the differential speed of the two motors at the two ends of the thin film to be stretched.

The films discussed in this section were all extruded and zone-stretched as described above. Typical thickness of film is around 10μm. The films were annealed at 80°C for 1hr and then at 130°C for 4hrs to increase the crystallinity. Electrodes

had round shape were sputtered (Au, Ag) or thermally evaporated (Al) onto both surfaces of the polymer. In the following discussion, if not specified the electrode material is silver.

D-E loop, current-time (I-t), and current-voltage (I-V) characteristics of the copolymer have been measured. D-E loop was recorded using a modified Sawyer-Tower circuit in Pennstate Materials Research Lab. The I-t and I-V curves were recorded by Keithley 6517 electrometer controlled using a Labview program. In I-t measurements, DC voltages were applied and the current were recorded every certain time. In I-V measurements, for each voltage a DC voltage was first applied for 5 seconds and then the current reading is recorded, and then the samples were shorted for 30 seconds before continuing to the next voltage. All of the above measurements were performed under room temperature unless specified. The diameter of all electrodes is 2cm. Other details of the measurements will be specified along with the corresponding measurement results.

Results of conduction current measurements

J-t curves

The measured J-t curves of P(VDF-CTFE) films coated with types of different metal electrodes are plotted in Figure 6.5. In charging measurement (denoted by "charge" in the figure) virgin samples were subjected to 50MV/m DC field. In discharging measurement (denoted by "discharge") the field is decreased to zero (short circuit) right after the charging measurement and the J-t curve is recorded. The discharging current is in opposite direction to charging current and its magnitude is shown in the figure.

A general trend for all the J-t curves shown in Figure 6.5 is that all the currents

decrease with time. The J-t curves are nearly linear except for some turning points. A linear curve on log-log plot suggests the J-t relationship of

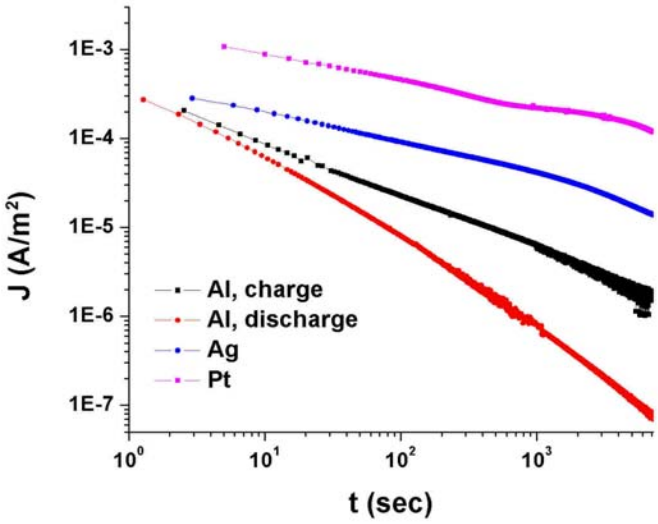

Figure 6.5. J-t curves of P(VDF-CTFE) films under 23°C and 50MV/m electric field.

$$J \propto t^{-n} \tag{6.22}$$

where n is a constant. This is a universal phenomena that has been widely observed in many dielectric materials. This type of relationship could be caused by dielectric relaxation with a broad distribution of relaxation times [76]; it could also be due to the slowly build-up of space charge and trap filling [77].

The current shows dependence on electrode material. Aluminum electrode resulted in the smallest current density while platinum electrode showed the largest. Similar trend has also been observed in P(VDF-TrFE-CFE) terpolymer (see Chapter 5). Furthermore, the charging and discharging currents of the same sample are significantly different. At the beginning, the two currents have almost the same magnitude, but the charging current decays much slower than the discharging

current. If the observed J-t relationship (equation (6.22)) is completely due to distribution of dielectric relaxation time, we would expect that the slope of J-t curves in charging and discharging measurements should be the same, which contradicts the experimental result [76]. Therefore, it is believed that the decay of current is not only due to dielectric relaxation and conduction is also involved.

The measured J-t curves under different DC electric fields and temperatures are shown in Figure 6.6. Similar to Figure 6.5, roughly speaking all the J-t curves consist of segments of straight lines connected at some turning points, which are indicated by arrows in the figures. The existence of turning points is due to the depletion of certain source of conduction, such as available trap states. It can be found that these turning points move to shorter time at higher temperatures and electric fields.

J-V curves

The measured J-V curves of the P(VDF-CTFE) films are shown in Figure 6.7. The curves can be roughly divided into three regions (Figure 6.7a). At low field (below 80MV/m) the J-V relationship is nearly linear. Under intermediate fields (80MV/m to 250MV/m) there is a peak in current density which is followed by a negative resistivity region where current density decreases with electric field. At higher fields (>250MV/m) the current increases rapidly with field. The low field J-V curves under different temperatures are shown in Figure 6.7b. Comparing the J-V curves and J-t curves it is found that the turning points in J-t curves corresponds well to the current peaks J-V curves. Therefore, it is very likely that they are due to the same underlying mechanism.

Tu et al suggested that the current peak and negative resistivity in J-V curves of polymers are due to the filling of traps near the surface of polymer [55]. Basically,

at the beginning of measurement the carriers are injected from electrode into the trap states in the polymer near the surface. Due to the wide distribution of energy, this process should be relatively easy. The filled traps form a homocharge layer and reduces the electric field near the surface, which causes the gradual decay of current in J-t curves. At certain field or time the available surface traps are almost filled and hence further injection must involve hopping into bulk states, which rate is expected to be much lower comparing to injection into surface traps. Both the decrease of field and depletion of traps could result in the current peak and negative resistivity.

The rapid increase of current at higher fields ($>$ 250MV/m) can be due to several different mechanisms, such as Schottky emission (lnJ$\sim \sqrt{F}$), field emission (lnJ$\sim -1/F$), Poole-Frankel emission (lnJ$\sim \sqrt{F}$), or hopping of small polarons (lnJ$\sim F$). It was found that the J-V curve between 300MV/m and 400MV/m can be best fitted by the small polaron hopping formula (equation (6.21)) (Figure 6.8):

$$J \propto \exp(\frac{qFl}{2kT}) \tag{6.23}$$

The fitting gives l=0.43nm, which roughly corresponds to the inter chain spacing in PVDF. Since the chains in stretched PVDF films generally orient along the stretching direction, the transport of carrier (small polarons) along the film thickness direction involves hopping between paralleled chains. Therefore, this hopping distance is a reasonable value.

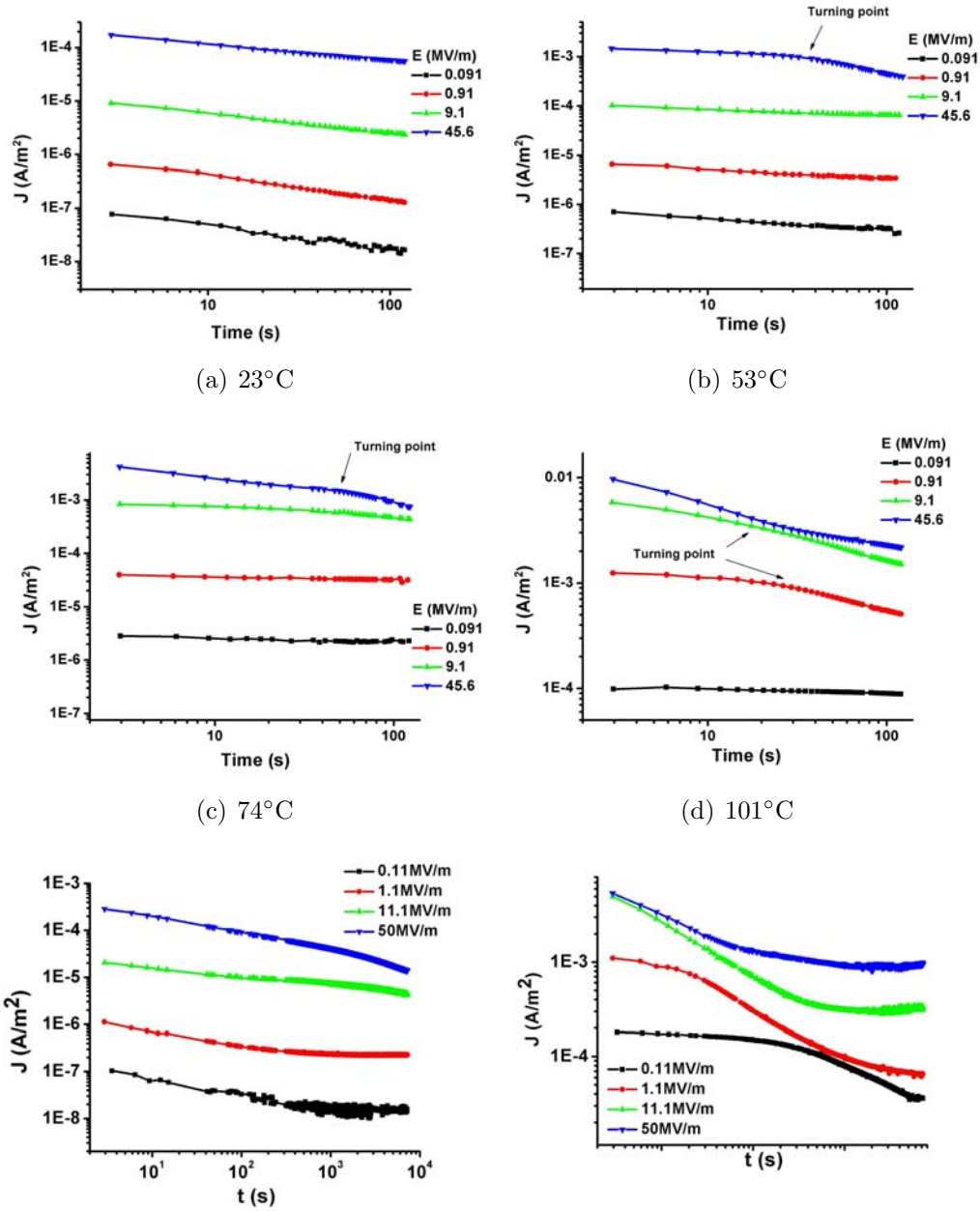

(a) 23°C (b) 53°C

(c) 74°C (d) 101°C

(e) 23°C, longer time (f) 100°C, longer time

Figure 6.6. The measured J-t curves of P(VDF-CTFE) films under different temperatures and electric fields.

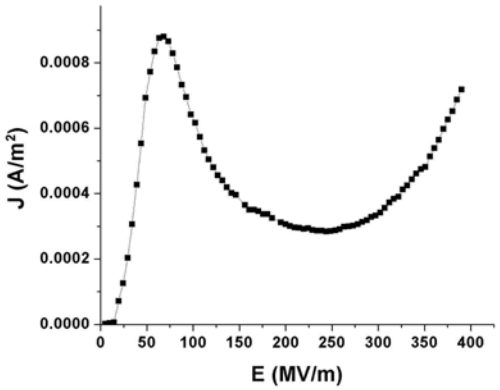

(a) Entire field range

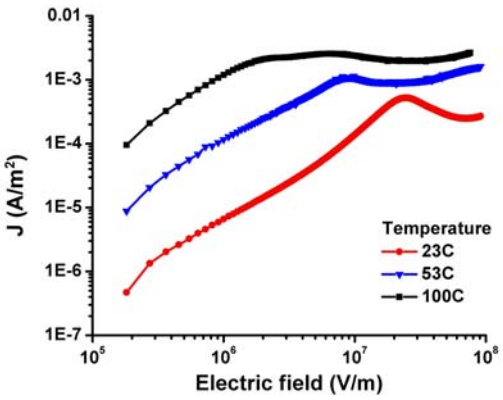

(b) Lower fields

Figure 6.7. The measured J-V curve of P(VDF-CTFE) films.

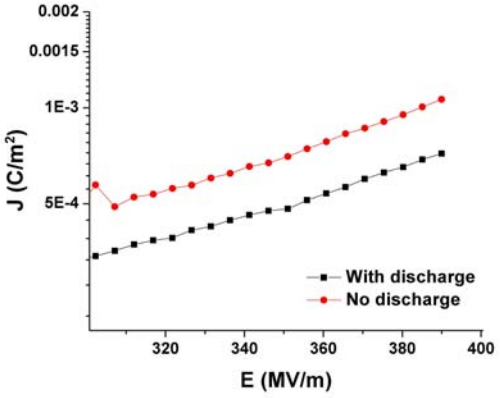

Figure 6.8. High field portion of J-V curve fitted with small polaron hopping formula.

Conclusions on electrical conduction in P(VDF-CTFE) copolymer

The dependence of conduction current on the type of metal electrode strongly suggests that the conduction is controlled by charge injection from electrodes. The interfacial energy barrier as well as the morphology of the interface (e.g. existence of interfacial layer) affect the injection current. Furthermore, the existence of current peak and negative resistivity also suggest charge injection controlled conduction where the traps near the interface play an important role in the conduction. However, the exponential type of J-V curve at high fields is most likely due to the field dependence of hopping mobility, which is the characteristic of bulk transportation. Therefore, we conclude that in the P(VDF-CTFE) copolymer the conduction is mainly controlled by charge injection from electrode, but the current density of charge injection is affected by the mobility of carriers in the polymer. This is similar to the bulk modified charge injection model proposed by Simmons [72].

6.4 Reducing the conduction loss in P(VDF-CTFE) copolymer by using blocking layers

Since the conducting carriers in P(VDF-CTFE) is supplied by the electrodes through charge injection at the interfaces, an effective approach to reduce the conduction loss is to block the charge injection. For instance, this can be realized by inserting a blocking layer between P(VDF-CTFE) and the electrode (Figure 6.9). This blocking layer must have very small leakage and high breakdown electric field. Furthermore, the process for fabricating the blocking layer must be compatible with

P(VDF-CTFE) so that the two films can be integrated together. In film capacitor applications, certainly all-polymer films are the most ideal choice. Many non-polar polymers have very small leakage current and high breakdown strength, such as polypropylene, polyethylene, polystyrene, and poly(2,6-dimethyl-1,4-phenylene oxide) (PPO). Polymer thin films can be deposited using various methods, such as spin coating, chemical vapor deposition and physical vapor deposition (e.g. sputtering and thermal evaporation). In addition, multilayered polymer films can be fabricated using co-extrusion method. With the currently available equipment, spin coating has been selected as the deposition method. In order to successively spin coat the individual layers in a multilayer, it is required that the solvent used for P(VDF-CTFE) (or blocking layer) does not dissolve the blocking layer (or P(VDF-CTFE)). Table 6.4 summarizes the solvents, non-solvents as well as dielectric properties of selected polymers. In terms of solvents, polystyrene, polypropylene, and poly(2,6-dimethyl-1,4-phenylene oxide) (PPO) are possible candidates. However, although acetone can dissolve P(VDF-CTFE), it is too evaporative and when used in spin coating it does not yield good film quality. Therefore, polystyrene cannot be used since it requires acetone as the solvent for P(VDF-CTFE) in spin coating. On the other hand, polypropylene has very poor adhesion to P(VDF-CTFE) and the fabricated multilayers are very easy to delaminate. PPO is soluble in toluene and cannot be dissolved by DMF, and toluene does not dissolve P(VDF-CTFE). Therefore, PPO has been selected as the blocking layer with toluene and DMF used as solvents for PPO and P(VDF-CTFE) in spin coating.

A drawback of using polymer as blocking layer is that the non-polar polymers with ultra small leakage current also exhibit low dielectric constant (<3). This reduces the overall dielectric constant of the multilayer film and results in very high electric field in blocking layers which increases the conduction. On the other

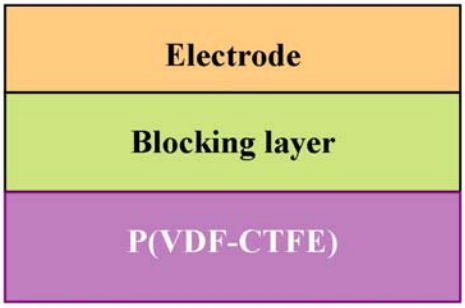

Figure 6.9. The schematic view of blocking layer inserted between electrode and P(VDF-CTFE) film.

Polymer	K (1kHz)	D (1kHz)	Solvents	Non-solvents
CT	13	0.02	Acetone, DMF, NMP	toluene
PS	2.5	<0.001	toluene, MEK, DMF	acetone, alcohols
PMMA	3	0.055	chloroform, MEK, DMF	Aliphatic hydrocarbons
PC	2.9	0.005	chloroform,dioxane DMF	hydrocarbons
PPO	2.7 (1MHz)	0.005	toluene	acetone, MEK, DMF
PP (a)	2.2-2.6	0.0005	benzene, toluene	Most polar solvents
PEI	3.1 (1MHz)	0.0013	DMF, NMP	Acetone

Table 6.4. Dielectric properties and solvents/nonsolvents of selected polymers. Source: [86]. CT: PVDF-CTFE; PS: polystyrene; PMMA: poly(methyl methacrylate); PC: polycarbonate; PPO: poly(2,6-dimethyl-1,4-phenylene oxide); PP (a): polypropylene, atactic; PEI: polyetherimide.

hand, inorganic materials with dielectric constants close to or higher than P(VDF-CTFE) and with very low conduction loss are widely available. The properties of some inorganic blocking materials are listed in Table 6.5. The inorganic dielectric films are usually deposited by vapor phase deposition, such as sputtering, evaporation and chemical vapor deposition (CVD). The melting temperature of P(VDF-CTFE) is 165°C and hence the deposition temperature of blocking layer must be considerably lower than this value. Furthermore, it was found that thin film of P(VDF-CTFE) can be easily damaged by plasma during sputtering. Plasma enhanced chemical vapor deposition (PECVD) provides a method to deposit high quality dielectric films at low temperature with moderate plasma energy. For instance, high quality silicon nitride (Si_3N_4) (dielectric constant K=7) films can be

Material	Method	K	J (A/m^2)
Al_2O_3	ALD	9	5×10^{-3} [90]
SiO_2	oxidation	3.9	10^4 [91]
Si_3N_4	PECVD	7	1 [89]
Ta_2O_5	CVD	26	10^{-6} [92]
TiO_2	CVD	81	10^{-4} [93]
HfO_2	sputtering	25	0.1 [94]
ZrO_2	sputtering	25	0.01 [95]

Table 6.5. Dielectric constant and leakage current for selected inorganic blocking materials. All the currents are for electric fields that are equivalent to 300MV/m in P(VDF-CTFE).

deposited at as low as about 125°C. In this study, PECVD Si_3N_4 blocking layers and Si_3N_4/P(VDF-CTFE) multilayers have been investigated.

In the following part of this section, the experimental methods and results of the reduction of conduction current using blocking layers will be presented. Both all-polymer and inorganic/polymer multilayers have achieved markedly improved efficiency comparing to P(VDF-CTFE) single film. I will also demonstrate that field emission (tunneling) into blocking layers which causes large conduction current is a major factor that limits the highest operation electric field of the multilayers.

Method for fabricating multilayered films containing blocking layers

The fabrication the multilayered film started with a silicon wafer. A metal layer was first deposited on silicon wafer to form the bottom electrode. The individual layers in the multilayer were then deposited successively by spin coating or PECVD. Finally, top electrode is deposited on the multilayered film.

Top and bottom electrodes

In all the experiments described in this section aluminum coated silicon wafers have been used as the substrate. Aluminum was selected due to its excellence adhesion to silicon. Before aluminum deposition, the silicon wafers were first immersed in acetone and cleaned by ultrasound for 30min, followed by dipping in boiling 1:1 acetone/ethanol mixture for at least fifteen minutes. After each of the steps the wafer was rinsed by DI water and dried by nitrogen gas. Aluminum is then thermal-evaporated on silicon under base pressure of less than 10^{-6} torr with typical rate of 0.2nm/sec. The aluminum is at least 100nm to ensure a good electrical conductivity. Top electrodes of the films are also aluminum and were deposited using the same process as for bottom electrode except that the deposition rate is 0.05nm/sec and the final thickness is 50nm. The bottom electrode covers the entire silicon wafer while the top electrodes are circles with diameter of 0.84mm. The top electrodes were defined by a shadow mask.

Deposition of polymer layer

Alternative multilayer of PVDF-CTFE and PPO is fabricated by successively spin coating of individual layers with DMF and toluene as solvents, respectively. Solution concentration between 1% and 6% and spin rate of 1000RPM to 8000RPM have been used for both polymers. The thickness of individual layer was controlled by varying the concentration or spin rate. After coating each layer the sample was placed in vacuum oven under 120°C for at least 10 hours to remove residual solvent.

Deposition of silicon nitride

Chemical vapor deposition (CVD) has been used to deposit silicon nitride for long time [87]. The fundamental process of formation of silicon nitride is the oxidation of silane (e.g. SiH_4) by nitrogen containing compounds such as NH_3, N_2 and N_2O. However, such reaction happens only at high temperatures (e.g. 700°C) [88]. Low temperature CVD can be achieved by plasma enhanced CVD (PECVD) where the kinetic energy of fast electrons in the plasma takes the place of thermal energy in the activation of desired CVD reactions. The dielectric properties of the nitride film depend strongly on the deposition conditions [87]. Usually a large excess of oxidant is used in the deposition and the key process factor is the ratio between plasma power and the supply rate of silane. If the amount of activated oxidant is not enough, the resulting film will contain large amount of excess Si and Si-H bonds which causes high loss. In addition, NH_3 has much higher efficiency in oxidizing silane as compared to N_2. It was reported that nitride deposited from N_2 is electrically leaky due to porous microstructure even when deposited using excess activated oxidant. On the other hand, films deposited from NH_3 is nonporous and with excess oxidant very good dielectric property can be achieved. The better efficiency of NH_3 was attributed to the formation of precursors, such as $Si(NH_2)_3$ and $Si(NH_2)_4$. On the other hand, plasma power or flow rate that is too high can lead to particle formation.

It has been reported that trap assisted conduction is the major conduction process in silicon nitride and Poole-Frankel (P-F) type of J-V relationship was often observed [96]. More recently, it was found that in Si-rich nitride films conduction is dominated by traps, while in stoichiometric samples trap controlled current is only observed in an intermediate field range and field emission (F-N tunneling)

dominates at high fields [89]. On the other hand, in oxynitride films which has the lowest trap density only low field ohmic conduction and high field tunneling can be observed. One set of suggested process conditions are that under 500°C, 10^{-3} to 10^{-4} Torr deposition pressure, and plasma power of 250W, flow rate ratio of SiH_4:N_2=0.133 yields Si-rich films and 0.0125 yields stoichiometric films, and oxynitride can be obtained by introducing O_2 during deposition [89]. Another researcher suggested that at between 200°C and 300°C the approximately minimum ratios of oxidant flow to SiH_4 is 125 for N_2O, 25 for NH_3, and 40 for N_2 [87]. It should be noted that the optimum flow rate depends on the temperature, power, and even other detailed configurations of the deposition equipment. Therefore, it is critical to search for an optimized condition for a specific deposition process. The above data serve as good starting points of the search.

In this study, silicon nitride has been deposited using a cluster tool (Applied Materials P5000). Silane (SiH_4), nitrogen and ammonia have been used as the source gases and the flow rates varies. The distance between the gas source and wafer was 400mil and the plasma power was 300W. The deposition pressure was 3.5 torr. The temperature of source gas was 150°C and wafer temperature was about 120°C to 130°C.

Comments on the maximum number of layer in the multilayered films

The maximum number of layers achievable in PPO/P(VDF-CTFE) multilayer is three. When depositing more than three layers the film becomes non-uniform and large number of defects were observed. It was found that such degradation of quality was due to the re-dissolving of deposited layers. It is the self dissolving (i.e. P(VDF-CTFE) dissolved by DMF or PPO dissolved by toluene) rather than inter-dissolving (i.e. toluene damages P(VDF-CTFE) or DMF damages PPO) that

is the main cause of problem. This is supported by the fact that when a single P(VDF-CTFE) (or PPO) layer is subjected to toluene (or DMF) no damage of the film could be found. On the other hand, the multilayers with poor qualities always have at least three layers. We expect that self-dissolving is caused by the permeation of solvent through the top layer which caused the underlying layer to be subjected to the solvent which can easily dissolve it. The permeability of polymer to small molecules is highest for amorphous polymers in rubbery state. Therefore, it is expect that P(VDF-CTFE) is easier to be penetrated due to its low glass transition temperature (about -30°C) as compared to PPO (> 200°C). Based on this consideration, highly crystalline polymers that are deposited from vapor phase such as parylene will prevent the self-dissolving problem. However, ultra-tin parylene films (<100nm) deposited by available equipment show much poorer properties comparing to PPO and hence were not used in the study. Nevertheless, baking the spin coated films under vacuum and high temperature can guarantee good film quality up to three layers which is sufficient for current study.

In the fabrication of Si_3N_4 multilayer, it was found that P(VDF-CTFE) could not be spin coated on Si_3N_4 because the solution did not wet the surface of Si_3N_4 film. Therefore, only bilayers with P(VDF-CTFE) at the bottom and Si_3N_4 at the top have been studied.

Methods of measurements

After the deposition of polymer and metal layers small portions of film near corners or edges of the wafers were removed by acetone or toluene (depends on which polymer is at bottom) to expose part of the bottom electrode for electrical contact. The thickness of films was measured using a surface profilometer (Tencor Alpha-Step 500). The thickness of single layers were also measured using an ellipsometer

to calibrate the profilometer measurement.

The electrical contact to the samples was provided by two probes that touch the top and bottom electrodes. The probe for the bottom contact has a conventional sharp tip. The tip of the probe for top contact has been replaced by a U-shaped thin metal wire (Figure 6.10a). The round bottom of metal wire provides a much softer and flatter contact as compared to the sharp tips and hence prevents the damage of polymer films. A test setup has been developed for D-E loop measurement (Figure 6.10b). The waveform is generated by a function generator and then amplified by a high voltage amplifier. Unless otherwise specified, single burst of unipolar triangular wave with total duration of 10msec was used in loop measurements. An oscilloscope probe (10:1 ratio) has been added to the reference channel to increase the input impedance of the oscilloscope.

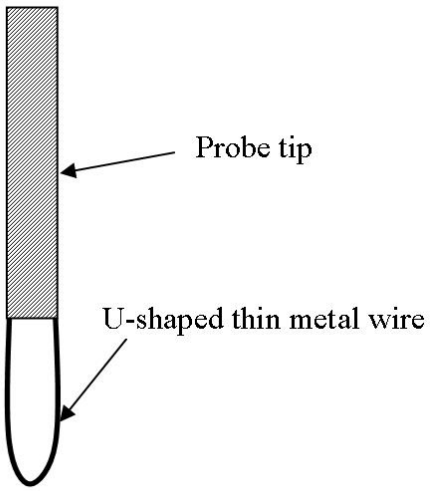

(a) The metal wire contact

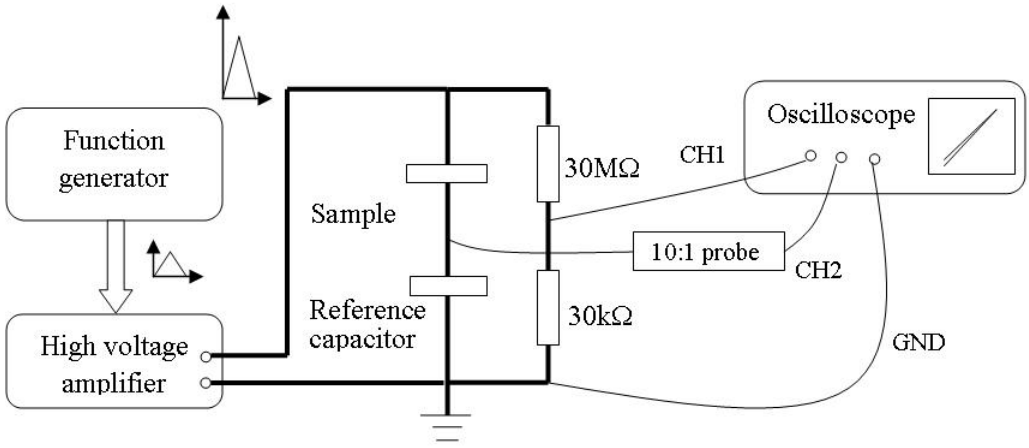

(b) The test setup for D-E loop measurement

Figure 6.10. (a) The metal wire contact used for top electrodes and (b) A schematic view of the test setup for D-E loop measurement.

Experimental results

Single layered films

The D-E loop of P(VDF-CTFE) single layer is shown in Figure 6.11a. The film thickness is 120nm. The films typically broke down between 200MV/m and 300MV/m, which is significantly lower than in extruded films where breakdown field of higher than 600MV/m can be routinely achieved. Furthermore, the conduction loss in spin coated film is much larger than extruded films. It is believed that the large conduction loss and low breakdown field is due to existence of conducting channels in spin coated films. The conduction channels could be pinholes or the boundary between crystalline and amorphous regions. Large spherulite shaped crystalline regions with sizes on the order of 10μm has been observed in P(VDF-CTFE) films cast from solution. The thickness of spin coated film is less than 500nm and hence one single spherulite may extend from one electrode to the other. In inorganic films it was proposed that the grain boundaries are one of the major cause of large leakage currents [85]. Therefore, it is also possible that these boundaries in the polymer could contribute significantly to conduction.

Other phenomena observed in the spin coated P(VDF-CTFE) film are pre-breakdown and self-healing. When the as-deposited film was first subjected to electric field the conduction loss was very large and breakdown often happened at very low voltage. However, after these breakdown events the film could still withstand high voltage and the conduction loss was significantly reduced. In general a series of such pre-breakdown happened at successively higher voltages until the film finally permanently break down.

The D-E loop of sandwiched P(VDF-CTFE) film with a 5nm aluminum interlayer embedded in the polymer is shown in Figure 6.11b. The breakdown field of

aluminum embedded film is much higher than pure P(VDF-CTFE) films, while the shape of loop and conduction loss of the two kinds of films are essentially the same. When a thin layer of aluminum is embedded in the polymer, it efficiently blocks the breakdown path by simple physical blocking and/or by homogenizing the charge in the breakdown channel. However, the aluminum layer does not block charge transportation and hence did not affect the conduction behavior of the film.

The time dependence of the remnant displacement in D-E loops of spin coated P(VDF-CTFE) films was also measured (Figure 6.12a). From the time dependence of loss at different electric field we can extract the conduction and dielectric energy losses from the slope and the intercept with D axis in D_r-t curves (Figure 6.12b). The leakage current density is about $0.6A/m^2$ under 400MV/m, which is more than one order of magnitude higher comparing to extruded films.

The D-E loop of spin coated PPO is shown in Figure 6.13. The thickness of film is 300nm. Linear response was maintained up to the highest field of about 900MV/m and the dielectric constant as determined from the slope of loop is 2.75. D-E loop of PECVD silicon nitride film is shown in Figure 6.14. The thicknesses of films are all 300nm. As was mentioned earlier, the electrical properties of silicon nitride depends on the deposition conditions. For instance, when the flow rates of NH_3, N_2 and SiH_4 are 100, 2000 and 75 sccm (standard cubic centimeter per minute) the film is very lossy (Figure 6.14a). If the flow rate of SiH_4 is reduced to 45 sccm the leakage current is very small (Figure 6.14b). In fact, under the same flow rates of NH_3 and N_2 and when the flow rate of SiH_4 is between 35 and 55 sccm, highly insulating films with leakage current and breakdown fields similar to the 45 sccm film can be obtained. Under these conditions the deposition rate is about 7-8nm/sec. The dielectric constant as determined from the loop is k=7.1. Similar to PPO, the dielectric response is linear up to at least 650MV/m.

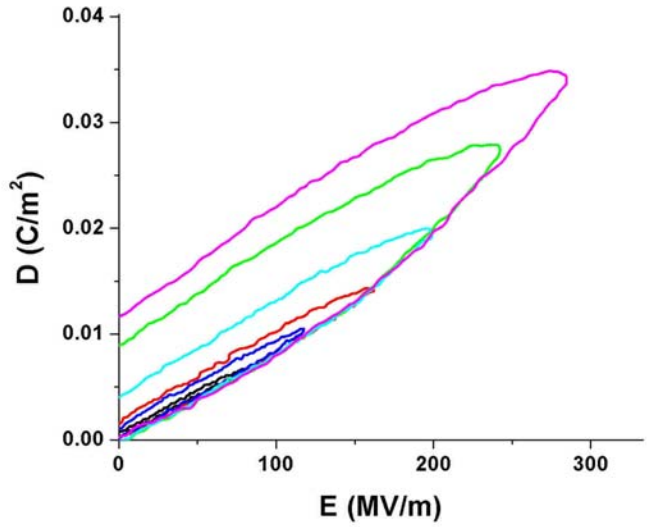

(a) Without Al

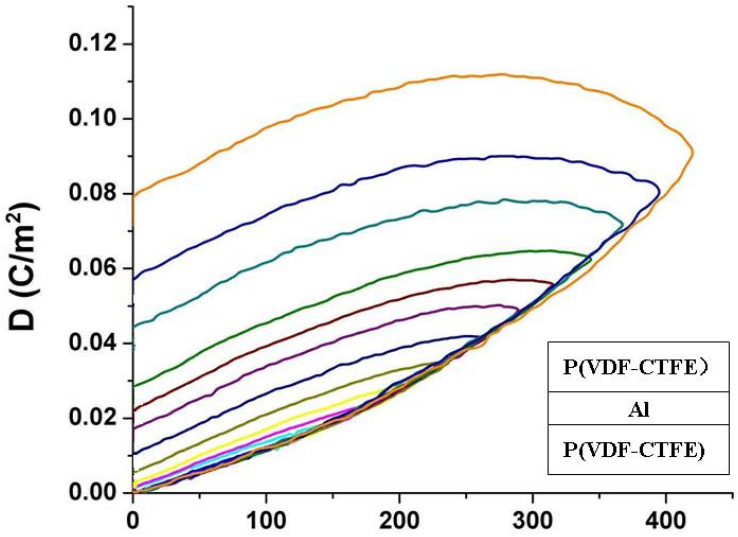

(b) With Al

Figure 6.11. The D-E loops of spin coated P(VDF-CTFE) films with and without embedded Al interlayer. The inset in (b) illustrates P(VDF-CTFE) film with embedded Al.

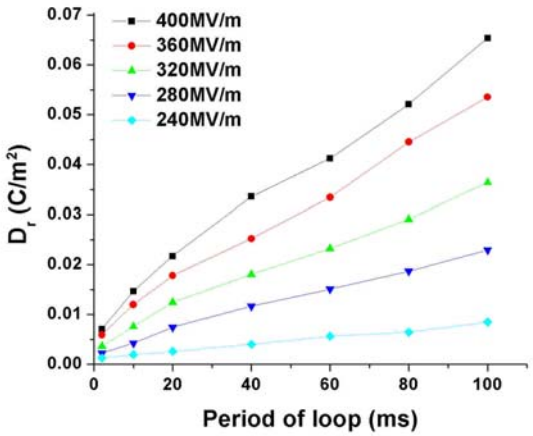

(a)

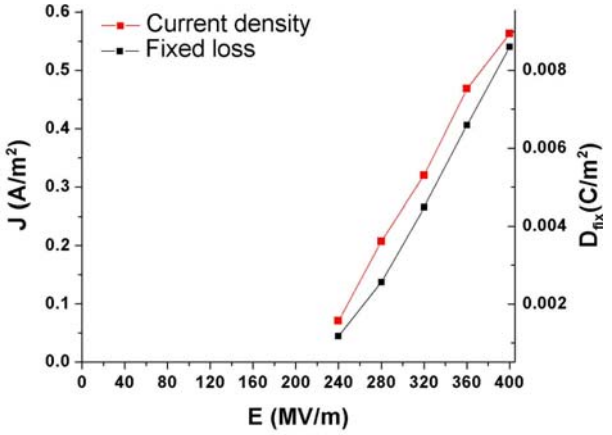

(b)

Figure 6.12. (a) The time dependence of remnant displacement of spin coated P(VDF-CTFE) film with different maximum fields in D-E loop; (b) Conduction current and dielectric energy loss extracted from the time dependence of remnant displacement.

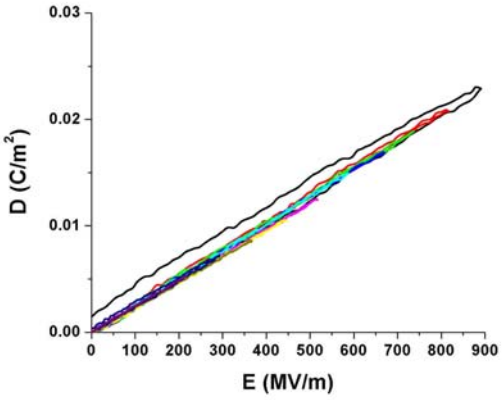

Figure 6.13. The D-E loop of spin coated PPO film.

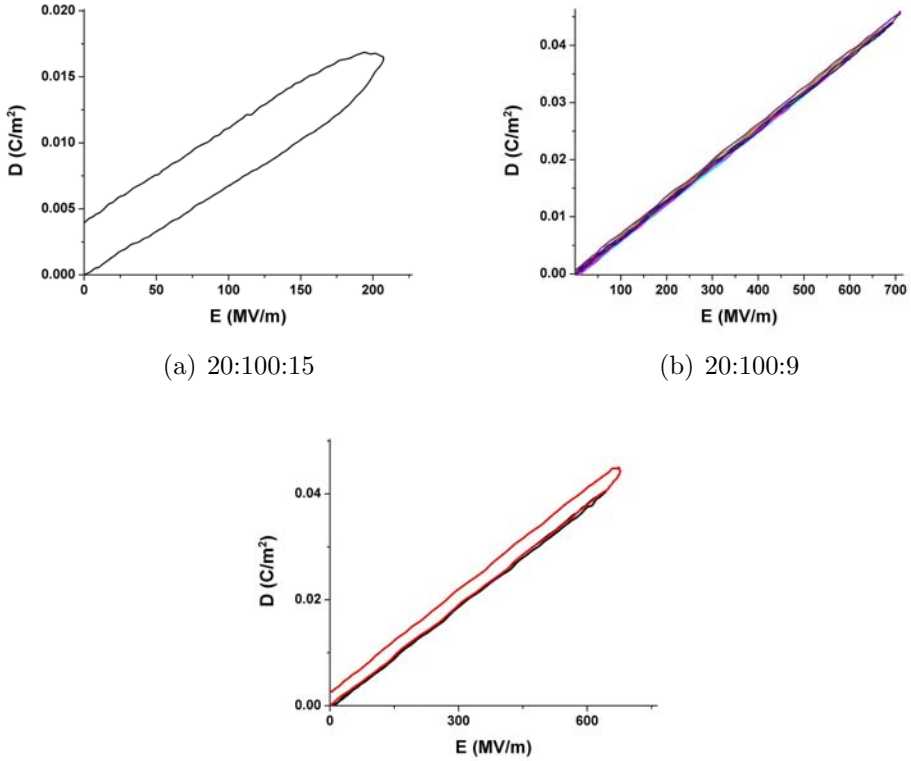

(a) 20:100:15

(b) 20:100:9

(c) 20:100:9, loop time 0.1sec

Figure 6.14. The D-E loops of pure Si_3N_4 films under different deposition conditions and loop times.

Comparing to single P(VDF-CTFE) films, the behavior of the loss in D-E loops of PPO and silicon nitride films is significantly different. For instance, in PPO very low loss is maintained up to a high electric field (800MV/m) and then the loss suddenly increases with only a small increase of electric field (i.e. to 900MV/m). Similarly, in silicon nitride very low loss is maintained up to about 650MV/m but dramatically increases when field is increased to 680MV/m. The rapid increase of loss happens at lower field if the time of loop is increased to 10 times (Figure 6.14b,c), which indicates that the loss is due to conduction current. On the other hand, in P(VDF-CTFE) considerable loss exist even at low fields and the loss increases gradually with electric field.

The rapid increase of conduction loss in PPO and high quality silicon nitride films at high electric field is most likely due to tunneling. In general there are two types of tunneling, namely, Fowler-Nordheim (F-N) tunneling which involves tunneling through the injection energy barrier, and direct tunneling where the carrier directly tunnels from one electrode to the other (Figure 6.15). The films under study are thicker than 100nm and typical barrier height is less than 3eV. An electric field of 500MV/m will produce voltage drop of 3V in only 6nm which is much smaller than film thickness. Therefore, only F-N tunneling will be considered here. The tunneling current is given by equation (6.16) and is rewritten as

$$J = \frac{A^* T^2 \pi \exp(-2\alpha\phi_B^{3/2}/3qF)}{(\alpha\phi_B^{1/2} kT/qF)\sin(\pi\alpha\phi_B^{1/2} kT/qF)} \tag{6.24}$$

and the barrier height is reduced due to image force:

$$\phi_B' = \phi_B - \Delta\phi = \phi_B - \sqrt{\frac{qF}{4\pi\epsilon}} \tag{6.25}$$

Assume that there is no surface states which modify the barrier height, the bar-

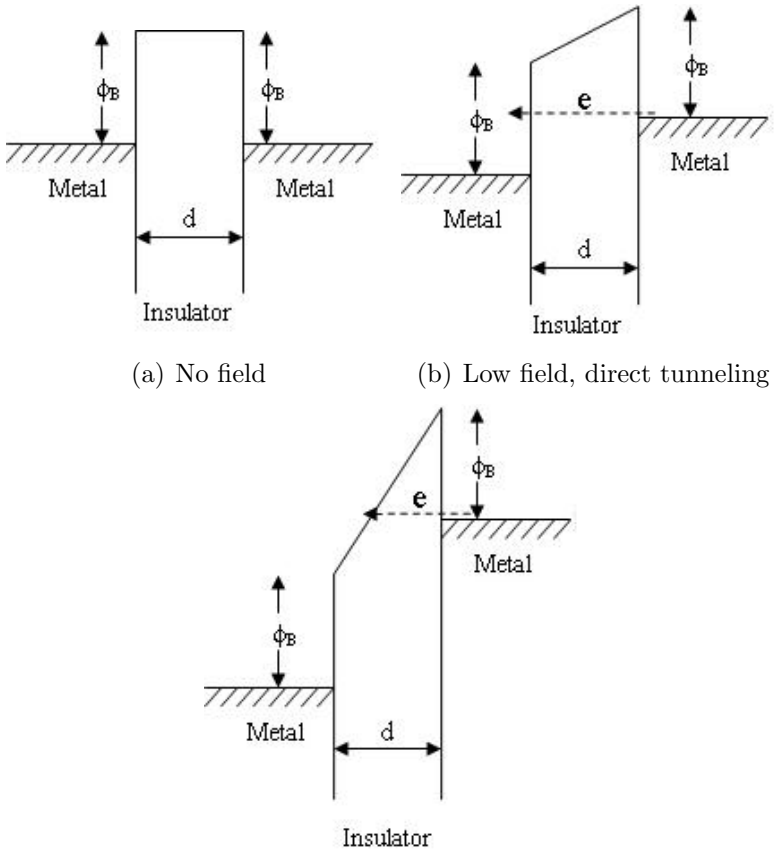

(a) No field (b) Low field, direct tunneling

(c) High field, F-N tunneling

Figure 6.15. Tunneling in metal-insulator-metal structures.

rier height between silicon nitride and aluminum is 2.2eV and 2.9eV for electrons and holes, respectively [10]. The calculated current densities are shown in Figure 6.16. From the measured D-E loop of silicon nitride film (Figure 6.14b) the conduction currents at 645MV/m and 675MV/m are estimated to be 0 and 0.5A/m^2, respectively. Calculation of tunneling current density indicates that current density of 0.5A/m^2 (for electrons) is achieved at 676MV/m, which is in very good agreement with D-E loop. The data for band edge of PPO is currently unavailable. From measured D-E loop the conduction currents of PPO under 815MV/m and 890MV/m are 0 and 0.33A/m^2, respectively. From the calculation of tunneling current the barrier height is estimated to be 2.8eV.

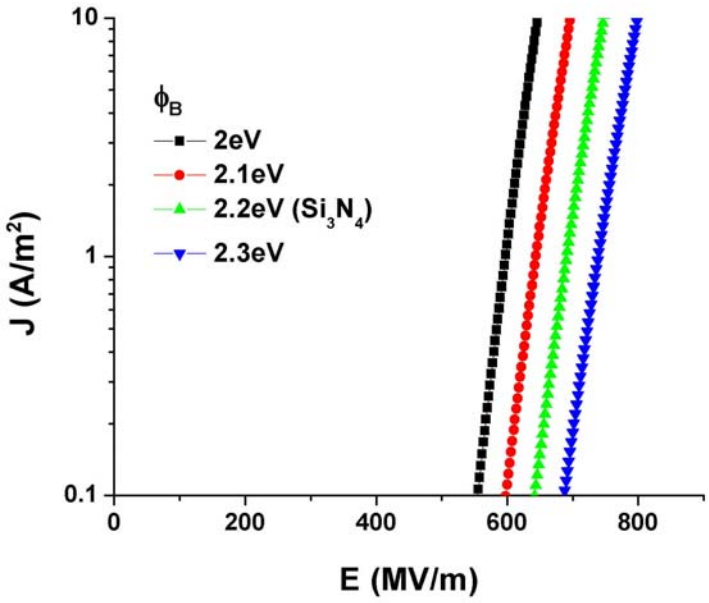

Figure 6.16. Calculated F-N tunneling current density of Si_3N_4.

PPO/P(VDF-CTFE) mulilayers

The D-E loops of two PPO/P(VDF-CTFE) multilayers are shown in Figure 6.17. Both of the two multilayers contain three individial layers. In the "OCO" film, both the top and bottom layers are PPO and the middle layer is P(VDF-CTFE). In the "COC" film, the top and bottom layers are P(VDF-CTFE) while the middle layer is PPO. The two films exhibit similar dielectric constants and the ratio between thicknesses of P(VDF-CTFE) and PPO in both films is about 2:1. The overall thickness of the OCO and COC films are 220nm and 380nm, respectively.

In the D-E loops of both OCO and COC films, the loss is negligible at low electric fields and increases significantly when the electric field is larger than certain value. In both films the increase of loss happened when the electric displacement is about $0.02 C/m^2$. Comparing to Figure 6.13, it can be found that this displacement corresponds to the field under which the conduction loss in PPO significantly

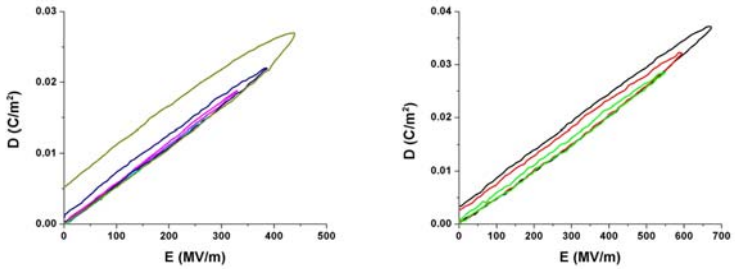

(a) OCO, k=6.2 (b) COC, k=5.5

Figure 6.17. The D-E loops of OCO and COC types of P(VDF-CTFE)/PPO films.

increases. Therefore, the increase of loss in the multilayeres is most probably due to the onset of tunneling in PPO.

At displacement of 0.02C/m^2, in P(VDF-CTFE) single films the remnant displacement is around 0.005, while in the multilayered films it is almost zero. Therefore, before the onset of tunneling the PPO did function as a perfect blocking layer.

Ideally, the OCO structure should exhibit the lowest conduction loss since the charge injection is completely by the PPO layers. However, the D-E loops show that at high electric fields the increase of conduction loss in OCO film is much faster than in COC film. For instance, at 440MV/m the remnant displacement in OCO film is 18.5% of the maximum displacement in the D-E loop. In COC film, at 672MV/m the remnant displacement is only 8.4% of maximum displacement. This is because in OCO film the PPO films are adjacent to metal electrodes and large electric field in PPO will readily generate very large tunneling current. On the other hand, in COC film the PPO layer is sandwiched by P(VDF-CTFE) films. In this case, the available carriers to be tunneled into PPO are the charge carriers in P(VDF-CTFE), which concentration is much smaller than electrons in metal and hence the tunneling current is expected to be much smaller.

Si_3N_4/P(VDF-CTFE) bilayer

The D-E loop of Si_3N_4/P(VDF-CTFE) bilayer with silicon nitride on the top is shown in Figure 6.18. The thickness of film is 300nm. The dielectric constant of the bilayer is 10.6. The loss increases gradually with electric field up to about 450MV/m and D$\sim$0.045. This corresponds to the highest displacement achieved in single layered silicon nitride films (Figure 6.14b). Comparing to single layered P(VDF-CTFE), again significant reduction of conduction loss can be observed. For instance, at displacement of D=0.04C/m^2, the remnant displacement in single layered P(VDF-CTFE) is more than 25% of maximum displacement, while in the bilayer it is only 6.2%.

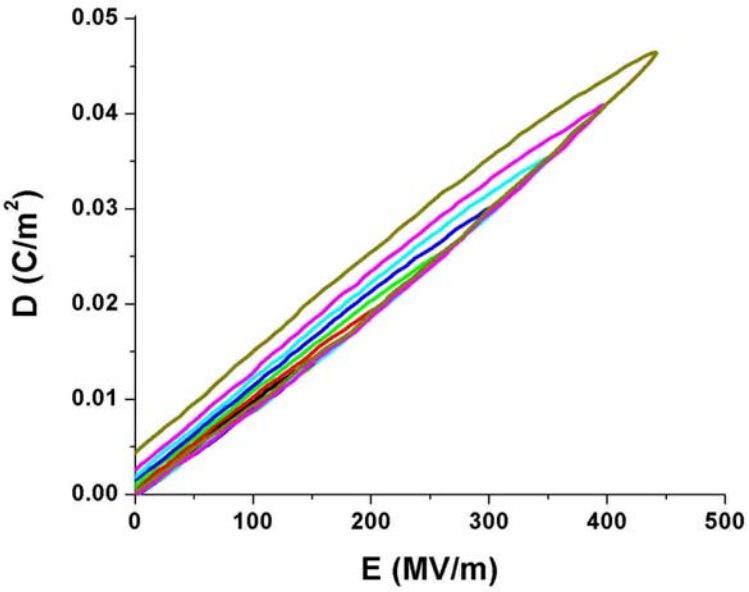

Figure 6.18. The D-E loops of P(VDF-CTFE)/Si_3N_4 bilayer with thickness ratio of P(VDF-CTFE):Si_3N_4 $\approx$2:1.

A comparison of different P(VDF-CTFE), PPO, and Si_3N_4 single layers and multilayers are shown in Figure 6.19 and Table 6.6. The films are compared at

Film	K	Stored (J/cm^3)	Released (J/cm^3)	Efficiency
PVDF-CTFE, stretched	13	11.10	7.31	65.9%
PVDF-CTFE:PPO=2:1	5.5	8.13	7.50	92.2%
PVDF-CTFE:Si_3N_4=2:1	9	11.10	8.95	80.5 %
PPO	2.75	8.88	8.88	>95%
Si_3N_4	7.1	15.40	15.40	>95%

Table 6.6. Comparison of the dielectric constants (K) and energy density of different films.

similar released energy density except for Si_3N_4. Pure Si_3N_4 film has the highest efficiency and relatively high energy density and seems to be the most promising material among all. However, Si_3N_4 is a stiff and brittle material which cannot be fabricated into capacitor films. Therefore, it is not suitable to be used along and for large scale applications it should be used together with polymers (i.e. in the form of multilayers).

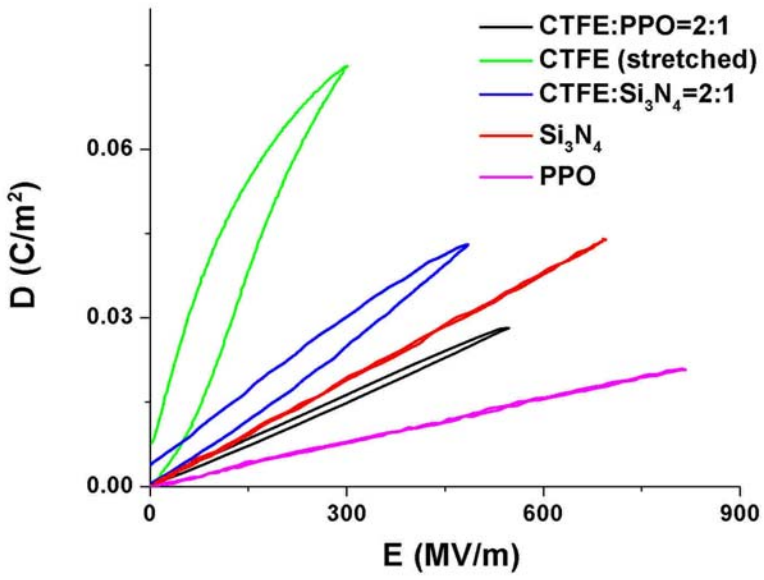

Figure 6.19. Comparison between the D-E loops of different films.

Chapter 7

CONCLUSIONS AND SUGGESTED FUTURE WORK

Electroactive polymers based on PVDF exhibit very large electro-optic (E-O) effect, electromechanical strain and electrical energy density. Examples of these polymers are P(VDF-TrFE-CFE) terpolymer and P(VDF-CTFE) copolymer. This thesis presents the study of the application of the P(VDF-TrFE-CFE) terpolymer and P(VDF-CTFE) copolymer in tunable optical devices and energy storage capacitors. As an example of tunable optical device, an electrically tunable long-period fiber grating (LPG) has been developed using the P(VDF-TrFE-CFE) terpolymer as E-O material. The tuning range of the tunable LPG is about 50nm when applied electric field is 50MV/m, which is sufficient to cover an entire fiber optic communication band. A computer simulation model has been developed to aim the design of the LPG. Simulation results revealed that the ITO layer used as the inner electrode of the terpolymer significantly enhanced the tuning range of the LPG. Furthermore, with proper ITO thickness and refractive index the variation of notch depth is very small while the resonance wavelength is tuned. It was

found that the effect of ITO on tuning characteristic of the LPG is due to the high refractive index of ITO which redistribute the light energy in the fiber. The enhancement of tuning due to ITO has been confirmed in index matching fluid test. Furthermore, it was also found that large tuning range can only be achieved when the native refractive index of the terpolymer is about 1.42, which is larger than the native refractive index of the terpolymer (n=1.4) by about 0.02. In order to increase the refractive index of the terpolymer while maintaining large E-O effect and high optical transparency, a nanocomposite with high refractive index zinc sulfide nanoparticles embedded in terpolymer matrix has been developed. Using the nanocomposite approach, increase of refractive index by as large as 0.1 can be achieved using only 10 vol% of zinc sulfide while the E-O effect was reduced by about one third. In order to prevent the agglomeration of nanoparticles which causes large scattering loss of light, the zinc sulfide nanoparticles were synthesized and mixed in-situ with terpolymer with the presence of coupling agents containing thiol groups. In this way, the optical loss of the nanocomposite film is almost the same as neat terpolymer films. When zinc-sulfide/terpolymer nanocomposite with 3 vol% of zinc sulfide is used as the E-O material for the tunable LPG, the native refractive index of the E-O layer is about 1.42 and the large tuning has indeed been achieved where the tuning range is 50nm.

For the application in energy storage capacitors, the breakdown behavior in the terpolymer and the conduction loss in P(VDF-CTFE) copolymer have been studied. It has been observed that the breakdown field of the terpolymer depends on the type of metal used as electrodes. Aluminum resulted in highest mean breakdown field (380MV/m) and narrowest distribution of the breakdown fields. On the other hand, silver and gold resulted in much lower breakdown field (300MV/m) and wider distribution. Even for the same type of metal, different deposition methods

also resulted in different breakdown fields. For gold and silver, sputtering resulted in better breakdown characteristics comparing to thermal and e-beam evaporation. It is believed that the dependence of breakdown field on electrode material and deposition method is due to both the work function difference between metals and the existence of interfacial layers. For instance, an interfacial layer has been detected for aluminum electrode which is due to the reaction between aluminum and polymer and ambient oxygen, while no interfacial layer has been found for silver and gold.

The electrical conduction in P(VDF-CTFE) copolymer has been studied. The J-t curves were dependent on electrode material and shows turning points. The J-V curves shows a current peak and a negative resistivity region. These observations suggest that the conduction in the copolymer is controlled by charge injection from the electrodes. However, at high fields the J-V curves are best fitted by field dependent mobility model which is a feature of bulk conduction. Therefore, it is believed that the charge injection into the copolymer is modified by bulk conduction in the polymer, as has been proposed earlier for charge injection into insulating materials. The reduction of conduction loss by using blocking layers has been demonstrated. Both poly(2,6-dimethyl-1,4-phenylene oxide) (PPO) and silicon nitride have been used as blocking layers and energy efficiencies of >90% and >80% have been achieved with released energy density of higher than 7.5J/cm^3.

An extension of the present study can be made into several areas related to this work but not yet explored. Following are a few suggested topics for future research.

Optical application

In the tunable fiber grating demonstrated in this thesis, the tuning range has been significantly enhanced by the high index ITO layer, and the notch depth variation can be minimized simultaneously. In many tunable optical devices, it is desirable to tune the resonance wavelength while maintaining a nearly constant field distribution. Therefore, the ITO effect in the tunable fiber grating can be applied to many other tunable optical devices. However, the refractive index of ITO is relatively difficult to control and hence thickness is the only variable for device design. In addition, ITO exhibits finite optical loss and hence the maximum thickness of ITO is limited.

In a generalized design, the ITO interlayer can be replaced by a multilayered stack that consists of layers of different materials. For instance, these can be alternating high index and low index layers as in the Bragg fibers [97, 98], and one of the layers can be P(VDF-TrFE-CFE) terpolymer which exhibits large E-O effect and another layer can be inorganic or organic material with high optical quality and suitable refractive index (Figure 7.1). This multilayered stack (layers A and B) can take the place of either the ITO interlayer only or both the interlayer and the second cladding (layer C). The unique dispersion relationship in such one dimensional photonic bandgap structures can provide very sensitive tuning in tunable fiber gratings. For a symmetric slab waveguide, in the ray optics treatment the eigen equation of a mode is [20]

$$akn_1 \sin\phi - \delta = N\pi \quad (N = 0, 1, 2, \cdots) \tag{7.1}$$

where a and n_1 are the thickness and refractive index of the slab, ϕ is the angle

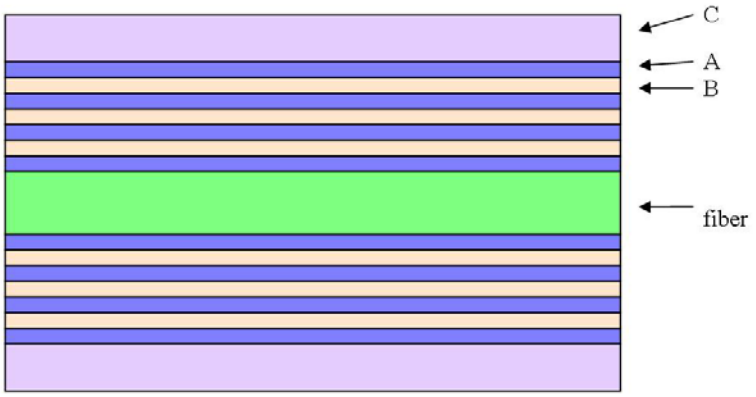

Figure 7.1. The structure of a fiber with multilayered second cladding.

between the ray and fiber axis [1], and k is the wave number of light in vacuum. The parameter δ is the phase retardation associated with the a total reflection at the boundary of the slab, which depends on the refractive indexes of the layers in the waveguide and the angle ϕ. In the external tuning regime, a and n_1 are constants, and the tuning of n_{eff} is determined by the change of δ due to e.g. the refractive index change in certain layers. For optical fibers, due to the cylindrical geometry the dispersion relationship of modes is more complicated than equation (7.1), but the tuning of n_{eff} is also determined by the change of δ. For a multilayer reflector, the phase retardation associated with reflection is high sensitive to the refractive index of the layers when operated close to the band edges of the reflector. In this case, more efficient tuning can be expected comparing to single high index interlayer.

[1] ϕ is related to effective refractive index by $n_{eff} = n_1 \cos\phi$

In addition to wider tuning range, another advantage of the multilayered structure is that when properly designed, much higher optical energy can be contained in the terpolymer active layers than in the passive layers. In tunable fiber gratings it is desirable that most light energy are contained in the core and in terpolymer layer so that large tuning range and deep notch can be achieved. Therefore, enhancing light energy in the terpolymer while suppressing it in the passive layers will improve both the tuning range and the notch depth.

The properties of fiber with multilayered interlayer or second cladding can be studied using the simulation model described in Chapter 3. The nature of the model allows for the analysis of arbitrary number of layers. Several different configurations can be studied. For instance, a possible configuration is that layer B in Figure 7.1 is the terpolymer layer while layers A and C are passive materials; another configuration is that no additional second cladding C is present; yet another configuration is that A and B are both passive materials and C is terpolymer.

The passive layers in this design can be either inorganic or polymer materials. Especially, polymers are preferred as the passive layer since they can be easily coated by dip coating whereas the inorganic layers are usually deposited by vacuum processes such as sputtering and thermal evaporation. A consideration of the all-polymer multilayered stack is that the dielectric constant of the terpolymer (50) is much higher than common polymers (typically <4), and hence if voltage is applied on the stack the achievable electric field in the terpolymer layer will be low. This problem can be overcome by using conducting polymers instead of dielectric polymer as the passive layer. Conducting polymers that are transparent at near infrared wavelengths are readily available [99].

Dielectric application

In the present development of multilayered films containing P(VDF-CTFE) copolymer and blocking layers, it is interesting to extend the study on new blocking materials and deposition techniques. Through this study the conduction loss could be further reduced and higher dielectric constant and energy density can be maintained.

The spin coated P(VDF-CTFE) layers in the present study exhibits conduction loss of at least one order higher comparing to extruded films. The large size of crystalline region in the present solution processed films is believed to significantly increase the conduction loss. Further study is required to improve the quality of solution processed films. For instance, suitable solvent and the curing procedure after spin coating could reduce the crystalline region size to an acceptable level. Extrusion followed by uniaxially stretching can readily produce very high quality films, but it would be challenging to fabricate sub-micron thick films using this method. The ultimate solution to fabricate high quality thin films would be using vapor phase deposition methods, such as chemical vapor deposition. However, it would require further study to properly control the composition of the deposited films.

When used as blocking layers, polymers are not expected to achieve significantly improved energy density and efficiency comparing to the current study. This is because of the low dielectric constant in low loss polymers, which limits the maximum field that can be applied on the multilayers. Perhaps the only case that could potentially achieve high performance is films that contains large number of ultrathin polymer layers (e.g. several nm) so that the interface properties dominates the response of the film. Such films could be fabricated using co-extrusion

technique.

On the other hand, the promising potential of inorganic blocking layers is far from being fully realized in the present study. For instance, the deposition process of silicon nitride blocking layers should be further optimized. In the D-E loops of P(VDF-CTFE)/Si_3N_4 bilayers, it was observed that there is considerable loss at low electric fields and the loss increases gradually with field. This is different from the behavior of P(VDF-CTFE)/PPO multilayers and is possibly due to damaging of films during deposition. Currently, film deposition has been performed under 125°C and plasma energy of 300W. Furthermore, during deposition the polymer is directly exposed to plasma and the high energy particles in the plasma could damage the polymer. In some modified PECVD deposition setup lower deposition temperature (down to room temperature) can be achieved and the plasma can be separated from substrate [100].

Silicon nitride can be also replaced by other inorganic blocking materials with higher dielectric constants. Examples of such high dielectric constant materials are tantalum oxide, titanium oxide, and aluminum oxide. In addition to vacuum deposition techniques, the oxide films can be also formed by anodizing metallic layers, which provides a potential low temperature process to deposit such layers.

Finally, only bilayers have been fabricated in the present study involving inorganic blocking layers, and it is expected that increasing the total number of layers while decreasing the thicknesses of individual layers could improve the performance of the multilayered films. This is because the large number of interfaces increases the number of energy barriers for the conducting carriers. In order to fabricate these multilayers, not only the possible damage of thin films during deposition should be concerned but also the adhesion between polymer and inorganic layers should be improved. For instance, it has been observed that P(VDF-CTFE) can-

not be spin coated on silicon nitride due to wetting problem. This problem could be overcome by choosing blocking materials with better wetting properties or by introducing an ultrathin interfacial layer to promote the wetting.

Bibliography

[1] T. Furukawa, "Ferroelectric Properties of Vinylidene Fluoride Copolymers," *Phase Transitions*, Vol. 18, No. 3-4, Part B, pp. 143-211. (1989)

[2] Q. M. Zhang, V. Bharti, and X. Zhao, "Giant Electrostriction and Relaxor Ferroelectric Behavior in Electron-irradiated Poly(vinylidene fluoride-trifluoroethylene) Copolymer", *Science*, vol. 280, No. 5372, pp. 2101-2104. (1998)

[3] F. Xia, Z. Y. Cheng, H. S. Xu, H. F. Li, Q. M. Zhang, G. J. Kavarnos, R. Y. Ting, G. Abdul-Sedat, and K. D. Belfield, "High ELectromechanical Responses in a Poly(vinylidene fluoride-triluoroethylene-chlorofluoroethylene) Terpolymer," *Advanced Materials*, vol. 14, No. 21, pp. 1574-1577. (2003)

[4] D. Y. Jeong, Y. K. Wang, M. Huang, Q. M. Zhang, G. J. Kavarnos, and F. Bauer, "Electro-optic Response of the Ferroelectric Relaxor Poly(vinylidene fluoride-trifluoroethylene-chlorofluoroethylene) Terpolymer," *Journal of Applied Physics*, Vol. 96, No. 1, pp. 316-319. (2004)

[5] B. J. Chu, X. Zhou, K. L. Ren, B. Neese, M. R. Lin, Q. Wang, F. Bauer, and Q. M. Zhang, "A Dielectric Polymer with High Electric Energy Density and Fast Discharge Speed", *Science*, Vol. 313, No. 5765, pp. 334-336. (2006)

[6] M. Rabuffi and G. Picci, "Status quo and future prospects for metallized polypropylene energy storage capacitors," *IEEE Transactions on Plasma Science*, Vol. 30, No. 5, pp. 1939-1942. (2002)

[7] K. W. Chung and S. Yin, "Analysis of a widely tunable long-period grating by use of an ultrathin cladding layer and higher-order cladding mode coupling," *Optics Letters*, Vol. 29, No. 8, pp. 812-814 (2004)

[8] S. Z. Yin, Q. M. Zhang, K. W. Chung, R. Yang, Z. Y. Cheng, and Y. Lu, "Investigation of the Electro-optic Properties of Electro Irradiated

Poly(vinylidene fluoride-trifluoroethylene) Copolymer," *Optical Engineering*, Vol. 39, No. 3, pp. 670-672. (2000)

[9] K. C. Kao, *Dielectric phenomena in solids*, pp. 354-358, Elsvier Academic Press, San Diego. (2006)

[10] G. D. Wilk, R. M. Wallace, and J. M. Anthony, "High-k gate dielectrics: Current status and materials properties considerations," *Journal of Applied Physics*, Vol. 89, No. 10, pp. 5243-5275. (2001)

[11] R. G. Kepler and R. A. Anderson, "Ferroelectric Polymers"' *Advances in Physics*, Vol. 41, No. 1, pp. 1-57 (1992)

[12] H. S. Nalwa, edt. *Ferroelectric Polymers*, Marcel Dekker, Inc., NY (1995)

[13] Q. M. Zhang, C. Huang, F. Xia, and J. Su, "Electric Polymers", in *Electroactive Polymer Actuators as Atificial Muscels*, Y. Bar-Cohen edt., SPIE Optical Engineering Prees, WA, pp. 89-139. (2004)

[14] Q. M. Zhang, V. Bharti, and G. Kavarnos, "Poly(vinylidene fluoride) (PVDF) and its copolymers," in *Encyclopedia of Smart Materials* Vol. 2, M. Schwartz ed., John Wiley & Sons Inc., pp. 807-826. (2004)

[15] H. Kawai, "The Piezoelectricity of Poly(vinylidene fluoride)", *Japanese Journal of Applied Physics*, Vol. 8, No. 7, pp. 975-976 (1969)

[16] T. T. Wang, J. M. Herbert, and A. M. Glass, edt. *The Applications of Ferroelectric Polymers*, Blackie and Son Ltd., London (1988)

[17] A. J. Lovinger, "Ferroelectric Polymers," *Science*, Vol. 220, No. 4602, pp. 1115-1121 (1980)

[18] "Relaxor Ferroelectric Poly(vinylidene fluoride-trifluoroethylene-chlorofluoroethylene) Terpolymer for High Energy Density Storage Capacitors", *IEEE Transactions on Dielectrics and Electrical Insulation*, Vol. 13, No. 5, pp. 1162-1169. (2006)

[19] A. M. Vengsarkar, P. J. Lemaire, J. B. Judkins, V. Bhatia, T. Erdogan, and J. E. Sipe, "Long-period fiber gratings as band-rejection filters," *Journal of Lightwave Technology*, Vol. 14, No. 1, pp. 58-65. (1996)

[20] M.J.Adams, *An Introduction to Optical Waveguides*, John Wiley & Sons, 1983.

[21] A. A. Abramov, A. Hale, R. S. Windeler, and T. A. Strasser, "Widely tunable long-period fiber gratings," *Electronic Letters*, Vol. 35, No. 1, pp. 81-82. (1999)

[22] A. A. Abramov, B. J. Eggleton, J. A. Rogers, R. P. Espindola, A. Hale, R. S. Windeler, and T. A. Strasser, "Electrically tunable efficient broad-band fiber filter," *IEEE Photonic Technology Letter*, Vol. 11, No. 4, pp. 445-447. (1999)

[23] Y. Jeong, H. R. Kim, S. Baek, Y. Kim, Y. W. Lee, S. D. Lee, and B. Lee, "Polarization-isolated electrical modulation of an etched long-period fiber grating with an outer liquid-crystal cladding," *Optical Engineering*, Vol. 42, No. 4, pp. 964-968. (2003)

[24] A. Yariv, "Coupled-mode theory for guided-wave optics," *IEEE Journal of Quantum Electronics*, Vol. 9, No. 9, pp. 919-933. (1973)

[25] H.Kogelnik, *Theory of Optical Waveguides*, ch.2 of *Guided-Wave Optoelectronics*, T.Tamir ed., Springer-Verlag, 1988

[26] "Cladding-mode Resonances in Short- and Long- Period Fiber Grating Filters," *Journal of the Optical Society of America A*, Vol. 14, No. 8, pp. 1760-1773. (1997)

[27] C. Yeh and G. Lindgren, "Computing the propagation characteristics of radially stratified fibers: an efficient method", *Applied Optics*, Vol.16, No. 2, pp. 483-493 (1977).

[28] Q. Chen, J. Lee, M. R. Lin, Y. Wang, S. Z. Yin, Q. M. Zhang, and K. M. Reichard, "Investigation of tuning characteristics of electrically tunable long-period gratings with a precise four-layer model", *Journal of Lightwave Technology*, Vol. 27, No. 7, pp. 2954-2962 (2006)

[29] T.Erdogan, *J Lightwave Technol.,* vol 15, no 8, pp 1277-1294, 1997

[30] J. W. Fleming, "Dispersion in GeO_2-SiO_2 glasses", *Applied Optics,* Vol. 23, No. 24, pp. 4486-4493 (1984)

[31] E. D. Palik ed., "Handbook of optical constants of solids", pp. 749, Academic Press, San Diego (1985)

[32] Y. S. Jung, "Spectroscopic ellipsometry studies on the optical constants of indium tin oxide films deposited under various sputtering conditions," *Thin Solid Films*, Vol. 467, No. 1-2, pp. 36-42. (2004)

[33] A. Cusano, A. Iadicicco, P. Pilla, L. Contessa, S. Campopiano, A. Cutolo, and M. Giodano, "Mode transition in high refractive index coated long period gratings", *Optics Express*, Vol. 14, No. 1, pp. 19-34 (2006)

[34] H. A. Haus, *Waves and fields in optoelectronics*, pp. 189, Prentice-Hall, Englewood Cliffs, NJ. (1984)

[35] R. Kashyap, *Fiber Bragg gratings*, Ch. 2, Academic Press, San Diego (1999)

[36] P. J. Lemaire, R. M. Atkins, V. Mizrahi, and W. A. Reed, "High-pressure H-2 loading as a technique for achieving ultrahigh UV photosensitivity and thermal sensitivity in GeO2 doped optical fibers," *Electronics Letters,* Vol. 29, No. 13, pp. 1191-1193 (1993)

[37] S. H. Nam, C. Zhan, J. Lee, C. Hahn, K. Reichard, P. Ruffin, K. L. Deng, and S. Yin, "Bend-insensitive ultra short long-period gratings by the electric arc method and their applications to harsh environment sensing and communication," *Optics Express*, Vol. 13, No. 3, pp. 731-737 (2005)

[38] R. B. H. Tahar, B. Takayuki, O. Yutaka, and T. Yasutaka, "Tin doped indium oxide thin films: Electrical properties," *Journal of Applied Physics*, Vol. 83, No. 5, pp. 2631-2645 (1998)

[39] Y. Marcus, *The Properties of Solvents*, Wiley, Chichester, UK (1998)

[40] H. Schmidt and M. Mennig, "Wet coating technologies for glass," online article at http://www.solgel.com/articles/Nov00/mennig.htm (2000).

[41] Q. Chen, M. R. Lin, J. E. Lee, Q. M. Zhang, and S. Yin, "Nanocomposites with very large electro-optic effect and widely tunable refractive index", *Applied Physics Letters*, Vol. 89, No. 14, Art. 141121 (2006)

[42] D. B. Stegall and T. Erdogan, "Leaky cladding mode propagation in long-period fiber grating devices," *IEEE Photonic Technology Letters*, Vol. 11, No. 3, pp. 343-345. (1999)

[43] G. Nemova and R. Kashyap, "Fiber-Bragg-grating-assisted surface plasmon-polariton sensor", *Optics Letters*, Vol. 31, No. 14, pp. 2118-2120. (2006)

[44] D. Y. Jeong, Y. H. Ye, and Q. M. Zhang, "Electrical tunable Fabry-Perot interferometer using a poly(vinylidene fluoride-trifluoroethylene-chlorofluoroethylene) terpolymer", *Applied Physics Letters*, Vol. 85, No. 21, pp. 4857-4859. (2004)

[45] M. D. Barnes, C. -Y. Kung, N. Lermer, K. Fukui, B. G. Sumpter, D. W. Noid, and J. U. Otaigbe, "Homogeneous polymer blend microparticles with a tunable refractive index," *Optics Letters*, Vol. 24, No. 3, pp. 121-123. (1999)

[46] J. Bicerano, *Prediction of Polymer Properties*, Ch. 8, Marcel Dekker, New York (2002)

[47] S. H. Zhang, N. Y. Zhang, C. Huang, K. L. Ren, and Q. M. Zhang, "Microstructure and electromechanical properties of carbon nanotube/poly(vinylidene fluoride-trifluoroethylene-chlorofluoroethylene) composites", *Advanced Materials*, Vol. 17, No. 15, pp. 1897-1901 (2005)

[48] C. Huang and Q. M. Zhang, "Fully functionalized high-dielectric-constant nanophase polymers with high electromechanical response", *Advanced Funcitional Materials*, Vol. 14, No. 5, pp. 501-506. (2004)

[49] C. L. Lu, Z. C. Cui, Z. Li, B. Yang, and J. C. Shen, "High refractive index thin films of ZnS/polythiourethane nanocomposites," *Journal of Materials Chemistry*, Vol. 13, No. 3, pp. 526-530. (2003)

[50] C. L. Lu, Z. C. Cui, Y. Wang, Z. Li, C. Guan, B. Yang, and J. C. Shen, "Preparation and characterization of ZnS-polymer nanocomposite films with high refractive index," *Journal of Materials Chemistry*, Vol. 13, No. 9, pp. 2189-2195. (2003)

[51] S. H. Zhang, B. Neese, K. L. Ren, B. J. Chu, and Q. M. Zhang, "Microstructure and electromechanical responses in semicrystalline ferroelectric relaxor polymer blends," *Journal of Applied Physics*, Vol. 100, No. 4, Art. 044113. (2006)

[52] X. Zhou, B. J. Chu, B. Neese, M. R. Lin, and Q. M. Zhang, "Electrical energy density and discharge characteristics of a poly(vinylidene fluoride-chlorotrifluoroethylene) copolymer," *IEEE Transactions on Dielectrics and Electrical Insulation*, Vol. 14, No. 5, pp. 1133-1138 (2007)

[53] F. Bauer, E. Fousson, Q. M. Zhang, and L. M. Lee, *IEEE Transactions on Dielectrics and Electrical Insulation*, Vol. 11, pp. 293 (2004)

[54] 7. J. K. Nelson, "Breakdown strength of solids," in *Engineering Dielectrics*, vol. 2A, R. M. Eichhorn and R. Bartnikas edt., Philadelphia, PA:ASTM, 1983

[55] N. R. Tu and K. C. Kao, "High-field electrical conduction in polyimide films," *Journal of Applied Physics* Vol. 85, No. 10, pp. 7267-7275. (1999)

[56] S. H. Zhang, B. J. Chu, B. Neese, K. L. Ren, X. Zhou, and Q. M. Zhang, "Direct spectroscopic evidence of field-induced solid-state chain conformation transformation in a ferroelectric relaxor polymer," *Journal of Applied Physics*, Vol. 99, No. 4, Art. 044107. (2006)

[57] H. E. Tsung, K. Y. Peng, and S. A. Chen, "Molecular oxygen and moisture as traps in poly[2-methoxy-5-(2 '-ethylhexyloxy)-1,4-phenylene vinylene]: locations and detrapping by chain relaxation," *Applied Physics Letters*, Vol. 82, No. 23, pp. 4086-4088. (2003)

[58] T. Tanaka, "Space charge injected via interfaces and tree initiation in polymers," *IEEE Transactions on Dielectrics and Electrical Insulation*, Vol. 8, No. 5, pp. 733-743. (2001)

[59] A. Neugroschel, L. Q. Wang, and G. Bersuker, "Trapped charge induced gate oxide breakdown," *Journal of Applied Physics*, Vol. 96, No. 6, pp. 3388-3398. (2004)

[60] D. Liu and K. C. Kao, "High-field hole injection, conduction, and breakdown in polyethylene films fabricated by plasma polymerization," *Journal of Applied Physics*, Vol. 69, No. 4, pp. 2489-2496. (1991)

[61] H. Sussner and K. Dransfeld, "Importance of the metal-polymer interface for the piezoelectricity of Polyvinylidene Fluoride," *Journal of Polymer Science: Polymer Physics*, Vol. 16, pp. 529-543. (1978)

[62] T. Mizutani, T. Nagata, M. Ieda, "TSC due to space-charge in polyvinylidene fluoride," *Journal of Physics D: Applied Physics*, Vol. 17, No. 9, pp. 1883-1887. (1984)

[63] C. Shen and A. Kahn, "Electronic structure, diffusion, and p-doping at the Au/F16CuPc interface," *Journal of Applied Physics*, Vol. 90, No. 9, pp. 4549-4554. (2001)

[64] H. Ahn and J. E. Whitten, "The metallicity of aluminum and gold in contact with thin films of a urethane-substituted polythiophene," *Journal of Applied Physics*, Vol. 93, No. 6, pp. 3384-3388. (2003)

[65] F. Faupel, "Diffusion and interface formation at polymer-metal interfaces," in *Polymer-solid interfaces: proceedings of the first international conference*, Namur, Belgium, 2-6 September 1991, J. J. Pireaux edt. , Institute of Physics Publishing, Bristol. pp. 171-188 (1992).

[66] B. Xu, C. N. Borca, S. Ducharme, A. V. Sorokin, P. A. Dowben, V. M. Fridkin, S. P. Palto, N. N. Petukhova, and S. G. Yudin, "Aluminum doping of poly(vinylidene fluoride with trifluoroethylene) copolymer," *Journal of Chemical Physics*, Vol. 114, No. 4, pp. 1866-1869. (2001)

[67] C. Shen, A. Kahn, and J. Schwartz, "Role of metalCmolecule chemistry and interdiffusion on the electrical properties of an organic interface: The Al-F16CuPc case," *Journal of Applied Physics*, Vol. 90, No. 12, pp. 6236-6242. (2001)

[68] F. Xia, H. S. Xu, F. Fang, B. Razavi, Z. Y. Cheng, Y. Lu, B. M. Xu, and Q. M. Zhang, "Thickness dependence of ferroelectric polarization switching in

poly(vinylidene fluoride-trifluoroethylene) spin cast films," *Applied Physics Letters*, Vol. 78, No. 8, pp. 1122-1124. (2001)

[69] "Electron Work Function of The Elements," in *Handbook of Chemistry and Physics*, D. R. Lide ed., CRC Press, 12-114 (2005)

[70] J. Metz and P. Plissart, "Plastic materials made of heterogeneous copolymers of vinylidene fluoride," US Patent No. 5292816 (1993)

[71] Solvay membranes, http://www.solvaymembranes.com/products/fluoropolymers/solefpvdf

[72] J. G. Simmons, "Richardson-Schottky effect in solids," *Physical Review Letters*, Vol. 15, No. 25, pp. 967-968. (1965)

[73] P. W. Anderson, "Absence of diffusion in certain random lattices," *Physical Review*, Vol. 109, No. 5, pp. 1492-1505. (1958)

[74] P. Nagels, "Electronic transport in amorphous semiconductors," in *Amorphous Semiconductors*, M. H. Brodsky edt., Berlin, pp. 113-158. (1985)

[75] S. M. Sze, *Physics of semiconductor devices*, 2nd ed., Ch. 5, John Wiley & Sons, New York (1981)

[76] K. S. Cole and R. H. Cole, "Dispersion and absorption in dielectrics," *Journal of Chemical Physics*, Vol. 10, No.2, pp. 98-105. (1942)

[77] R. H. Walden, "A method for the determination of high-field conduction lows in insulating films in the presence of charge trapping," *Journal of Applied Physics*, Vol. 43, No. 3, pp. 1178-1186. (1972)

[78] C. B. Duke and T. J. Fabish, "Charge-induced relaxation in polymers," *Physical Review Letters*, Vol. 37, No. 16, pp. 1075-1078. (1976)

[79] M. A. Baldo and S. R. Forrest, "Interface-limited injection in amorphous organic semiconductors," *Physical Review B*, Vol. 64, No. 8, Art. 085201. (2001)

[80] P. W. M. Blom, M. J. M. de Jong, and M. G. van Munster, "Electric-field and temperature dependence of the hole mobility in poly(p-phenylene vinylene)," *Physical Review B*, Vol. 55, No. 2, pp. R656-R659. (1997)

[81] T. Minari, T. Nemoto and S. Isoda, "Temperature and electric-field dependence of the mobility of a single-grain pentacene field-effect transistor," *Journal of Applied Physics*, Vol. 99, Art. 034506. (2006)

[82] P. R. Emtage, "Conduction by small polarons in large electric fields," *Physical Review B*, Vol. 3, No. 8, pp. 2685-2689. (1971)

[83] B. J. Chu, M. R. Lin, B. Neese, X. Zhou, Q. Chen, and Q. M. Zhang, "Large enhancement in polarization response and energy density of poly(vinylidene fluoride-trifluoroethylene-chlorofluoroethylene) by interface effect in nanocomposites," *Applied Physics Letters* Vol. 91, No. 12, Art. 122909. (2007)

[84] J. Y. Li, "Exchange coupling in P(VDF-TrFE) copolymer based all-organic composites with giant electrostriction," *Physical Review Letters*, Vol. 90, No. 21, Art. 217601. (2003)

[85] H. Zhang and R. Solanki, "Atomic layer deposition of high dielectric constant nanolaminates," *Journal of The Electrochemical Society*, Vol. 148, No. 4, pp. F63-F66. (2001)

[86] J. Brundrup, E. H. Emmelgut, E. A. Grulke, (edt.) *Polymer Handbook*, 4th edition, John Wiley & Sons, New York (1999)

[87] D. L. Smith, "Controlling the plasma chemistry of silicon nitride and oxide deposition from silane," *Journal of Vacuum Science and Technology A*, Vol. 11, No. 4, pp. 1843-1850. (1993)

[88] K. I. Lundstrom and C. M. Svensson, "Properties of MNOS structures," *IEEE Transactions on Electron Devices*, Vol. ED-19, No. 6, pp. 826-836. (1971)

[89] M. Tao, D. Park, S. N. Mohammad, D. Li, A. E. Botchkerav, and H. Morkoc, "Electrical conduction in silicon nitrides deposited by plasma enhanced chemical vapor deposition," *Philosophical Magazine B*, Vol. 73, No. 4, pp. 723-726. (1996)

[90] M. D. Groner, J. W. Elam, F. H. Fabreguette, and Sm M. George, "Electrical characterization of thin Al2O3 films grown by atomic layer deposition on silicon and various metal substrates," *Thin Solid Films*, Vol. 413, pp. 186-197. (2002)

[91] D. J. Dumin, J. R. Cooper, J. R. Maddux, R. S. Scott, and D. P. Wong, "Low-level leakage currents in thin silicon oxide films," *Journal of Applied Physics*, Vol. 76, No. 1, pp. 319-327. (1994)

[92] R. M. Fleming, D. V. Lang, C. D. W. Jones, M. L. Steigerwald, D. W. Murphy, G. B. Alers, Y. H. Wong, R. B. van Dover, J. R. Kwo, and A. M. Sergent, "Defect dominated charge transport in amorphous Ta2O5 thin films," *Journal of Applied Physics*, Vol. 88, No. 2, pp. 850-862. (2000)

[93] S. A. Campbell, H. S. Kim, D. C. Glimer, B. He, T. Ma, and W. L. Gladfelter, "Titanium dioxide (TiO2) based gate insulators," *IBM Journal of Research and Development*, Vol. 43, No. 3, pp. 383-392. (1999)

[94] L. Kang, B. H. Lee, W. J. Qi, Y. Jeon, R. Nieh, S. Gopalan, K. Onishi, and J. C. Lee, "Electrical characteristics of highly reliable ultrathin hafnium oxide gate dielectric," *IEEE Electron Device Letters*, Vol. 21, No. 4, pp. 181-183. (2000)

[95] W. J. Qi, R. Nieh, B. H. Lee, L. Kang, Y. Jeon, and J. C. Lee, "Electrical and reliability characteristics of ZrO2 deposited directly on Si for gate dielectric application," *Applied Physics Letters*, Vol. 77, No. 20, pp. 3269-3271. (2000)

[96] S. M. Sze, "Current transport and maximum dielectric strength of silicon nitride films," *Journal of Applied Physics*, Vol. 38, No. 7, pp. 2951-2956. (1967)

[97] P. Yeh, A. Yariv, and E. Marom, "Theory of Bragg fiber," *Journal of the Optical Society of America*, Vol. 68, No. 9, pp. 1196-1201. (1978)

[98] P. Yeh, A. Yariv, and C. S. Hong, "Electromagnetic propagation in periodic stratified media. I. General theory," *Journal of the Optical Society of America*, Vol. 67, No. 4, pp. 423-438. (1976)

[99] V. G. Kulkarni, "Transparent Conducting Coatings," in *Handbook of Conducting Polymers*, 2nd edition, T. A. Skotherm, R. L. Elsenbaumer, and J. R. Reynolds ed., Marcel Dekker Inc., New York, pp. 1059-1073. (1998)

[100] I. Kato, K. Noguchi, and K. Numada, "Preparation of silicon nitride films at room temperature using double-tubed coaxial line-type microwave plasma chemical vapor deposition system," *Journal of Applied Physics*, Vol. 62, No. 2, pp. 492-497. (1987)

Vita

Qin Chen

Qin Chen was born on May 28, 1983 in Jiangxi Province, China. He received a bachelor of science degree in electronic engineering from Tsinghua University, Beijing, China in 2003. He then came to the Pennsylvania State University as a Ph. D. student in the Department of Electrical Engineering. Qin is a student member of IEEE, OSA, SPIE, and MRS.